Bending Vibration of Rotating Drill Strings

by

Rong-Juin Shyu

B. S., National Cheng-Kung University, Tainan, Taiwan

(1980)

M. S., National Taiwan University, Taipei, Taiwan

(1982)

Submitted in Partial Fulfillment
of the Requirements for the

Degree of

Doctor of Philosophy

in Ocean Engineering

at the

Massachusetts Institute of Technology

August 1989

Signature of Author _____

Department of Ocean Engineering
August 7, 1989

Certified by _____

Professor J. Kim Vandiver
Thesis Supervisor

Accepted by _____

Professor A. Douglas Carmichael
Chairman, Departmental Graduate Committee

Bending Vibration of Rotating Drill Strings

by

Rong-Juin Shyu

Submitted to the
Department of Ocean Engineering
on August 4, 1989 in partial fulfillment of the requirements
for the Degree of Doctor of Philosophy

Abstract

Several dominant mechanisms which cause the bending vibration of rotating drill strings have been identified, they are :

- Linear coupling between dynamic axial force and bending vibration
- Parametrically excited bending vibration due to dynamic axial force
- Whirling of the drill string with and without borehole contact

Mathematical models for explaining and predicting these bending behaviors have been found and discussed. Experiments carried out in the laboratory confirmed the existence of the linear and parametric coupling between axial force and bending vibration. Data from a field test conducted in 1984 by Shell Oil Company also showed the existence of the both types of coupling. Forward and backward whirling of the drill string are also evident in this data set.

Because of the effect of rotation, the frequencies needed to excite the linearly coupled bending vibrations, and the parametrically excited bending vibration, are varying linearly with respect to the rotational speed. This phenomenon is explained and demonstrated by the laboratory experiments. The effect of rotation plays a crucial role in understanding the bending vibration of a rotating drill string.

Thesis Supervisor: Professor J. Kim Vandiver

Title: Professor of Ocean Engineering

Acknowledgments

I would, first of all, like to thank my academic and thesis advisor, Prof. J. Kim Vandiver, for his helpful insights that lead me to this thesis topic, for his patience and guidance that made this thesis possible, and for his great personality that made my stay in MIT very fruitful and enjoyable. I would like to thank my thesis committee: Prof. Stephen Crandall, Prof. Dale Karr, and Dr. George Triantafyllou, for their critical suggestions that help in writing this thesis.

My special thanks go to my family, especially my parents, for their continuing encouragement and support over the years. I would also like to thank my colleagues over the years, C. Y. Liou, T. Y. Chung, N. Joglekar, H. Y. Lee, C. Y. Hsin, Chifang Chen, H. Miyachi, for their numerous discussions and friendship. I would also like to thank Ms. Shiela McNary for her many typing jobs.

This work is primarily sponsored by Agip, Amoco, Annadrill, Britoil-British Petroleum, Elf Aquitaine, Exploration Logging, Exxon, Shell, Statoil, Teleco, and Total. A special thanks goes to Shell Development Co. for the permission to publish data which were acquired during a field test in 1984.

Finally, my thanks goes to two special friends, my master's thesis advisor, Prof. C. S. Lee of National Taiwan University, and Ms. Chou Su, for their friendship and encouragement which have positively changed many aspects of my life.

Contents

List of Figures

List of Tables

Chapter 1

Introduction

The vibration of drillstrings includes longitudinal, torsional and bending vibration. This dissertation focuses on bending vibrations in the bottom hole assembly (BHA). The BHA is emphasized because many of the the most severe forms of bending vibration occur there, and because the most common location for drillstring failures attributable to bending vibration is in the BHA. Bending vibration is often severe near the bit, because bit forces drive some forms of bending vibration. Whirling is also most common near the bit, because the large mean compressive loads on the drill collars near the bit produce significant curvature of the drill collars.

Bending vibration generated near the bit does not usually propagate to the surface as torsional and longitudinal vibration does. This is due to the vastly different wave propagation velocities. The propagation speed of axial waves in steel drill pipe is about 16,850 feet per second and of torsional waves is about 10,200 ft/sec. Even at a depth of several thousand feet the distance to the bottom of the hole is no more than a few wave lengths at frequencies less than 30 Hz. Thus these waves are commonly felt at the surface. In contrast bending waves at 30 Hz have a wave speed of approximately 600 ft/sec, and therefore must travel many wavelengths to reach the surface. Lower frequencies travel even more slowly. Furthermore, bending vibrations have larger damping, produced by the mud and wall contact and therefore, bending waves, generated at the bottom do not propagate to the surface unless the hole is very shallow.

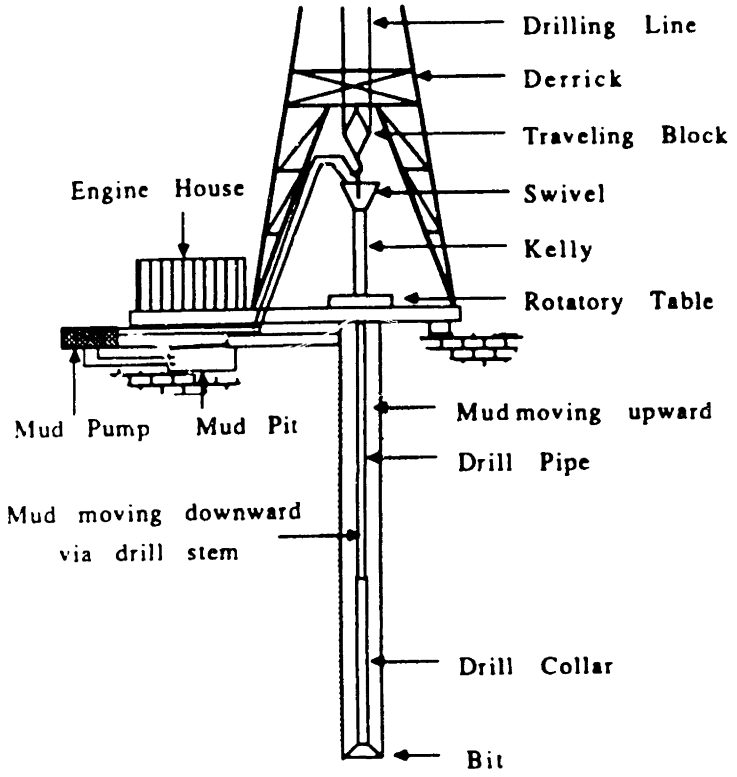

Figure 1.1: A Typical Oil Drilling Rig

In part, because bending vibration was not commonly observed at the surface, it was not well understood or recognized as being a problem. The evidence of connection fatigue failures in drill collars, failure of downhole MWD tools and heavy surface abrasion of collars and stabilizers has provided evidence to the contrary. In recent years, the availability of downhole vibration measurements has provided the necessary insight to guide the development of bending vibration models for BHA's. The goal of this dissertation is to identify and describe the most important bending mechanisms in BHA's, to develop analytical and numerical models of these phenomena and to verify them through the use of laboratory models and downhole measurements.

1.1 Basic Drilling Equipment

Let us start by introducing the terminology for drilling frequently used in a drilling operation. A typical land-based drilling rig is shown in figure 1.1 There are several

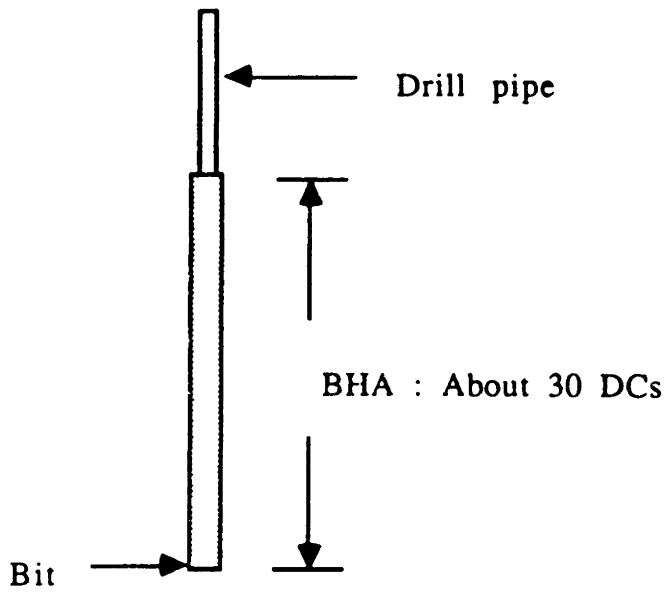

Figure 1.2: Bottom Hole Assembly

terms that are used frequently in the drilling industry and in this thesis. Following is a list of these terms.

Drill String: It consists of the kelly, drill pipe, drill collars, and a variety of special tools. Either collar or pipe can be added to extend the drilling depth.

Drill Collar: Drill collars are designed to operate in compression without buckling, so as to provide the weight and torque to the bit.

Drill Pipe: Drill pipe is used to transfer torque from the rotary table to the drill collar and to support the weight of the drill string. Drill pipe is designed to operate in tension, so the cross sectional area is smaller than that of the drill collars.

Bottom Hole Assembly (BHA) : It is a section of the drill string from bit to the top of the drill collar. Its length is typically several hundred feet. Fig 1.2 shows the BHA.

Stabilizer: It is a device that holds the drill collar in the center of the borehole. The arrangement of the stabilizers affects the direction of the borehole and the bending natural frequencies of the drill collars. Fig 1.3 shows a standard four-bladed stabilizer.

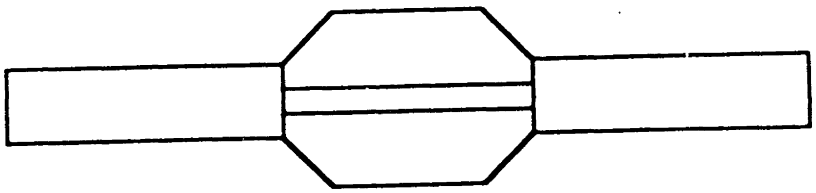

Figure 1.3: A Four-Bladed Stabilizer

Weight On Bit (WOB): The compression force acting on the bit.

Torque On Bit (TOB): The torque acting on the bit.

1.2 Problems in Drilling Dynamics

The dynamics of a drill string pose a unique problem in vibration analysis. In the upper part of the drill string, the state of the stress is tension, whereas, in the lower part of the drill string due to the weight on the bit, the state of the stress is compression. Figure 1.4 depicts typical stress variations along the drill string. A drill string is also subjected to various dynamic forces, including:

1. mud pressure fluctuations
2. weight on bit and torque on bit fluctuations
3. internal and external damping forces
4. centrifugal forces.
5. interactions with the wall.

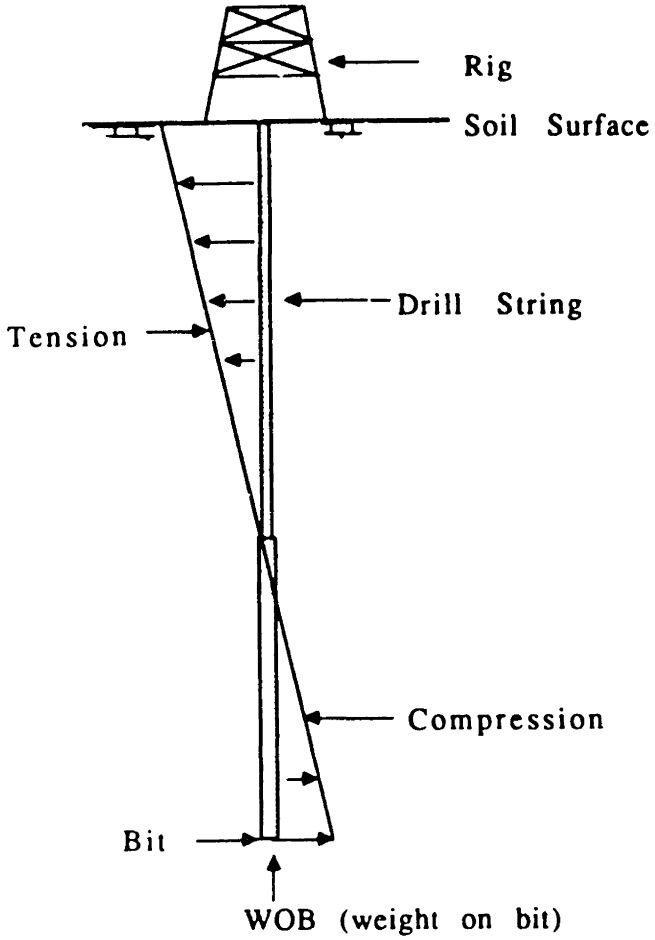

Figure 1.4: Stress Variation Along the Drill String

Because of these forces, a number of problems may arise. For example: the bit may bounce on the cutting surface resulting in bit damage; severe bending moments may develop in the BHA leading to the fatigue failures; forward whirl may cause wear against the bore hole, and backward whirl due to the friction of the wall may result in fatigue failure. These phenomena are all hazardous to drilling operations.

1.3 Outline of the Thesis

This thesis concentrates on the understanding of bending related vibrations of the BHA. They include whirl-related motion, bending vibration due to linear coupling with axial forces, and parametrically excited bending vibration. These studies will

help us gain insights into the dynamic behavior of the BHAs.

In the second chapter, the motions of a typical drill collar are described in both fixed and rotating coordinate systems. These motions include forward whirling , backward whirling, and whirling with bending vibration. Detail is given to reveal how one uses measurements made in a rotating frame of reference to deduce the collar motions. The rotating frame of reference is important to drilling engineers, since most downhole transducers are mounted inside rotating drill collars.

In the third chapter, the equations of motion of bending vibration of the Bottom Hole Assembly are given, and a finite difference scheme is introduced to solve the eigenvalue problem. This model accounts for the effects of linear varying compression, mud added mass and damping forces, and dynamic variations in WOB. It also takes into account the effect of stabilizers. The natural frequencies are expressed with respect to a fixed coordinate system. The bifurcation of the natural frequencies resulting from expressing natural frequencies in terms of a rotating coordinate system is also explained.

In the fourth chapter, linearized coupled equations between axial and bending vibration are presented by assuming small curvature. This equation represents the linear effect of axial force on the bending vibration. Also presented are the equations of motion showing the parametric axial force excitation of bending vibration. Examples are given to demonstrate linear and parametric axial excitation of bending vibration.

In the fifth chapter, rubbing contact between the drill collars and the wall are explained. Forward and backward whirl with slip are presented. Whirling can potentially shorten the fatigue life of drill collars and can cause substantial surface abrasion.

Chapter six shows a series of laboratory experiments that demonstrate the behavior predicted by the mathematical model. The experiments included strain gage bending measurements of whirling and bending vibration. Linear and parametric coupling between axial force and bending vibration are demonstrated in both rotating and non-rotating cases.

Chapter seven shows the results of a field test. This test was conducted by Shell and NL in 1984. A total of 60 hours of downhole data were taken during that experiment. Six examples are presented to demonstrate the behavior mentioned in previous chapters, including, whirl, linear coupling, and parametrically excited bending vibration.

Chapter eight concludes the results obtained so far. Several suggestions are made for future research.

Chapter 2

Measurement Systems on a Rotating Shaft

In rotor vibration measurements, the motion of the shaft is usually measured by proximity probes. This kind of measurement reveals only the motion of the center of gravity of the shaft. The measurements are taken with respect to a fixed coordinate system, attached to the earth. When the measurements are taken by a transducer attached to the rotating shaft, they are more difficult to interpret, because they are not taken with regard to a fixed coordinate system, and usually are not taken at the center of gravity. The following gives a simple description of the motion of a drill collar as seen from both frames of reference under various combinations of whirling and rotation, and shows how to interpret the measurements from transducers attached to the collar.

2.1 Motion of a Drill Collar in Pure Whirling

Figure 2.1 is the definition of the coordinate system used to describe the motion of the drill collar, where :

Oxy = fixed reference frame centered in the borehole

Ox'y' = rotating reference frame with speed Ω and with its origin located on the axis of the borehole

Ax"y" = rotating reference frame with speed ω and with origin

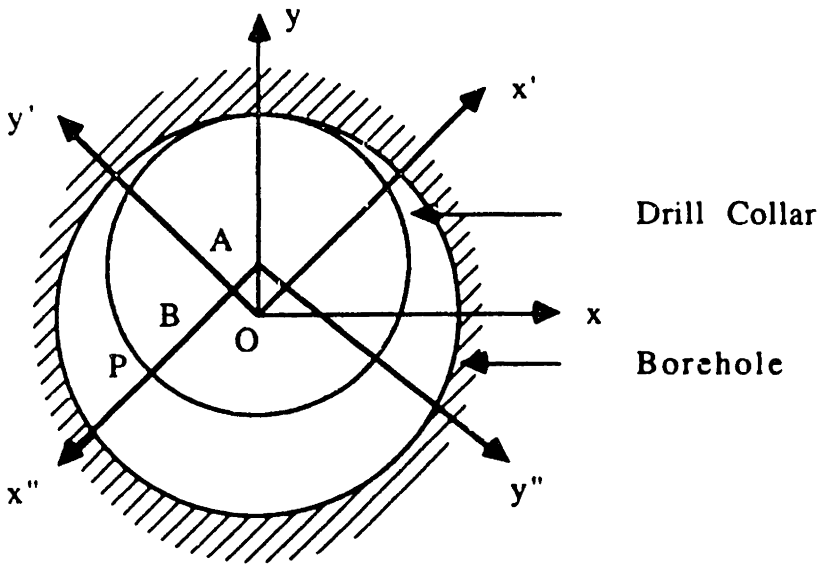

Figure 2.1: Definition of the Coordinate System

	located at the center of the drill collar
Ω	= whirling speed of the collar with respect to Oxy (rad/sec)
ω	= rotation speed of the collar with respect to Oxy (rad/sec)
R_1	= whirling radius or displacement of the drill collar center
R_2	= radius of the collar (= 3.5 inches in examples)
R_3	= radial location of the radial and tangential accelerometers

When the collar contacts the wall, R_1 equals the clearance, which in these examples is specified as .875 inches.

2.2 Motion Seen From Coordinate Oxy

Figure 2.2 shows the linear relationship of v vs. whirl rate, Ω at a fixed rotation rate, ω, where v is the tangential contact velocity between the circumference of the collar and the wall. The following figures represent the trajectory of a point P, fixed to the circumference of the collar, as seen from a fixed coordinate system, Oxy, under various slipping and whirling conditions. In all cases, the collar is in constant contact with the wall. Figures 2.3 to 2.9 correspond to the points a through g as shown on

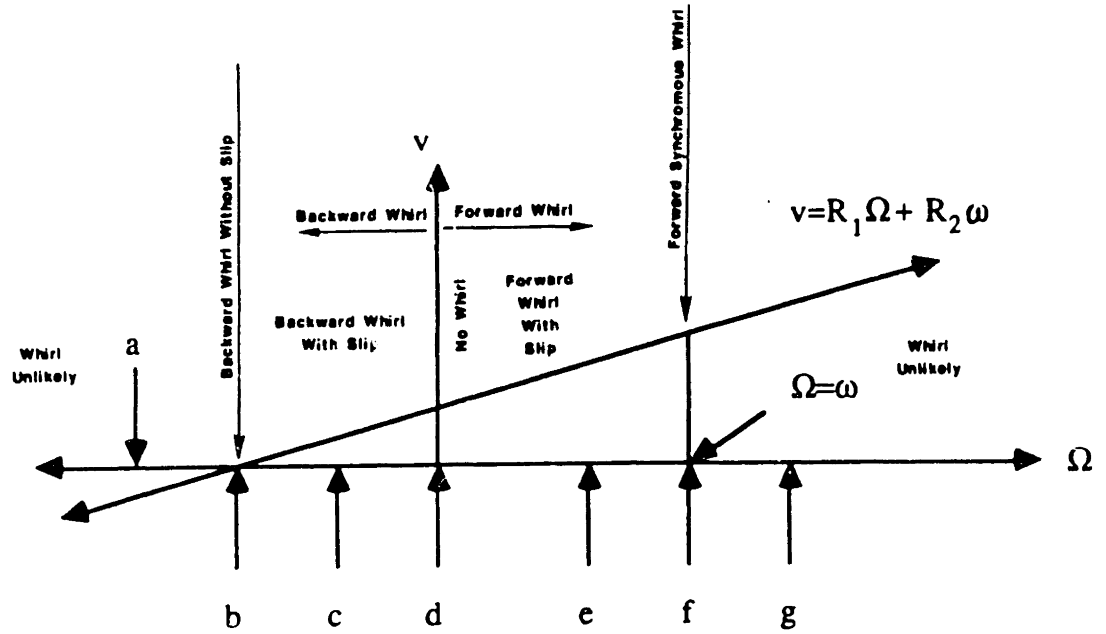

Figure 2.2: Tangential Velocity of a Circumferential Point vs Whirling Speed

Figure 2.2. Figure 2.8 represents the trajectory under synchronous whirl, in which whirl rate is equal to rotation rate. The minus sign of the rotation rate indicates the direction is clockwise. Figure 2.6 shows the trajectory of P with pure rotation, ie. Ω equals to zero. Figure 2.4 show the trajectory of point P under backward whirl with no slip. The backward whirl rate under this condition is $\frac{R_2\omega}{R_1}$, and the velocity at the contact point between the collar and the wall is always pointing toward the center of the hole. No tangential velocity component is present in this case. Figure 2.5 shows the trajectory of P under backward whirl with slip. The backward whirl rate is smaller than that in Figure 2.4, and the tangential velocity of the contacting point is no longer zero. Figure 2.7 is the case of forward whirl with slip, but the whirl rate is lower than the rotation rate. Figure 2.3 represents the case when the backward whirl rate is larger than $\frac{R_2\omega}{R_1}$, and Figure 2.9 shows the case with forward whirl rate greater than the rotation rate. Both of these cases are not likely to happen in the real drilling situation. In all cases mentioned above, the center of the collar, point A, would appear to move in a circle about O with a radius R_1 and at frequency Ω .

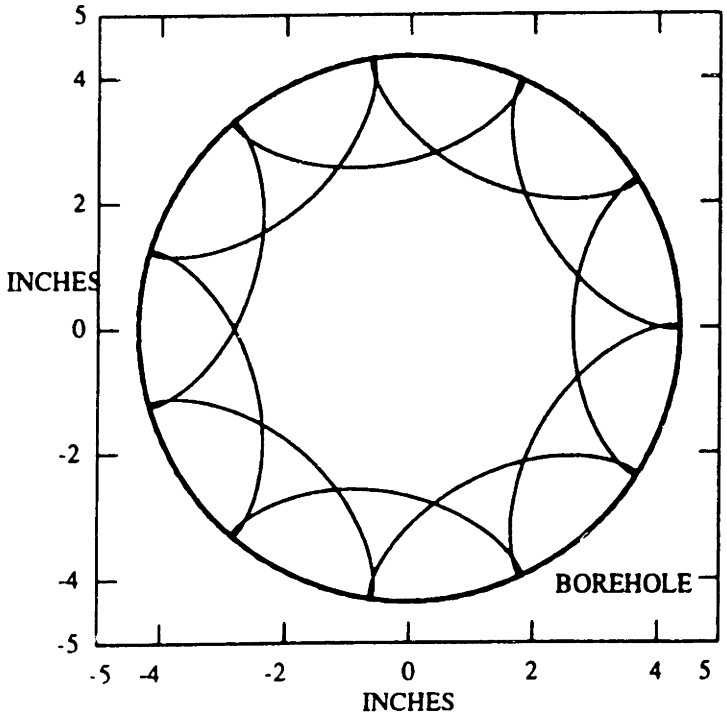

Figure 2.3: Backward Whirl with Slip, Rotation Speed -2.2 Hz, Whirling Speed 9.9 Hz

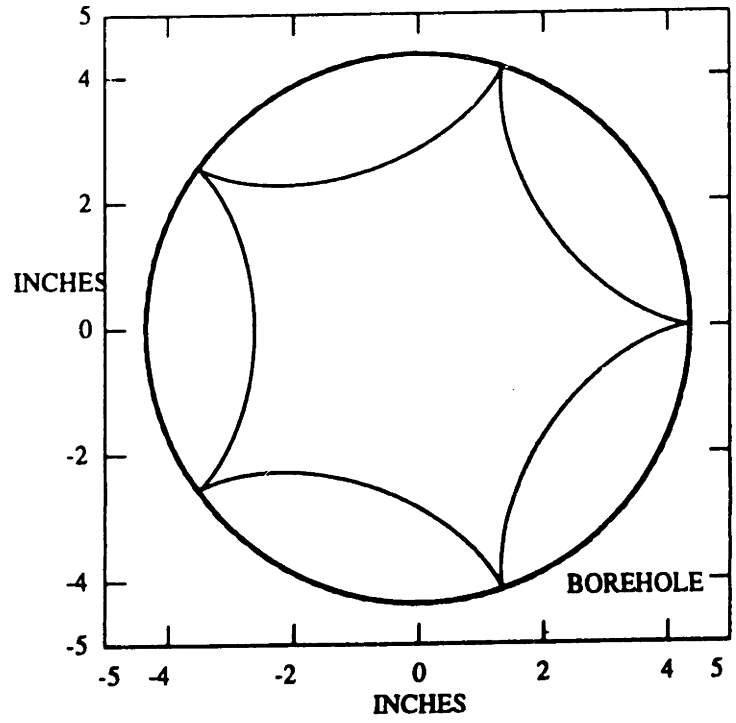

Figure 2.4: Backward Whirl, No Slip, Rotation Speed -2.2 Hz, Whirling Speed 8.8 Hz

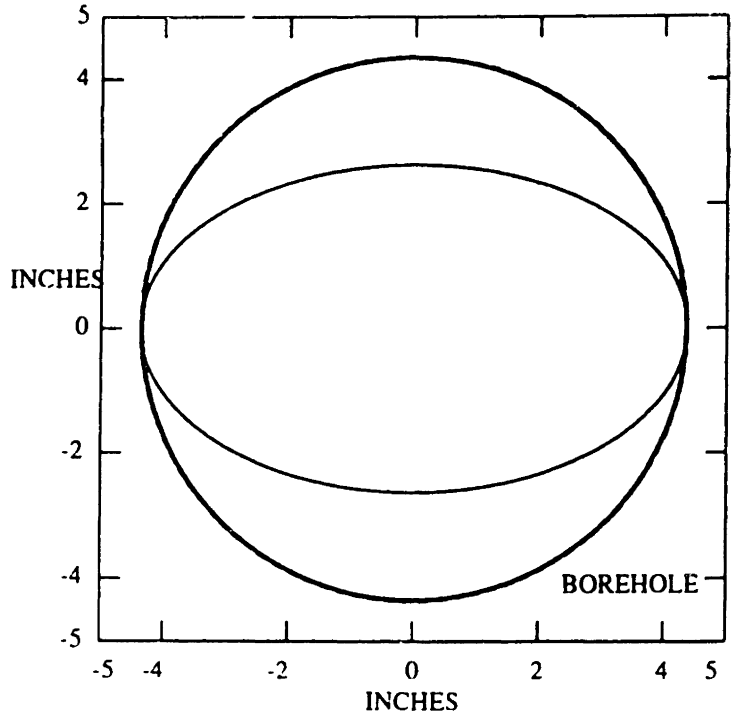

Figure 2.5: Backward Whirl With Forward Slip, Rotation Speed -2.2 Hz, Whirling Speed 2.2 Hz

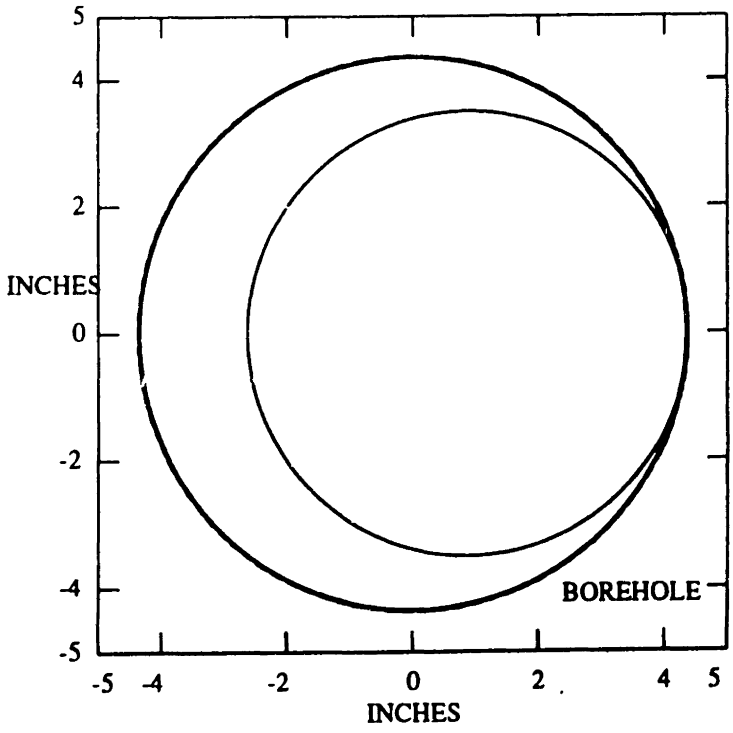

Figure 2.6: No Whirl, Pure Rotation, Rotation Speed -2.2 Hz, Whirling Speed 0 Hz

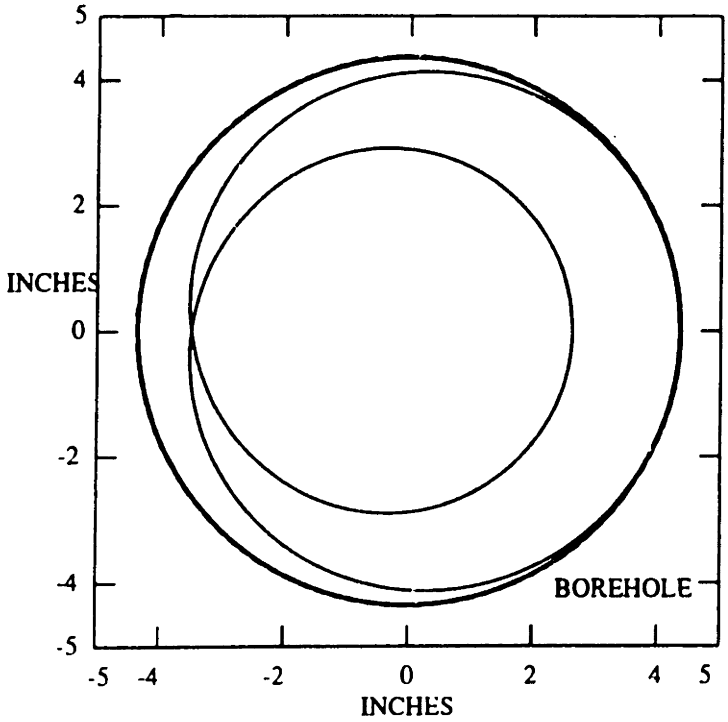

Figure 2.7: Forward Whirl With Slip, Rotation Speed -2.2 Hz, Whirling Speed -1.1 Hz

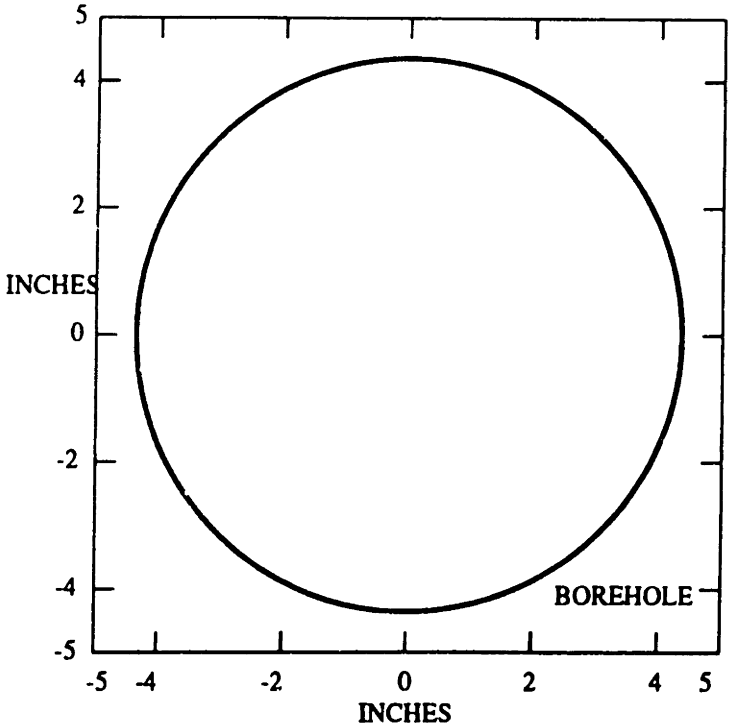

Figure 2.8: Synchronous Whirl With Slip, Rotation Speed -2.2 Hz, Whirling Speed -2.2 Hz

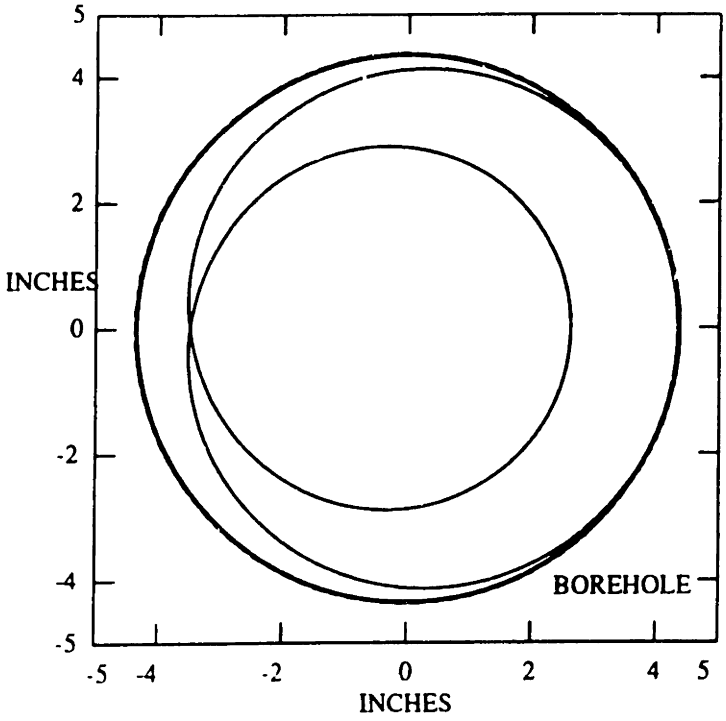

Figure 2.9: Forward Whirl With Forward Slip, Rotation Speed -2.2 Hz, Whirling Speed -3.3 Hz

2.3 Motion Seen From the Rotating Coordinate System Ox'y'

This coordinate system rotates at Ω about the center of the borehole, point O. In this coordinate system, the center of the collar, point A, would be at a distance R_1 from O and would not move, as depicted in Figure 2.10. Any other fixed point, such as B or P, on the drill collar will appear to rotate at $\omega - \Omega$ in the rotating frame of reference about an apparent center displaced from O an amount equal to R_1. Figure 2.10 also shows the locus of two points B and P as seen from the Ox'y' rotating frame. P is a point on the surface of the collar, and lies on an axis x'', which rotates with the collar. This point appears to go in circles at a rate $\omega - \Omega$, with a radius R_2. Point B simulates the location of the accelerometers in the collar. They are not on the outer circumference of the collar, but are at a lesser distance from the center. That point, B, would appear to move as shown, also a circle with radius R_3, centered at R_1 from O. Point B also is also assumed to be located on the x'' axis, which is fixed to the

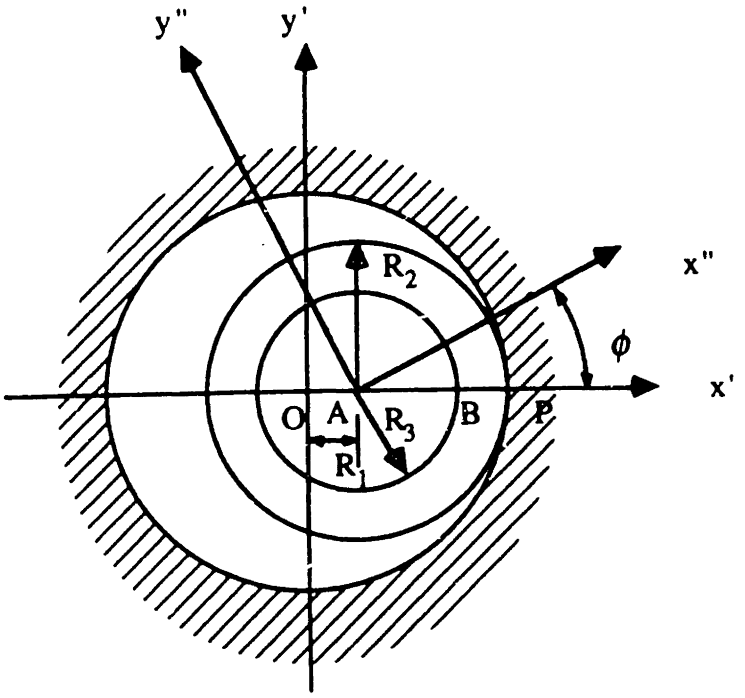

Figure 2.10: Points on the Drill Collar

collar.

2.4 Measurements Taken in a Rotating Reference Frame Under Pure Whirl Condition

2.4.1 Bending Moments $B_{x'}$ and $B_{y'}$

Bending moments are determined by the curvature of the beam as computed with respect to the neutral axis. In this case, the neutral axis coincides with A, the center of the collar. The deflection of the collar center as seen in the rotating frame Ox'y' is designated $v_0(z)$ and is assumed to be given by :

$$v_0(z) = R_1 \sin(\frac{\pi z}{L}) \tag{2.1}$$

$v_0(z)$ defines a radial distance from the borehole center(z axis) to the center of the collar. $v_0(z)$ is, therefore, the whirl radius. The function $\sin(\frac{\pi z}{L})$ accounts for the

radial deflection of the collar center as a function of the distance, z, along the axis from the bit, as shown in Figure 2.11. Here it has been assumed that the whirl deflected shape of the collar is half a sine wave between the bit and the first stabilizer. Figure 2.10 was drawn assuming one was at the midspan of the collar. At any other z, the distance to the center of the circle made by B and P would be given by $R_1 \sin(\frac{\pi z}{L})$, and the radii of the circle R_2 and R_3 would not change. At the bit, for example, the points B and P as seen in the rotating frame Ox'y' would be circles centered at O and moving at an angular rate of $\omega - \Omega$.

The bending moment corresponding to $v_0(z)$ is given by the moment curvature relationship

$$\underline{B}(z) = EI\frac{d^2v_0}{dz^2} = \frac{EI\pi^2}{L^2}R_1 \sin(\frac{\pi z}{L}) \tag{2.2}$$

In the examples drawn from the Shell-NL fields experiments, the bending moment $\underline{B}(z)$ was measured by two perpendicularly mounted strain gages in the Ax"y" system, which rotates with the collar. But note that $\underline{B}(z)$ is a two vector components in the Ax'y' system, with unit vectors i' and j', because the strain gages measure the strain from the undeflected position, which is the center of the hole.

$$\underline{B}(z) = \underline{B}(z)[\sin(\omega - \Omega)ti' + \cos(\omega - \Omega)tj'] \equiv B_{x'} + B_{y'} \tag{2.3}$$

In the example given, the distance, L, from the bit to the center of the stabilizer was 59.2 feet. The collar outside diameter was 7.0 inches, in an 8.375 inches hole. A midpoint deflection equal to a clearance of .875 inches would lead to a midpoint bending moment of 3525 foot-pounds. In the Shell-NL tests, the strain gage location was typically nine feet above the bit. At the measurement location nine feet above the bit, the measured bending moment would be reduced to 1600 foot pounds. The bending moment measurement can be used directly to interpret the whirling motions of the collar. The magnitude of the bending moment is simply given by

$$\underline{B}(z = 9) = (B_{x'}^2 + B_{y'}^2)^{\frac{1}{2}} \tag{2.4}$$

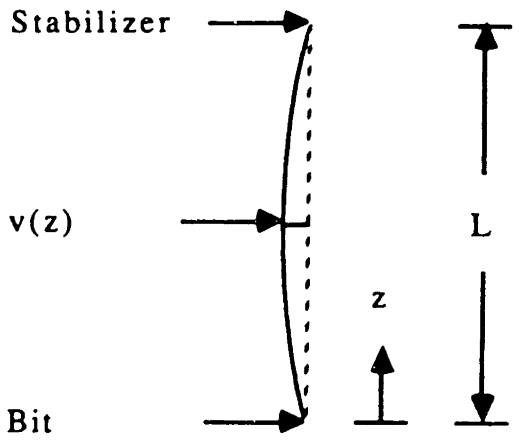

Figure 2.11: Whirl Deflected Shape

A phase angle can be estimated from $B_{x'}$ and $B_{y'}$;

$$\phi(t) = \tan^{-1}(\frac{B_{x'}}{B_{y'}}) = \tan^{-1}\frac{sin(\omega - \Omega)t}{cos(\omega - \Omega)t} = (\omega - \Omega)t \tag{2.5}$$

$\phi(t)$ is simply the phase angle which accumulates at the rotation speed of the collar as measured in the Ox'y' system. Therefore, from the bending moment measurements, the magnitude of the whirl can be estimated, and from the phase angle the difference between whirl and rotation rate can be determined, but not unique values of ω and Ω. In contrast, a magnetometer is insensitive to whirl and only sees the rotation of the collar with respect to the fixed reference frame. Its output is sensitive to the rotation rate ω, but provides no information regarding the whirl rate Ω.

Consider the different whirling conditions described in Figure 2.2 The values of ω, Ω, and $\omega - \Omega$ are summarized in the following table for all cases a through g. Note for this particular table the relative contact velocity with the wall is also presented.

$$v = R_1\Omega + R_2\omega \tag{2.6}$$

where R_1= 0.875 inches , R_2=3.5 inches.

Table 2.1: Rotation Rate, Whirl Rate, and Slip Velocity

Case		$\omega/2\pi$	$\Omega/2\pi$	$(\omega-\Omega)/2\pi$	$\mid v \mid$
a	Backward whirl with slip	-2.2	9.9	-12.1	.50
b	Backward whirl, no slip	-2.2	8.8	-11	0
c	Backward whirl, forward slip	-2.2	2.2	-4.4	3.02
d	No whirl, pure rotation	-2.2	0	-2.2	4.03
e	Forward whirl with slip	-2.2	-1.1	-1.1	4.53
f	Synchronous whirl with slip	-2.2	-2.2	0	5.04
g	Forward whirl with forward slip	-2.2	-3.3	1.1	5.54

where v is expressed in ft/sec. Note that in all cases $\frac{\omega}{2\pi}$=-2.2 Hz., where the minus sign indicates clockwise rotation looking down the hole(turning to the right). This would be the frequency of the peak one would observe in a spectrum of a magnetometer output. If one were to compute a spectrum of the time history of either $B_{x'}$ or $B_{y'}$, the peak would occur at the frequency $\mid \omega - \Omega \mid$. The total magnitude $\underline{B}$ does not vary with time. A polar plot of $\underline{B}$ and $\phi(t)$ would produce a circle with a radius $\underline{B}$, an angular velocity of $\omega - \Omega$, and rotation angle $\phi(t)$ equal to $(\omega - \Omega)t$.

The phase rates $\omega - \Omega$ has a physical significance. It represents the frequency of bending stress cycles experienced by the collar. For example, synchronous whirl, case f in table 2.1, results in no bending fatigue. However, it has a relatively high tangential velocity and, therefore, would tend to abrasively wear out the collar. On the other hand, case b, backward whirl with no slip, has zero tangential velocity and hence no wear. However, for this particular case the bending cycles would occur at approximately five times the rotation rate.

2.4.2 Acceleration Measurements with Radial and Tangentially Mounted Accelerometers Fixed to the Collar at a Radius R_3

Accelerometers measure absolute acceleration regardless of reference frame. Therefore, a radially oriented accelerometer mounted at a radius R_3 from the collar center would respond to the radial acceleration, $R_3\omega^2$, with respect to the center of the collar, as well as the component of the whirl acceleration of the collar center in the direction of the radially mounted accelerometer. This component is given by $R_1\Omega^2\cos(\omega-\Omega)t$. A tangential accelerometer would not feel any centripetal acceleration due to the collar rotation, but would respond to the tangentially oriented component of the whirl acceleration of the collar center. Therefore, we may write

$$a_r = R_1\Omega^2\cos(\omega-\Omega)t + R_3\omega^2 \tag{2.7a}$$

$$a_t = R_1\Omega^2\sin(\omega-\Omega)t \tag{2.7b}$$

where a_r is the radial acceleration, and a_t is the tangential acceleration. If the accelerometers are of the piezoelectric type, they can not measure constant acceleration components. Thus, the $R_3\omega^2$ term of the radial acceleration would not be measured, and the acceleration magnitude as measured would be

$$\underline{a} = (a_r^2 + a_t^2)^{\frac{1}{2}} = R_1\Omega^2 \tag{2.8}$$

and the phase angle

$$\phi(t) = tan^{-1}(\frac{a_t}{a_r}) = (\omega-\Omega)t \tag{2.9}$$

In the case of synchronous whirl, $\omega-\Omega=0$ and both $a_r(t)$ and $a_t(t)$ would not vary with time. In that case, the output of the accelerometers would be zero, due to the low frequency limitations of piezoelectric accelerometers. In reality, the drill collar may exhibit dynamic behavior other than pure whirling motion as described thus far. For example, torsional vibration will lead to non-zero tangential acceleration. In the previous discussion of acceleration and bending measurements, the phase angle

$\phi(t)=(\omega-\Omega)t$ and $\ddot{\phi}=0$. Torsional vibration would introduce a tangential acceleration component $R_3\ddot{\phi}$. Similarly, transient impacts with the wall would cause tangential and radial accelerations which are not as simple as cases of pure whirl. Bending data are in practice very difficult to interpret when non-whirling caused vibration occurs. An example is discussed in the next section.

2.5 Measurements Taken on a Rotating Frame With Simultaneous Whirling and Bending Vibration

Rotation and mass eccentricity cause a shaft to whirl. The amplitude of the whirling depends on the eccentricity, and on the closeness of the rotation speed and the bending natural frequencies of the shaft. The whirling amplitude grows larger as the rotation speed approaches one of the natural frequencies. But as the collar whirls, bending vibrations can also be excited, for example, by lateral or axial dynamic forces. Depending on the reference frame, these motions may seem simple or very complex.

An observer in the fixed coordinate system describes synchronous whirl as a circular motion of the shaft. But to an observer staying in the center of the coordinate system $OX'Y'$, rotating at Ω, whirl is just a constant deflection. Assume that in addition to this constant deflection, the rotating observer also witnesses a simple circular motion of the center of the shaft about the constant deflection center. The equations describing the motion of the shaft center as seen by this person are:

$$x'(t) = R_{x'}\cos\omega_n t \tag{2.10a}$$

$$y'(t) = R_{y'}\sin\omega_n t \tag{2.10b}$$

where $R_{x'}$ and $R_{y'}$ are the amplitude of the bending vibration and ω_n is the bending vibration frequency relative to the rotating coordinate system. The trajectory seen from a non-rotating reference frame is given by:

$$x(t) = R_1\cos(\omega t) + R_{x'}\cos(\omega_n t)\cos(\Omega t) - R_{y'}\sin(\omega_n t)\sin(\Omega t) \tag{2.11a}$$

$$y(t) = R_1\sin(\omega t) + R_{x'}\cos(\omega_n t)\sin(\Omega t) + R_{y'}\sin(\omega_n t)\cos(\Omega t) \tag{2.11b}$$

Figures 2.12 and 2.13 give examples of the trajectories of the shaft center as seen from both rotating and non-rotating frame of references, assuming two dimensional bending motion as mentioned above. These figures are plotted with the following parameter values. The hole clearance is assumed to be large enough that no wall contact occurs.

R_1 = 0.875 inches

$R_{x'}$ = 1.0 inches

$R_{y'}$ = 1.0 inches

Ω = -2.2 Hz = ω, forward synchronous whirl

ω_n = -3.0 Hz

The motion is circular with respect to the rotating coordinate system, but the observers in the fixed coordinate system will see much more complicated motions. This example not only illustrates the differences in the appearance of the motion as seen in the fixed and moving frames, but also has a useful physical interpretation which will be illustrated in the experimental results. A whirling shaft excited by axial forces will respond with orbital motion superposed on the whirl motions just as in this example.

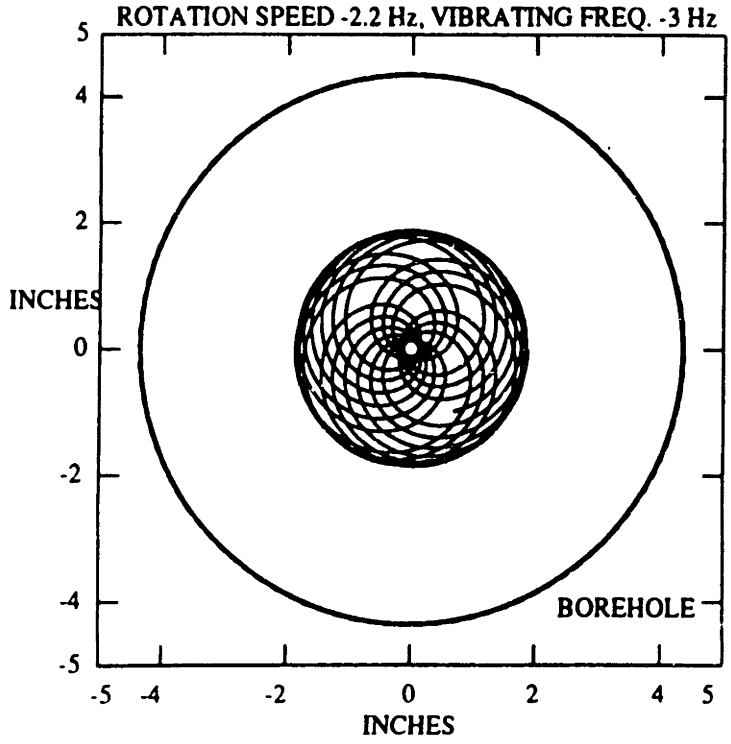

Figure 2.12: Motion Seen From the Fixed Coordinate System

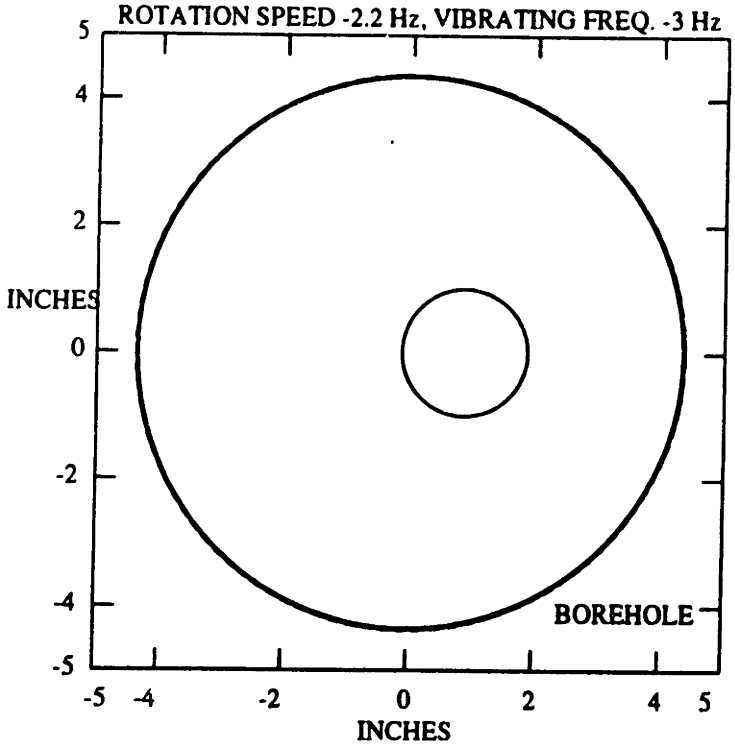

Figure 2.13: Motion Seen from the Rotating Coordinate System

Chapter 3

The Bending Natural Frequencies of Rotating Drill Collars

The bending vibration of the BHA is less well understood than torsional or axial vibration. Relatively, few papers have been devoted to the study of this phenomenon. The lack of research is partly due to the fact that bending vibrations downhole seldom propagate to the top, and to the lack of downhole measurements. Therefore, we begin with the discussion of the bending vibration of the drill collars.

3.1 Basic Configurations of the BHA

The arrangement of the stabilizers in the BHA affects the direction of the borehole. Depending on the location of the stabilizers, BHAs can be categorized as building, holding, or dropping assemblies. Figure 3.1 shows five configurations of the BHA. According to drilling practice, BHA no.1 is rated as a dropping assembly; BHA no.2 is found to be a very strong dropping assembly; BHA no.3 is rated as a very strong building assembly; BHA no.4 is found to act as a good holding assembly; BHA no.5 can be used as a weak building or a weak dropping assembly, depending on hole geometry and the interaction between the stabilizer and the formation. The placement of the stabilizers also affects the bending natural frequencies of the BHA. The simpliest approach, and the one taken here, is to model the effect of the bit and stabilizers with equivalent boundary conditions. Thus, a BHA is modelled as an axisymmetric,

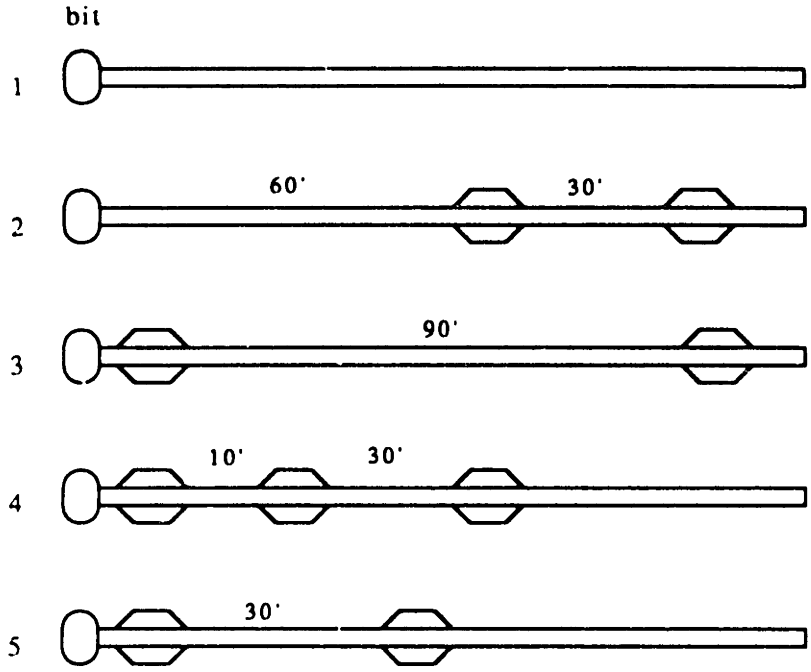

Figure 3.1: Several Configurations of the BHA

rotating, multispan beam. The spans are determined by the placement of the bit and stabilizers. With this approach, BHA number 2 in Figure 3.1 might be modelled as a two span beam that is hinged at the bit, restrained in displacement at the first stabilizer. and given a displacement and moment spring restraint at the second stabilizer. Such a model, then, approximates the effect of the BHA above the second stabilizer by a simple spring. Depending on the value of the spring constant, this restraint can be varied from a simple hinged to a built-in (fixed) condition. This simple approach will provide estimates of the natural frequencies and mode shapes for bending vibration between the bit and the second stabilizer only.

3.2 Theoretical Background

Figure 3.2 shows a section of BHA near the bit. The coordinate systems for the drill collars are shown in Figure 3.3. The homogeneous governing equation for bending vibration for a rotating beam in the x direction is [42]:

$$A\rho C_M\ddot{x} = -EI\frac{\partial^4 x}{\partial z^4} + Q\frac{\partial^3 x}{\partial z^3} - (C_E + C_I)\dot{x} + C_I\omega y$$
$$-A\rho gh\cos\phi[(l-z)\frac{\partial^2 x}{\partial z^2} - \frac{\partial x}{\partial z}] + A\rho C_M a\omega^2\cos\omega t \qquad (3.1)$$

the y direction is:

$$A\rho C_M\ddot{y} = -EI\frac{\partial^4 y}{\partial z^4} - Q\frac{\partial^3 y}{\partial z^3} - (C_E + C_I)\dot{y} - C_I\omega x$$
$$-A\rho gh\cos\phi[(l-z)\frac{\partial^2 y}{\partial z^2} - \frac{\partial y}{\partial z}] + A\rho C_M b\omega^2\sin\omega t - A\rho gh\sin\phi \qquad (3.2)$$

if complex notation $s' = x + iy$ and $e' = a + ib$ are used, and dividing through by $A\rho C_M$, then

$$\ddot{s}' + \frac{C_E + C_I}{A\rho C_M}\dot{s}' + \frac{EI}{A\rho C_M}\frac{\partial^4 s'}{\partial z^4} + i\frac{Q}{A\rho C_M}\frac{\partial^3 s'}{\partial z^3}$$
$$+\frac{gh\cos\phi}{C_M}[(l-z)\frac{\partial^2 s'}{\partial z^2} - \frac{\partial s'}{\partial z}] - i\frac{C_I\omega}{A\rho C_M} = \omega^2 e' e^{i\omega t} - i\frac{gh\sin\phi}{C_M} \qquad (3.3)$$

The definition of each symbol is

A = cross sectional area of collar

ρ, ρ_m = density of steel and mud

C_E, C_I = external and internal damping

EI = flexural rigidity

g = gravity constant

ϕ = slant angle of drill collar

C_M = mass coefficient of collar = 1+(added mass of mud per unit length + mud mass per unit length trapped inside the collar)/collar mass per unit length

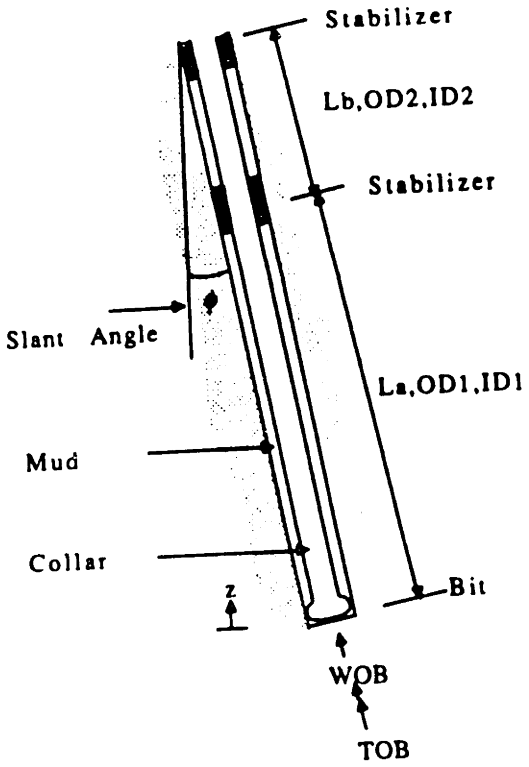

Figure 3.2: BHA Near the Bit

h = $1-\frac{\rho_m}{\rho}$

l = weight on bit$/A\rho gh\cos\phi$

Q = torque

ω = rotation speed of the drill collar

e' = mass eccentricity of the collar

The undamped natural frequencies and mode shapes for the non-rotating drill collars may be sought by first setting the damping and rotating speed, ω, to zero, and assuming static side force does not affect the natural frequency. The equations of motion can be expressed in a dimensionless form as follows. Let L_a = length of drill collar form the bit to the first stabilizer

$$\omega_0^2 = \frac{EI}{A\rho C_M L_a^4} \tag{3.4a}$$

$$w = \frac{z}{L_a} \tag{3.4b}$$

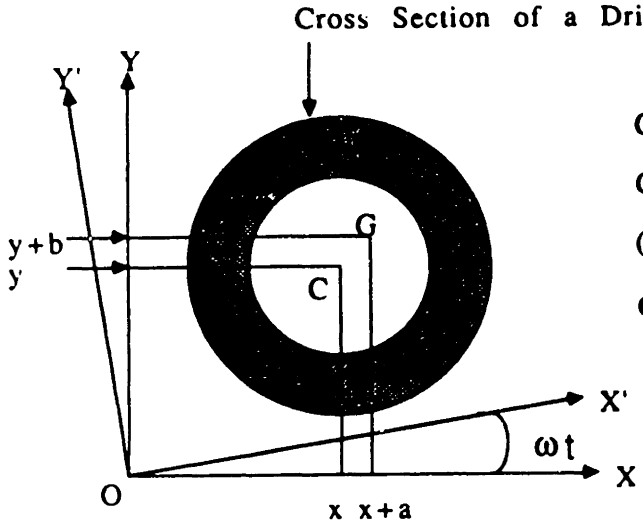

G : gravity center

C : geometric center

(a,b) : eccentricity of the collar

ω : rotation speed of the collar

OXY : fixed reference frame

OX'Y' : rotating reference frame

Figure 3.3: Coordinate System

$$\tau = \omega_0 t \tag{3.4c}$$

$$s = \frac{s'}{L_a} \tag{3.4d}$$

$$l_1 = \frac{l}{L_a} \tag{3.4e}$$

then

$$\frac{\partial^2 s}{\partial \tau^2} + \frac{\partial^4 s}{\partial w^4} + i\frac{QL_a}{EI}\frac{\partial^3 s}{\partial w^3} + \frac{gh\cos\phi}{L_a C_M \omega_0^2}[(l_1 - w)\frac{\partial^2 s}{\partial w^2} - \frac{\partial s}{\partial w}] = 0 \tag{3.5}$$

By separating the time and spatial variables and using the central difference method to replace the spatial derivatives, the differential equation can be transformed into a system of algebraic equations. For details see Appendix A.

$$[D][s] = 0 \tag{3.6}$$

where

[D] is a n×n finite difference matrix

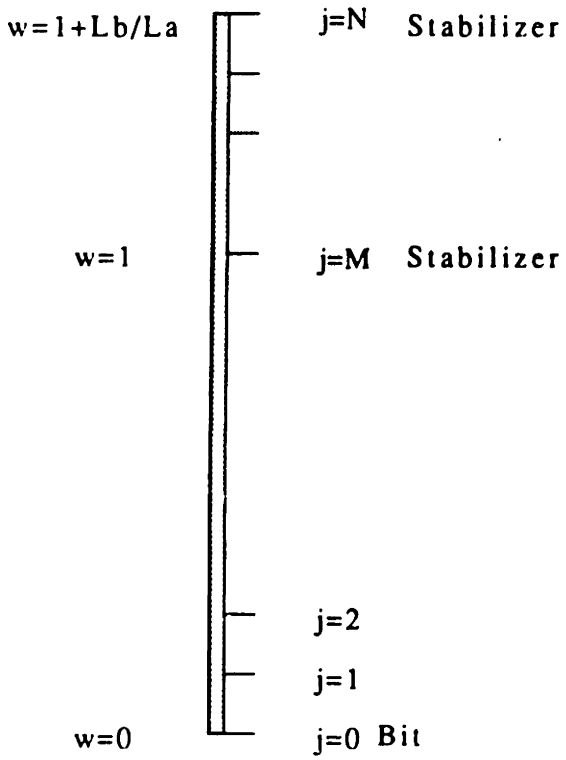

Figure 3.4: Discretization of the Drill Collar

[s] is a n×1 vector representing the non-dimensionalized displacements

The discretization of the collar is shown in Figure 3.4. The eigenvalues and eigenvectors of the matrix [D] are the natural frequencies and mode shapes of the non-rotating drill collar. The eigenvalue problem as described above for a two span beam has been implemented in a program known as BEND2PC.

3.3 Added Mass Coefficient of a Rod in a Confined Hole

The added mass coefficient of mud is a function of wall clearance and the viscosity of the mud [11]. Table 3.1 shows the added mass coefficient under various combinations of S and R/r, where

$S = \omega r^2/\nu$

ν = kinematic viscosity of the mud

Table 3.1: Added Mass Coefficient of a Vibrating Rod in a Confined hole

R/r \ S	500	1000	2000	3000	5000
1.2	6.88	6.83	6.54	6.38	6.21
1.3	4.86	4.63	4.43	4.34	4.24
1.4	3.75	3.57	3.43	3.37	3.31
1.5	3.11	2.97	2.86	2.81	2.76
1.6	2.70	2.57	2.49	2.45	2.42
1.7	2.41	2.31	2.23	2.20	2.17
1.8	2.19	2.11	2.05	2.02	1.99
1.9	2.04	1.96	1.90	1.88	1.85
2.0	1.92	1.84	1.79	1.77	1.74
2.2	1.74	1.67	1.63	1.61	1 59
2.4	1.62	1.56	1.52	1.50	1.48
2.6	1.53	1.47	1.44	1.42	1.41
2.8	1.46	1.41	1.38	1.36	1.35
3.0	1.42	1.36	1.33	1.31	1.30
3.5	1.33	1.28	1.25	1.24	1.23
4.0	1.27	1.23	1.21	1.19	1.18
5.0	1.22	1.18	1.15	1.13	1.12
6.0	1.19	1.15	1.12	1.11	1.10
8.0	1.16	1.12	1.10	1.08	1.07
10.0	1.14	1.11	1.08	1.07	1.06

R = radius of the hole

r = outer radius of the collar

ω = vibration frequency in radians per second

The coefficients in Table 3.1 can also be obtained through following formula,

$$C_m = Re\left(\frac{[\alpha^2(1+\gamma^2) - 8\gamma]\sinh(\beta-\alpha) + 2\alpha(2-\gamma+\gamma^2)\cosh(\beta-\gamma) - 2\gamma^2\sqrt{\alpha\beta} - 2\alpha\sqrt{\frac{\alpha}{\beta}}}{\alpha^2(1-\gamma^2)\sinh(\beta-\alpha) - 2\alpha\gamma(1+\gamma)\cosh(\beta-\alpha) + 2\gamma^2\sqrt{\alpha\beta} + 2\alpha\sqrt{\frac{\alpha}{\beta}}}\right) \tag{3.7}$$

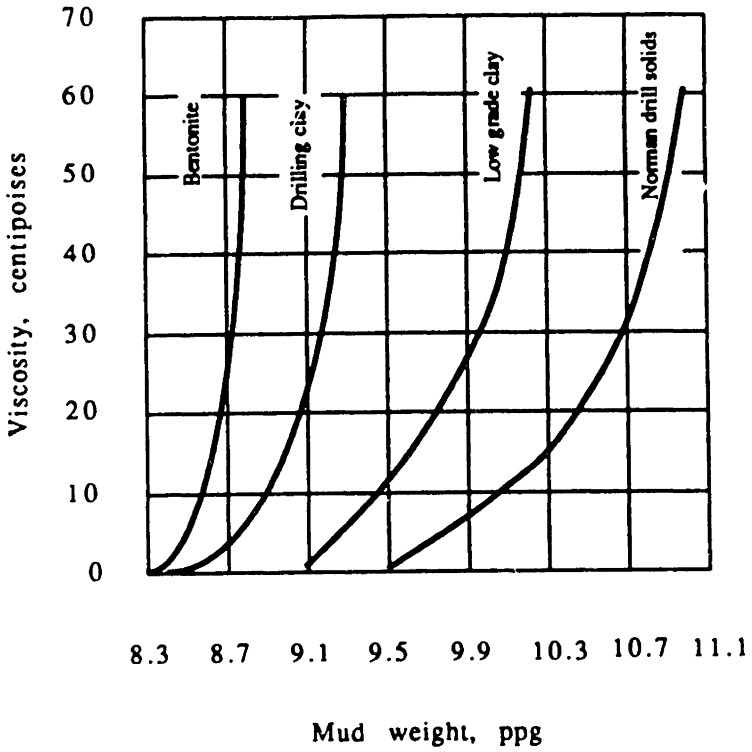

Figure 3.5: Viscosity of Drilling Muds

where Re indicates the real part of a complex quantity, $\alpha = kr$, $\beta = kR$, $\gamma = \frac{r}{R}$, and $k = \sqrt{i\frac{\omega}{\nu}}$. Equation 3.7 is valid if both α and β are greater than 10. Figure 3.5 shows the viscosity for various drilling muds. To convert viscosity from centipoises to kinematic viscosity in ft^2/sec, the following formula are needed.

poises= centipoises/100

ρ = mass density of the mud $(slug/ft^3)$

ν = kinematic viscosity (ft^2/sec) = poises/497ρ

3.4 Effects of WOB and TOB on the Bending Vibration

A numerical example is given to show the effects of the WOB and TOB on the bending natural frequencies. The numbers used as the inputs to the program

BEND2PC are shown in the Table 3.2. The first two modes are shown in Figure 3.6. Figure 3.7 shows the effect of the WOB and Figure 3.8 shows the effect of the TOB on the natural frequency of these modes. During drilling operations, the WOB may reach 50K lbs, but the TOB seldom exceeds 10,000 ft-lbs. So, from Figures 3.7 and 3.8, we can conclude that the effect of TOB on bending natural frequencies can usually be neglected. This assumption is made in chapter 4.

Table 3.2: BEND2PC Sample Input Data

59.8,35.23	(l1:bit to 1st stab. l2: 1st stab. to 2nd stab.,ft)
20,12	(no. of segments of l1 and l2)
6.83,2.93	(od and id of l1,inches)
6.25,2.81	(od and id of l2,inches)
0	(tob, ft-lbs)
30000	(wob, lbs)
8.8	(mud density, lbs/gal)
5	(added mass coeff. of the mud)
1	(boundary condition at 2nd stabilizer.1=fixed 0=depending on spring const.)
0.	(slant angle of the borehole, degrees)
4.28e09,15.2	(Young's Modulus and density of the collar,lbs/ft**2,slug/ft**3)
0.	(boundary condition at bit,1=fixed 0=depending on spring const.)
0.,0.	(moment spring constant at bit and stabilizer, ft-lbs/rad)

The simplified formula shown below gives a rough estimate of the first bending natural frequency with WOB and TOB effects. This equation was obtained assuming constant axial force, T, and constant torque, Q,

$$\omega_{WOB,TOB} = \omega\sqrt{1 - \frac{\frac{Q^2}{4EI} + T}{T_{crit}}} \tag{3.8}$$

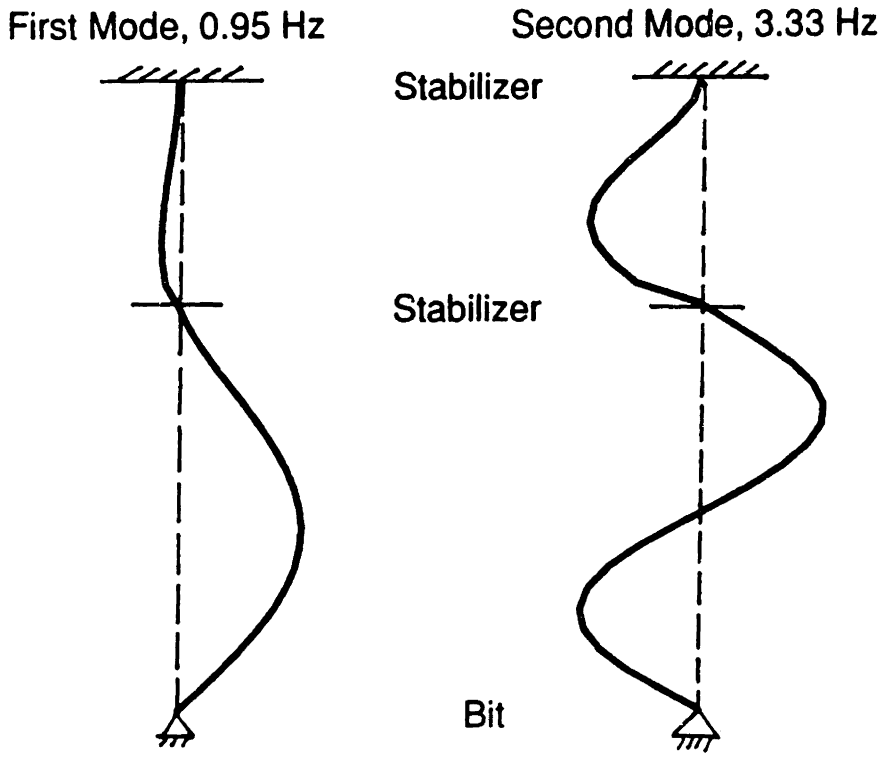

Figure 3.6: First Two Bending Modes

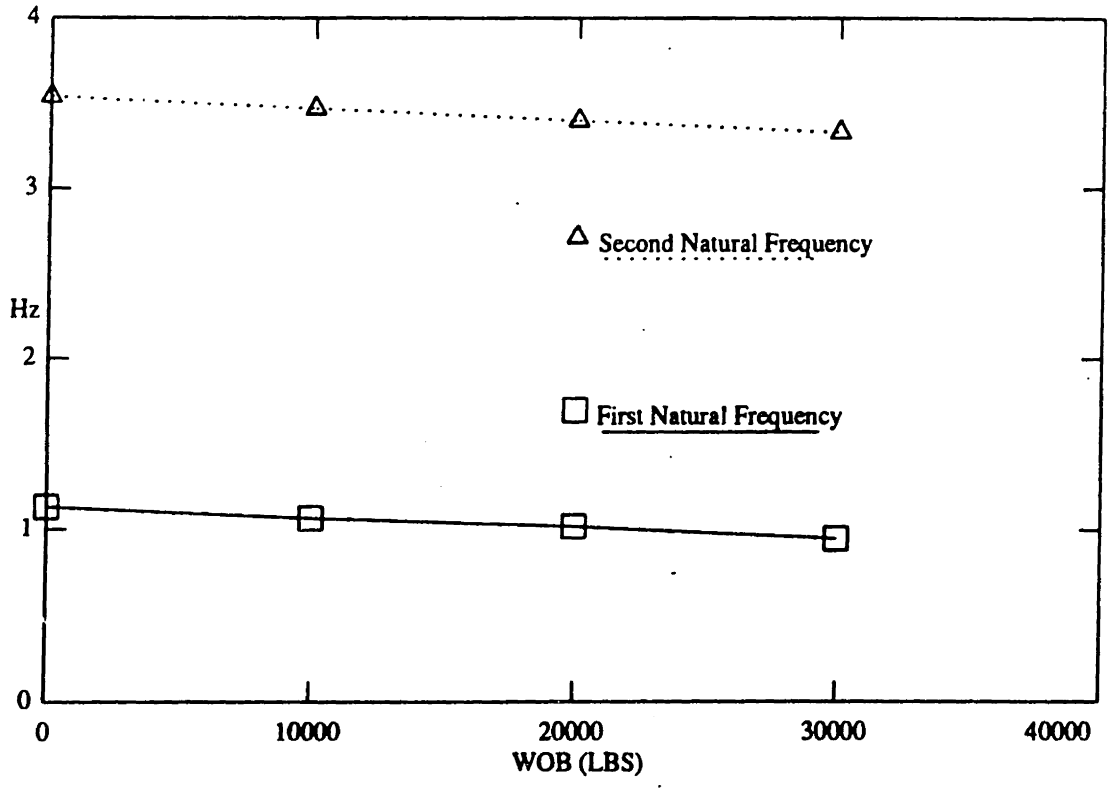

Figure 3.7: The Effect of WOB on Natural Frequency

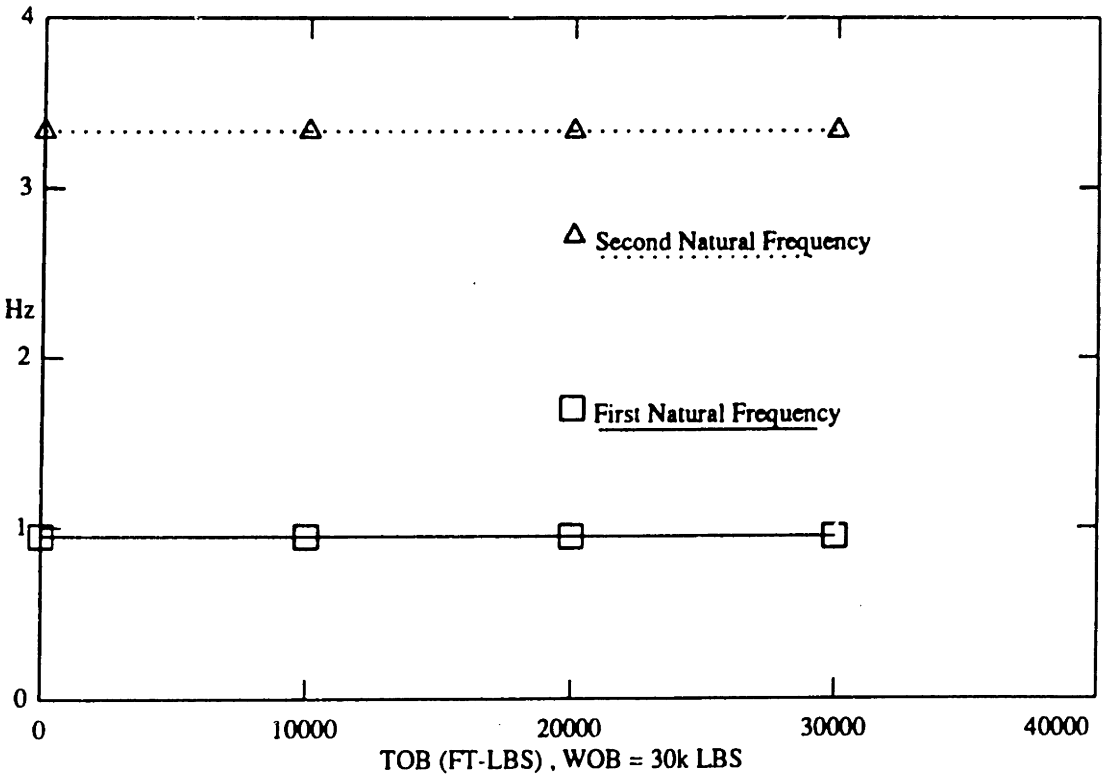

Figure 3.8: The Effect of TOB on Natural Frequency

where $\omega_{WOB,TOB}$, ω are the natural frequencies with and without WOB and TOB effects. T_{crit} is the first critical buckling load of a pin-pin beam of length L, and Q is the torque. In actual drilling, Q seldom exceeds 10K ft-lb, so the quantity $\frac{Q^2}{4EI}$ is small compared to T; therefore, the effect of the torque can usually be neglected.

3.5 Natural Frequencies of a Rotating Beam Expressed in a Rotating Coordinate System

Equation 3.3 describes the bending motion of a rotating beam with respect to a fixed reference frame. The bending vibration with respect to a reference frame rotating at speed ω can be obtained by substituting

$$s = r(\omega,\tau)e^{i\omega\tau} \tag{3.9a}$$

$$\dot{s} = (\dot{r} + i\omega r)e^{i\omega\tau} \tag{3.9b}$$

$$\ddot{s} = (\ddot{r} + i2\omega\dot{r} - \omega^2 r)e^{i\omega\tau} \tag{3.9c}$$

into equation 3.3, The resulting equation is :

$$\ddot{r}' + [\frac{C_E + C_I}{A\rho C_M} + i2\omega]\dot{r}' + \frac{EI}{A\rho C_M}\frac{\partial^4 r'}{\partial z^4} + i\frac{Q}{A\rho C_M}\frac{\partial^3 r'}{\partial z^3}$$
$$+\frac{gh\cos\phi}{C_M}[(l-z)\frac{\partial^2 r'}{\partial z^2} - \frac{\partial r'}{\partial z}] - (\omega^2 - i\frac{C_E\omega}{A\rho C_M})r' = \omega^2 e' - i\frac{gh\sin\phi}{C_M}e^{-i\omega t} \quad (3.10)$$

If ω_n is the bending natural frequency computed from a non-rotating drill collar, then, there are two eigenvalue solutions for the above equation, when damping is neglected:

$$\omega_n^+ = \omega_n + \omega \quad (3.11a)$$

$$\omega_n^- = \omega_n - \omega \quad (3.11b)$$

where ω_n^+ and ω_n^- are the two natural frequencies which would be observed in the rotating reference frame. Figure 3.9 is a graphical representation of equation 3.11a and 3.11b. Motion at ω_n^+ as observed in the rotating frame, would appear as circular paths opposite to the direction of rotation. Motion at ω_n^- is seen as circular orbits in the same direction as the rotation for ω_n^- positive, and in the opposite direction when ω_N^- is negative. For example, when $\omega = \omega_n$, then $\omega_n^- = 0$, this is the case known as forward synchronous whirl. The circular motion as seen in the rotating frame degenerates to a static displacement, with a frequency of $\omega_n^- = 0$. To demonstrate the effect of rotation on the frequency observed in the rotating coordinate system, we begin by examining the motion of a mass-spring system on a rotating disk. This system is shown in Figure 3.10. No eccentricity is assumed in this case to simplify the derivations. The equation of motion for this system corresponding to the stationary coordinate system, Oxy, is

$$x: \quad m\ddot{x} + kx = 0 \quad (3.12a)$$

$$y: \quad m\ddot{y} + ky = 0 \quad (3.12b)$$

The natural frequency corresponding to both x and y directions is $\omega_n = \sqrt{\frac{k}{m}}$. Depending on the amplitude and phase angle between the x and y motion, the mode

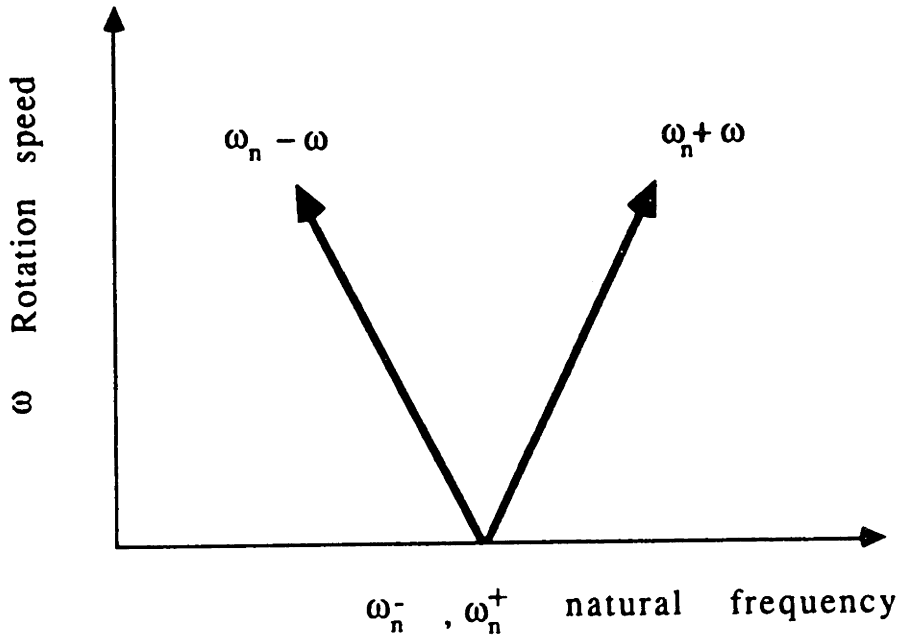

Figure 3.9: Frequencies Observed in a Rotating Coordinate

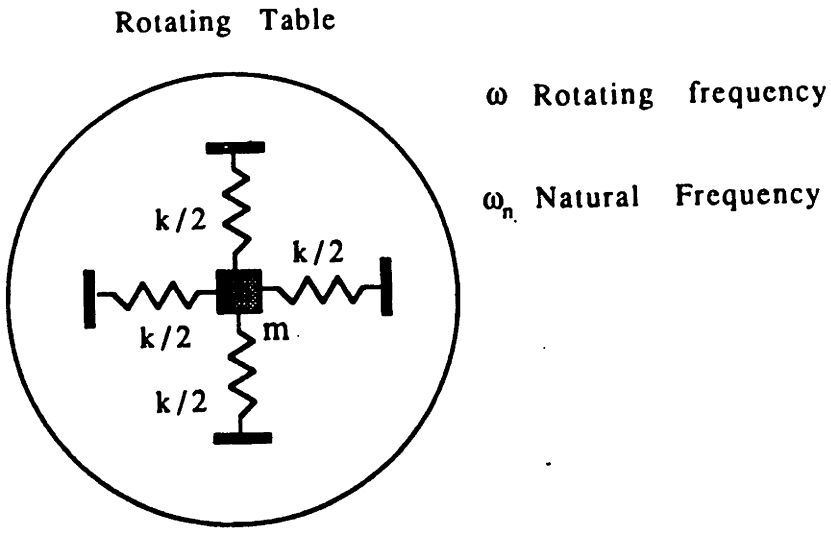

Figure 3.10: Mass-Spring System on a Rotating Table

shape can be circular, or elliptical, and may rotate in clockwise or counterclockwise direction. The equation of motion for this system corresponding to the rotating coordinate system, $Ox'y'$, is

$$x': \quad m(\ddot{x'} + 2\omega\dot{y'} - \omega^2 x') + kx' = 0 \tag{3.13a}$$

$$y': \quad m(\ddot{y'} - 2\omega\dot{x'} - \omega^2 y') + ky' = 0 \tag{3.13b}$$

where x' and y' are the coordinates fixed on the disk, m and k are the mass and stiffness respectively. The above equation can be written in operator form as,

$$x: \quad L_1 x' + L_2 y' = 0 \tag{3.14a}$$

$$y: \quad L_3 x' + L_4 y' = 0 \tag{3.14b}$$

where

$$L_1 = D^2 - \omega^2 + \omega_n^2 \tag{3.15a}$$

$$L_2 = 2\omega D \tag{3.15b}$$

$$L_3 = -2\omega D \tag{3.15c}$$

$$L_4 = D^2 - \omega^2 + \omega_n^2 \tag{3.15d}$$

$$D = \frac{d}{dt} \tag{3.15e}$$

The solutions to this system of differential equation are the roots of

$$\Delta = \begin{vmatrix} L_1 & L_2 \\ L_3 & L_4 \end{vmatrix} = 0 \tag{3.16}$$

By solving this equation, the homogeneous solutions for x' and y' can be written as follows :

$$x' = A_1 e^{-i(\omega_n+\omega)t} + A_2 e^{i(\omega_n-\omega)t} + A_3 e^{i(\omega_n+\omega)t} + A_4 e^{-i(\omega_n-\omega)t} \tag{3.17a}$$

$$y' = B_1 e^{-i(\omega_n+\omega)t} + B_2 e^{i(\omega_n-\omega)t} + B_3 e^{i(\omega_n+\omega)t} + B_4 e^{-i(\omega_n-\omega)t} \tag{3.17b}$$

The clockwise direction indicates the the direction of decreasing angle, and counterclockwise direction indicates the direction of increasing angle. Therefore, if the

direction of rotation of the drill collar is clockwise, indicating that the rotation rate is $-\omega$, then, the coefficients A_3, A_4, B_3, and B_4 will vanish. On the other hand, if the direction of rotation is counterclockwise, the coefficients A_1, A_2, B_1, and B_2 will vanish. The ratio of $\frac{A_n}{B_n}$ indicates the mode shape of their associated eigenvalues. For example, the ratio of $\frac{A_1}{B_1}$ shows the mode shape of eigenvalue $-i(\omega + \omega_n)$. The ratio of $\frac{A_1}{B_1}$ can be obtained by substituting equation 3.17a into equation 3.13b, and setting A_2, A_3, A_4, B_2, B_3, and B_4 equal to zero. Following this procedure, we can find that the mode shape for eigenvalues $-i(\omega_n \pm \omega)$ is $-i$, and the mode shape for eigenvalues $i(\omega_n \pm \omega)$ is i, if $\omega_n \pm \omega$ remains positive. This implies that x' and y' are equal in magnitude, but 90 degrees out of phase with each other, which would be seen as circular motion in the rotating frame. The direction of rotation depends on the sign of the eigenvalue. A positive eigenvalue indicates a counterclockwise rotation, whereas, a negative eigenvalue indicates a clockwise rotation. If we assume that there is an sinusoidal input force in the x' direction designated as $Pe^{i\omega_L t}$, the particular solution can be obtained by assuming the solution in the form

$$x' = A_1 e^{i\omega_L t} \tag{3.18a}$$

$$y' = B_1 e^{i\omega_L t} \tag{3.18b}$$

Substituting this into the equation of motion and solving for A_1 and B_1, we find that

$$A_1 = \frac{\omega^2 - \omega_L^2 - \omega^2}{\Theta} \tag{3.19a}$$

$$B_1 = \frac{i2\omega\omega_L}{\Theta} \tag{3.19b}$$

where Θ is

$$\Theta = (\omega^2 - \omega^2 - \omega_L^2)^2 - 4\omega^2\omega_L^2 \tag{3.20}$$

If we demand that $|A_1| = |B_1|$, then, it implies that $\omega_L = \omega \pm \omega_n$. Physically, it means that if the excitation frequency equals to one of the natural frequencies, then,

the motion of the mass is a circle with respect to an observer who stays in the center of the disk. Following a similar argument, it can be shown that if the excitation frequency frequency is not at a natural frequency, then the ratio of $\frac{A_n}{B_n}$ can not be 1.0. The resulting motion will be elliptical in shape.

3.6 Several Interpretations of the Results

The bending natural frequencies with respect to a fixed coordinate system determine the rotation speeds at which large amplitude forward synchronous whirl occurs. The closer the rotation speed comes to the natural frequencies as computed in a fixed reference frame, the larger the whirling amplitude. Synchronous whirl at this rotation speed may cause excessive wear on one side of the drill collar, or may result in backward whirl if the wall friction is sufficiently high. One the other hand, the natural frequencies with respect to a rotating coordinate system determine the frequencies of external excitations that will cause large bending vibration. Therefore, the excitations needed to drive the collar into large bending motion vary linearly with the rotation speed of the drill collar. Examples of bending vibration due to external excitation are shown in the experimental results in chapter six, which contains the predictions given above. Examples of forward and backward whirl are given in chapter seven.

Chapter 4

Axial Excitation of Bending Vibration

In actual drilling, dynamic axial forces are produced because of the interaction between the bit and the formations. These axial forces can induce bending vibration. There are two principal types of bending vibration resulting from axial forces. In this thesis, they are termed linear coupling and parametric coupling. These coupling mechanisms between axial forces in the drill string and bending vibrations are described in the following sections.

4.1 Linear Coupling of Axial Force and Bending

Linear coupling between the axial forces on the bit and bending vibration occurs frequently in real drilling assemblies, often superposed on other bending vibration phenomena. The source of linear coupling is initial curvature of the BHA, such as is depicted in Figure 4.1. Linear coupling is easy to visualize by taking a thin ruler or a piece of paper, giving it a slight curve, and then pressing axially on the ends. The object responds by additional bending in the plane of the initial curvature. The frequency of the bending and axial vibrations is the same. The coupling is made possible by the initial curvature. Linear coupling will not occur on a perfectly straight beam excited by an axial load which is less than the critical buckling load. However, if there is any initial curvature, an axial load will cause a lateral deflection. For

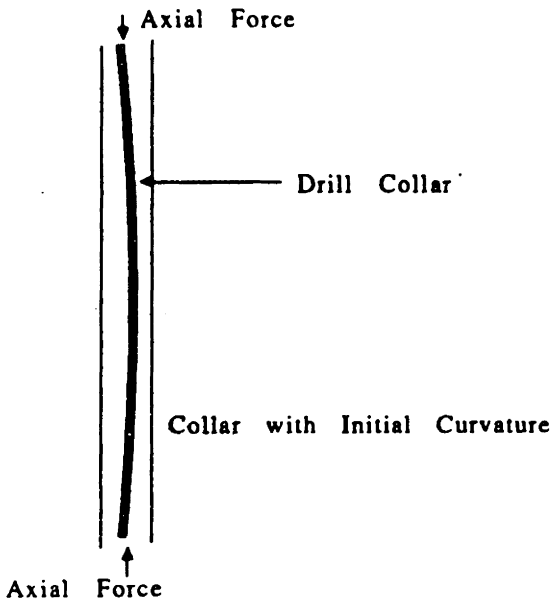

Figure 4.1: A Section of a Bent Collar

small amounts of curvature, the greater the initial curvature, the greater the lateral deflection. Of course, curvature is very common in bottom hole assemblies due to the combined effects of gravity and axial force in inclined holes. Whirling also results in curvature of the BHA and, therefore, also leads to coupling. Dynamic variations in the weight on bit then cause bending vibration to occur about the mean statically deflected shape.

4.2 Linearly Coupled Equations of Motion

The equations of motion describing coupled axial and bending vibration are given below for the non-rotating beam. Rotation will be introduced later. In the axial direction :

$$A\rho\frac{\partial^2 u}{\partial t^2} = \frac{\partial}{\partial z}EA(\frac{\partial u}{\partial z} - \kappa_y x + \kappa_x y) - EI(\kappa_x\frac{\partial^3 y}{\partial z^3} - \kappa_y\frac{\partial^3 x}{\partial z^3}) \tag{4.1}$$

in the x direction, where x is measured from the initially curved position:

$$\begin{aligned} A\rho C_M\ddot{x} &= -EI\frac{\partial^4 x}{\partial z^4} + Q\frac{\partial^3 x}{\partial z^3} - (C_E + C_I)\dot{x} \\ &- A\rho gh\cos\phi[(l-z)\frac{\partial^2 x}{\partial z^2} - \frac{\partial x}{\partial z}] + EA\kappa_y(\frac{\partial u}{\partial z} - \kappa_y x + \kappa_x y) \end{aligned} \tag{4.2}$$

in the y direction, where y is measured from the initially curved position:

$$A\rho C_M\ddot{y} = -EI\frac{\partial^4 y}{\partial z^4} - Q\frac{\partial^3 y}{\partial z^3} - (C_E + C_I)\dot{y} \qquad (4.3)$$
$$- A\rho gh\cos\phi[(l-z)\frac{\partial^2 y}{\partial z^2} - \frac{\partial y}{\partial z}] + EA\kappa_x(\frac{\partial u}{\partial z} - \kappa_y x + \kappa_x y)$$

where

κ_x = initial curvature along x direction = $\frac{d^2 x_0}{dz^2}$

κ_y = initial curvature along y direction = $\frac{d^2 y_0}{dz^2}$

where $x_0(z)$ and $y_0(z)$ are the initial curved shapes

This set of equations indicates that the coupling mechanism of axial and bending is the curvature of the drill collars. Without the curvature, the axial and bending vibration will respond independently, according to linear beam theory. A similar result may be found in [41]. The above equation was solved by central finite difference scheme. Figure 4.2 depicts the BHA model that was used for the calculations. It is a standard pendulum BHA with two stabilizers. The boundary conditions at the bit were specified as lateral displacements and bending moments equal zero. At the first stabilizer, the lateral deflection was zero. The boundary conditions at the second stabilizer were specified as lateral displacements and slopes equal zero. Due to the curvature induced by axial load, gravity , or eccentricity of the collars, the bending natural frequencies may shift slightly with respect to an unbent configuration. Figure 4.3 shows the effect of the curvature on the first bending natural frequency of the BHA shown in Figure 4.2. In this example, the initial deflection shape $v_0(z)$ was assumed to be in the first mode shape. The maximum value of v_0 occurs at the midpoint of the longer drill collar section. A measure of the initial curvature is given by the ratio $\frac{v_0(max)}{L_a}$, where L_a is the unsupported span length. This ratio is plotted versus the first mode bending natural frequency in Figure 4.3 The natural frequency, due to the coupling effect, decreases with increasing curvature. For a borehole with a radial wall clearance of 4 inches and a span of 59 feet, this ratio is approximately 0.005 resulting

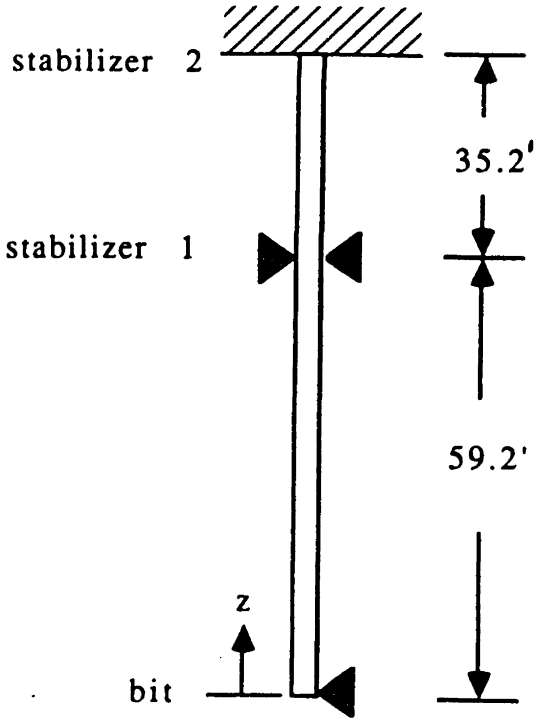

Figure 4.2: Drill String Model for the Linear Coupled Example

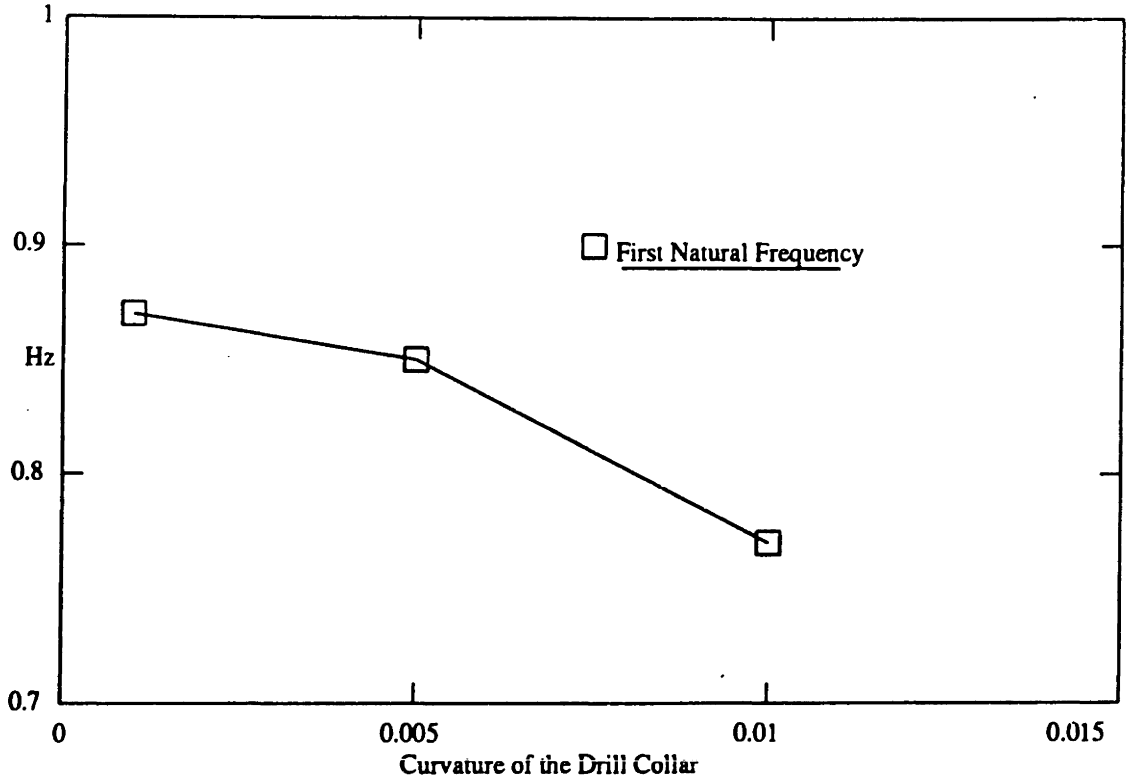

Figure 4.3: The Effect of the Curvature on the Natural Frequencies

in a decrease of less than 5 percent in natural frequency. To further understanding of linear coupling, one might consider the term $\frac{\partial u}{\partial z}$ in both x and y equations of motion. Physically, this term represents the axial strain along the drill string. If the axial strain were to vary harmonically in time due to dynamic variations in WOB, it would assume the form $\frac{du(z)}{dz}e^{i\omega t}$. This term may be thought of as the input forcing function, and because the equations are linear, the solution for both x and y will be harmonic at the same frequency.

In actual drilling practice, the borehole diameters are often only one to two inches larger than the drill collars. So, the curvature of the drill collars is limited by the diameter of the hole. In a pendulum BHA, the first stabilizer is placed about 60 ft above the bit; therefore, the curvature of the collar is very small, and the effect of the curvature on the drill collar bending natural frequency can be neglected, as mentioned above. Although the changes in bending natural frequency can be neglected, the curvature does induce bending vibration which may be problem. An example demonstrating this phenomenon will be shown in chapter 6.

4.3 The Effect of Rotation on the Linear Coupling Phenomena

The equation shown above is described in terms of a stationary coordinate system. But, as was mentioned in chapter 3, the natural frequency observed in a rotating coordinate system will vary with rotation rate. This also implies that the frequency of axial excitation needed to drive the collar into large resonant bending vibrations will change, according to the rotation speed of the drill collars. For example, if the drill string is stationary, the axial frequency needed to drive the collar at a bending resonance is equal to ω_n, the natural frequency of the drill collar, provided the curvature is small. But, as the drill string starts to rotate at ω, the axial frequency needed to drive the collar into bending resonance will change from ω_n to $|\omega_n \pm \omega|$. This concept is not intuitively obvious, but it is essential to understanding drill collar vibration.

The equations of motion expressed as seen in the rotating reference frame are as follows, in the axial direction :

$$A\rho\frac{\partial^2 u}{\partial t^2} = \frac{\partial}{\partial z}EA(\frac{\partial u}{\partial z} - \kappa_y x + \kappa_x y) - EI(\kappa_x\frac{\partial^3 y}{\partial z^3} - \kappa_y\frac{\partial^3 x}{\partial z^3}) \tag{4.4}$$

in the x direction:

$$\begin{aligned} A\rho C_M(\ddot{x} + i2\omega\dot{x} - \omega^2 x) &= -EI\frac{\partial^4 x}{\partial z^4} + Q\frac{\partial^3 x}{\partial z^3} - (C_E + C_I)\dot{x} \\ &- A\rho gh\cos\phi[(l-z)\frac{\partial^2 x}{\partial z^2} - \frac{\partial x}{\partial z}] + EA\kappa_y(\frac{\partial u}{\partial z} - \kappa_y x + \kappa_x y) \end{aligned} \tag{4.5}$$

in the y direction:

$$\begin{aligned} A\rho C_M(\ddot{y} + i2\omega\dot{y} - \omega^2 y) &= -EI\frac{\partial^4 y}{\partial z^4} - Q\frac{\partial^3 y}{\partial z^3} - (C_E + C_I)\dot{y} \\ &- A\rho gh\cos\phi[(l-z)\frac{\partial^2 y}{\partial z^2} - \frac{\partial y}{\partial z}] + EA\kappa_x(\frac{\partial u}{\partial z} - \kappa_y x + \kappa_x y) \end{aligned} \tag{4.6}$$

4.4 Bending Vibration of the BHA With Parametric Excitation Without Wall Contact

The bending vibration can be excited parametrically by the dynamic axial excitations. It occurs usually when the shaft is straight, and with strong dynamic axial forces coming from the bit rock interactions as shown in Figure 4.4. This phenomenon is most likely to occur in the section between bit and the first stabilizer in a pendulum assembly or the section above the uppermost stabilizer, if the BHA is vertical. The most distinguishing feature of parametrically excited vibration is that the bending response frequency is one half the axial excitation frequency. This phenomenon is demonstrated in the laboratory experiments described in chapter 6.

4.5 Equation of Motion

The following equation includes the effect of parametric axial excitation on bending vibration for a non-rotating beam. The definition of the symbols and the coordinate

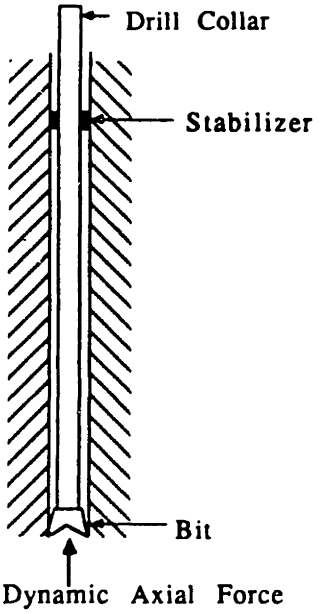

Figure 4.4: Drill Collar Under Axial Excitation

system are the same as in chapter 3,

$$A\rho C_M \frac{\partial^2 s'}{\partial t^2} + (C_E + C_I)\frac{\partial s'}{\partial t} + EI\frac{\partial^4 s'}{\partial z^4} + iQ\frac{\partial^3 s'}{\partial z^3} + A\rho gh\cos\phi[(l' - z)\frac{\partial^2 s'}{\partial z^2} - \frac{\partial s'}{\partial z}] = 0 \tag{4.7}$$

where l' is :

$$l' = \frac{T_s + T_d}{A\rho gh\cos\phi} \tag{4.8}$$

and T_s is the mean WOB, and T_d is the dynamic axial force,

$$T_d = EA\frac{\partial u}{\partial z} = T_b P(\omega, z)\cos\omega t \tag{4.9}$$

where

T_b : the amplitude of the weight-on-bit dynamic fluctuation at frequency ω

$P(\omega, z)$: force transfer function between the bit and the point z

u : axial displacement which satisfies

$$A\rho\frac{\partial^2 u}{\partial t^2} = EA\frac{\partial^2 u}{\partial z^2} \tag{4.10}$$

If the length of the section considered is short compared to the wave length of the axial vibration, $P(\omega, z)$ can be assumed to be unity. This is a realistic approximation near the bit in actual drilling conditions. Typical bottom hole assemblies consist of two or three drill collars below the first stabilizer. This section of drill collars is susceptible to parametric bending vibrations, due to large dynamic variations in the weight on bit. Usually, each drill collar is 30 feet long, so, the total length below the first stabilizer is less than 100 feet long. The axial wave length in steel drill collar is about 16,000 feet at a frequency of 1 Hz. So, we can neglect the dynamic axial stress variations along this section of the drill collar.

The equation above can be nondimensionalized using $w = \frac{z}{L}$, $\mathrm{l} = \frac{l'}{L}$ and $\tau = \omega_0^2 t$. The following equation is the nondimensionalized equation

$$\frac{\partial^2 s}{\partial \tau^2} + \frac{C_E + C_I}{A\rho C_M \omega_0}\frac{\partial s}{\partial \tau} + \frac{\partial^4 s}{\partial w^4} + i\frac{QL}{EI}\frac{\partial^3 s}{\partial w^3} + \frac{\rho g h \cos\phi}{C_M \omega_0^2}[(l-w)\frac{\partial^2 s}{\partial w^2} - \frac{\partial s}{\partial w}] = 0 \tag{4.11}$$

Equation 4.11 can be reduced to a system of linear equations by introducing a central finite difference scheme,

$$\begin{aligned}
\frac{\partial s}{\partial w} &= \frac{N}{2}[-s_{j-1} + s_{j+1}] \\
\frac{\partial^2 s}{\partial w^2} &= N^2[s_{j-1} - 2s_j + s_{j+1}] \\
\frac{\partial^3 s}{\partial w^3} &= \frac{N^3}{2}[-s_{j-2} + 2s_{j-1} - 2s_{j+1} + s_{j+2}] \\
\frac{\partial^4 s}{\partial w^4} &= N^4[s_{j-2} - 4s_{j-1} + 6s_j - 4s_{j+1} + s_{j+2}]
\end{aligned} \tag{4.12}$$

The matrix form of equation 4.11 is

$$\frac{d^2}{d\tau^2}[s] + \frac{C_E + C_I}{A\rho C_M \omega_0}\frac{d}{d\tau}[s] + [A][s] + i\frac{QL}{EI}[B][s] + \frac{gh\cos\phi}{C_M L \omega_0^2}[(l-w)[C][s] - [D][s]] = 0 \tag{4.13}$$

where

[A] = 4th order difference matrix

[B] = 3rd order difference matrix

[C] = 2nd order difference matrix

[D] = 1st order difference matrix

$[s] = [s_1, s_2 ..... s_N]^T$

The elements near the bit or stabilizers, in the finite difference matrix, depend on the boundary conditions. Therefore, these matrices also depend on the boundary conditions. If the terms with same order of differentiation are grouped, the above equation can be rewritten as :

$$\frac{d^2}{d\tau^2}[s] + \frac{C_E + C_I}{A\rho C_M \omega_0}\frac{d}{d\tau}[s] + ([P_s] + [P_d])[s] = 0 \tag{4.14}$$

where the matrix P_d representing the dynamic axial force at each element is

$$[P_d] = \frac{1}{A\rho C_M L^2 \omega_0^2} T_d [C] \tag{4.15}$$

and the matrix P_s representing the static force at each elements is

$$[P_s] = [A] + i\frac{QL}{EI}[B] + \frac{gh\cos\phi}{C_M L\omega_0^2}[(\frac{T_s}{A\rho gh L\cos\phi} - w)[C] - [D]] \tag{4.16}$$

where $[I]$ is the identity matrix. If the damping is ignored for the moment, and the equation is normalized using the eigenvectors of the undamped system, then, equation 4.14 becomes

$$\frac{d^2}{d\tau^2}[s] + ([F] + T_s[S])[s] = 0 \tag{4.17}$$

where [F] = $[E]^{-1}[P_s][E]$=

$$\begin{bmatrix} \frac{\omega_1^2}{\omega_0^2} & . & . & . \\ . & \frac{\omega_2^2}{\omega_0^2} & . & . \\ . & . & . & . \\ . & . & . & \frac{\omega_N^2}{\omega_0^2} \end{bmatrix}$$

and $\omega_1, ..., \omega_N$ are the natural frequencies of the non-rotating system, and [S] = $[E]^{-1}[P_d][E]$, where [E] is the matrix of the eigenvectors. The instability condition for

this system according to [23] is

$$\omega_i + \omega_j - T_b\eta < \omega < \omega_i + \omega_j + T_b\eta \tag{4.18}$$

where

$$\eta = (\frac{S_{ij}S_{ji}}{4\omega_i\omega_j})^{\frac{1}{2}} \tag{4.19}$$

where S_{ij} is the ij-element of matrix [S]. The parameter η is the slope of the boundary of the unstable regions. An increase in the slope will increase the size of the unstable regions. Figure 4.5 shows an example of the unstable region for a pinned-pinned Acrylic rod with ID=0 inches , OD= 0.375 inches, and 3 feet long. The density of the material is 2.68 $\frac{slugs}{ft^3}$, and the Young's Modulus is 5.75×10^7 psf. The figure is plotted with axial excitation frequency ω *vs.* amplitude of the dynamic axial force T_b. If the combination of ω and T_b is inside the unstable region, the amplitude of bending vibration will grow until it is ultimately restrainted by the borehole. In the example given above, the unstable region was found for a condition with no external damping. With no damping, the instability may be driven by an arbitrarily small excitation, T_b. The effect of damping is to raise the threshold of excitation which can produce the instability. The greater the damping, the higher the threshold. A plot of the unstable region will look similar as the one shown, except that it can not extend below the threshold value. A detailed discussion of the effect of damping on the unstable region can be found in [24]

4.6 String under Dynamic Axial Tension

As an aid to understanding parametric excited bending vibration of drill collars, consider the string depicted in Figure 4.6. The string is shown passing through a pair of pinch rollers, which is the lower boundary condition, and continues on to a tension measuring device. If the string has a static component of tension T_0, and a known mass per unit length, μ, then the first natural frequency of the string can be computed as,

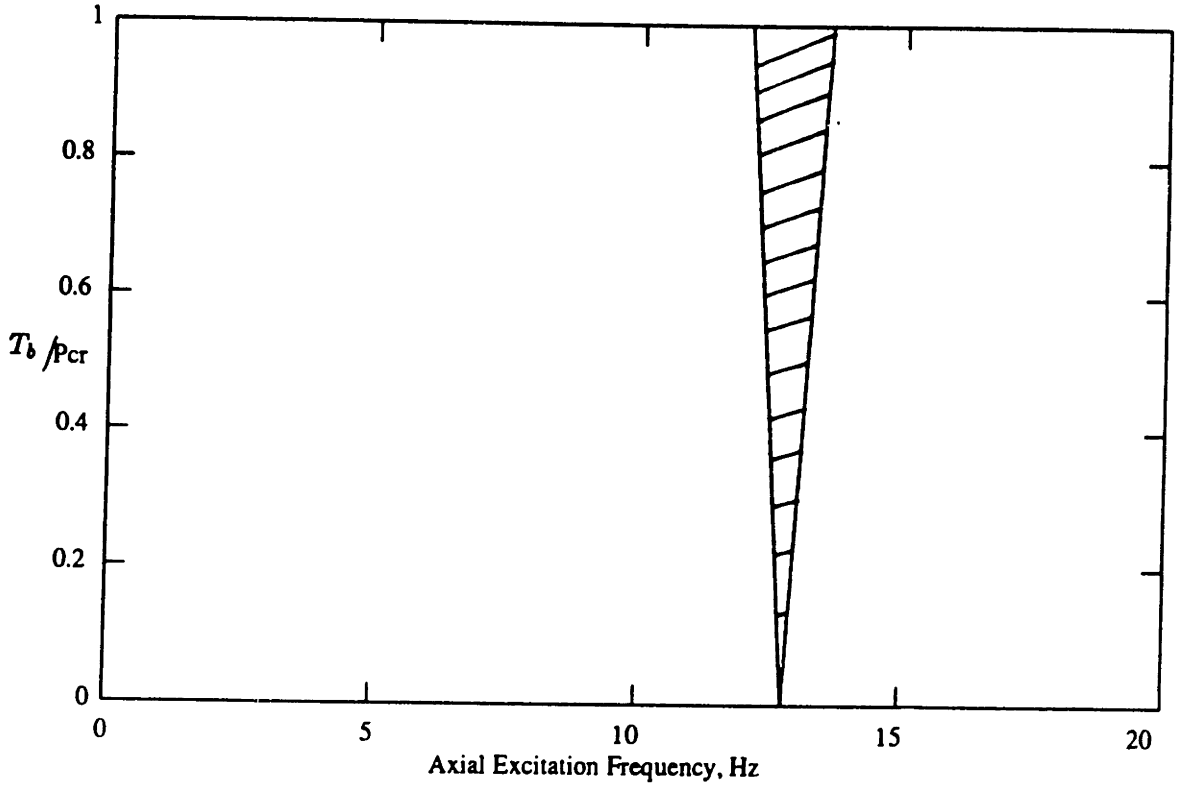

Figure 4.5: Region of Parametric Instability

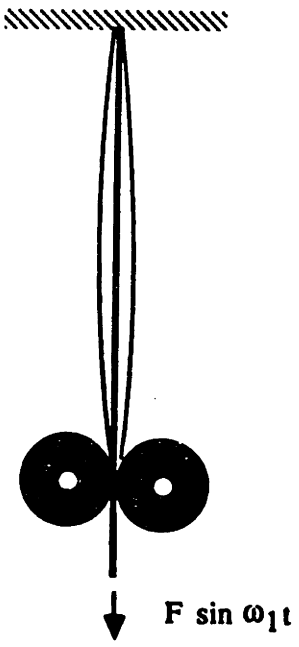

Figure 4.6: String under Axial dynamic Tension

$$\omega_1 = \frac{\pi}{L}\sqrt{\frac{T_0}{\mu}} \tag{4.20}$$

The undamped response of the string to an initial deflection in its first mode is simply

$$y(x,t) = A\sin(\omega_1 t)\sin(\frac{\pi x}{L}) \tag{4.21}$$

If one were to measure the dynamic fluctuations in tension, which are caused by the vibration at ω_1 , the tension would be observed to vary at 2 times the vibration frequency. The tension could be expressed as

$$T(t) = T_0 + T_1\sin(2\omega_1 t) \tag{4.22}$$

The tension has a dynamic component at twice the vibration frequency. If the process was reversed and a tension with dynamic component of $2\omega_1$ were applied at the end, then the string will respond at its natural frequency, ω_1. This is a simple analogy to the mechanism of parametric excitation of the bending vibration of the drill collars. Expressed in drilling terminology, a dynamic component of the weight on bit is capable of exciting bending resonances of the drill string at natural frequencies which are at one half of the excitation frequency. A mud motor rotating a bit could parametrically excite a non-rotating BHA.

4.7 Equation of Motion in a Rotating Coordinate System

Equation 4.7 describes a non-rotating BHA. The equation for a rotating beam expressed in a rotating coordinate system is as follows:

$$A\rho C_M\frac{\partial^2 r'}{\partial t^2} + (C_E + C_I + i2\omega)\frac{\partial r'}{\partial t} + EI\frac{\partial^4 r'}{\partial z^4} + iQ\frac{\partial^3 r'}{\partial z^3}$$
$$+A\rho gh\cos\phi[(l'-z)\frac{\partial^2 r'}{\partial z^2} - \frac{\partial r'}{\partial z}] - \omega^2 r' = 0 \tag{4.23}$$

where the prime in the expression r' denotes that the equation has not been put in dimensionless form. The effect of the rotation is shown in the Figure 4.7. This

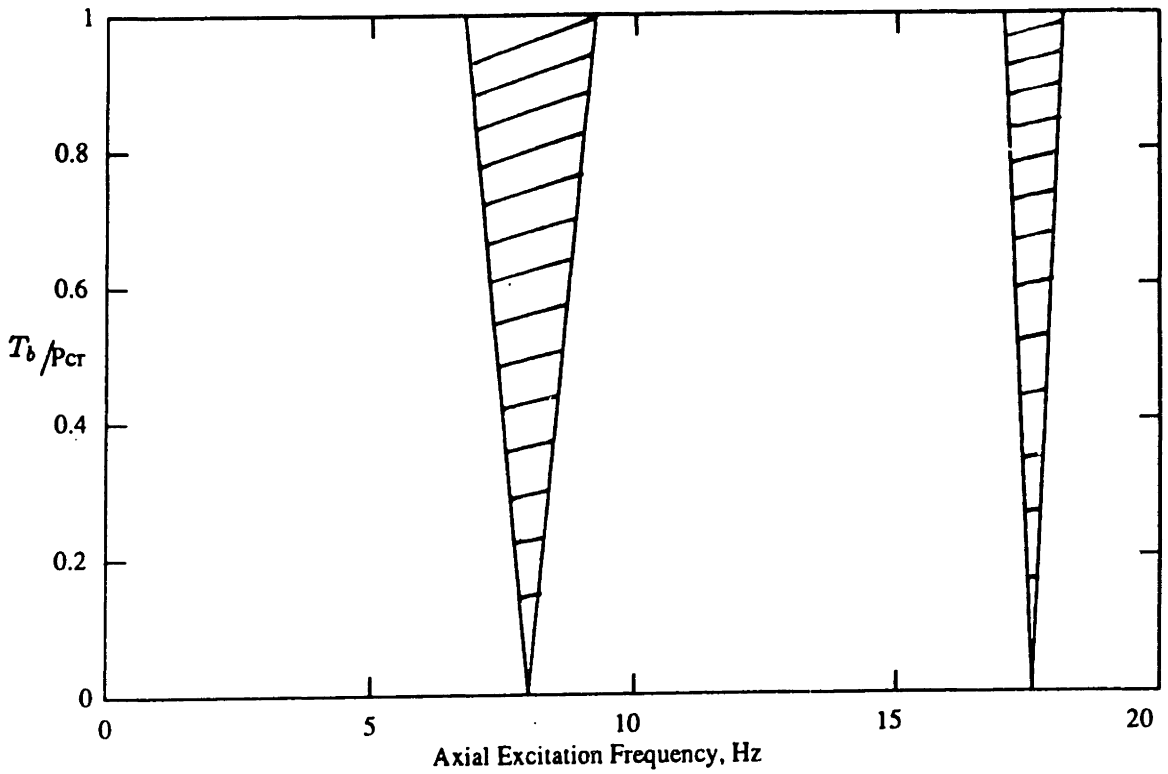

Figure 4.7: Region of Parametric Instability With Rotation Rate 2.4 Hz

example is plotted using the same data as in the earlier non-rotating case but now with a rotating speed ω of 2.4 Hz. It shows that the unstable region splits into two regions The unstable response associated the higher frequency region was demonstrated using a scale model as described in chapter 6.

4.8 Parametric Excitation of Bending Vibration a With Borehole Constraint

Equation 4.7 describes the drill collar motion without the constraint of the bore hole. This occurs possibly when the bore hole is nearly vertical. If the hole is slanted, and stabilizers do not hold the collars in the center of the hole, they may lay against the wall because of gravity. The section of the drill collars above the uppermost stabilizer are most likely to exhibit such behavior. Figure 4.8 shows the coordinate system used in the equation that describes the wall constraint. A detailed derivation

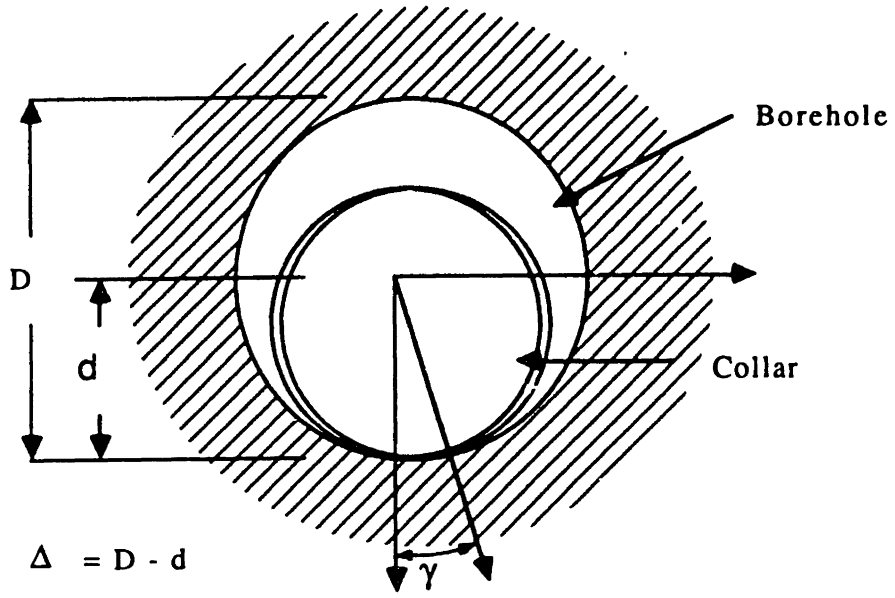

Figure 4.8: Coordinate System

of the equation with wall constraint is presented in Appendix B. The equation of motion with borehole constraint for the non-rotating case is:

$$A\rho C_M \frac{\partial^2 \gamma}{\partial t^2} + (C_E + C_I)\frac{\partial \gamma}{\partial t} + EI\frac{\partial^4 \gamma}{\partial z^4} + Q\frac{\partial^3 \gamma}{\partial z^3}$$
$$+A\rho gh\cos\phi[(l' - z)\frac{\partial^2 \gamma}{\partial z^2} - \frac{\partial \gamma}{\partial z}] + A\rho gh\frac{\sin\phi}{\Delta}\gamma = 0 \qquad (4.24)$$

where Δ is the borehole diameter minus the collar diameter, and γ is an angle measured with respect to the center of the hole between the static equilibrium point of contact and the instantaneous point of contact between the drill collar and the wall. γ is both a function of axial position z and time. The definitions of the other symbols are the same as those in equation 4.7. Following the same nondimensionalization and finite difference procedures, one can obtain the the matrix form of the equation

$$\frac{d^2}{d\tau^2}[\gamma] + \frac{C_E + C_I}{A\rho C_M \omega_0}\frac{d}{d\tau}[\gamma] + [A][\gamma] + \frac{QL}{EI}[B][\gamma]$$
$$+\frac{\rho gh\cos\phi}{C_M\omega_0^2}[(l - w)[C][\gamma] - [D][\gamma]] + \frac{gh\sin\phi}{C_M\omega_0^2\Delta}[\gamma] = 0 \qquad (4.25)$$

where [A], [B], [C], [D] are defined in equation 4.7. If similar terms are grouped, then

$$\frac{d^2}{d\tau^2}[\gamma] + \frac{C_E + C_I}{A\rho C_M \omega_0}\frac{d}{d\tau}[\gamma] + ([P_s] + [P_d])[\gamma] = 0 \tag{4.26}$$

where

$$[P_d] = \frac{\rho g h \cos\phi}{C_M \omega_0^2} T_d [C][\gamma] \tag{4.27}$$

$$[P_s] = [A] + \frac{QL}{EI}[B] + \frac{\rho g h \cos\phi}{C_M \omega_0^2}[(T_s - w)[C] - [D]] + \frac{gh\sin\phi}{C_M \omega_0^2 \Delta} \tag{4.28}$$

If the same normalizing procedure is taken, then equation 4.28 can be reduced to

$$\frac{d^2}{d\tau^2}[\gamma] + ([F] + T_b[S])[\gamma] = 0 \tag{4.29}$$

The instability condition for this system is the same as the case of no wall constraint, which is

$$\omega_i + \omega_j - T_b\eta < \omega < \omega_i + \omega_j + T_b\eta \tag{4.30}$$

However, the natural frequencies ω_i and ω_j are not necessarily the same as the case without wall contact. Without wall contact, the mode shapes look sinusoidal about the undeflected position of the straight beam. The mode shape lies entirely in a plane. With wall contact, the mode shapes when projected on the wall still look sinusoidal. But, as the beam deflects laterally, it must follow the curvature of the wall. In an inclined hole this is resisted by gravity. In the same way as a frictionless mass will oscillate in a circular shaped well due to gravity, the collar will also oscillate due only to the restoring gravitational force. Compared to the bending stiffness of the collar, this restoring force is negligibly small, except in the case of very low modes which may have little restoring force due to beam stiffness. This is especially true for the modes whose natural frequencies are reduced due to large compressive loads in the BHA. In other words, the presence of the wall may increase the natural frequency of the modes that are likely to be sensitive to buckling effects in the BHA. The unstable regions are indicated in Equation 4.30 The length of the drill collars above the uppermost stabilizer can be several hundred feet. Therefore, the modal density

(the number of modes per unit increase in frequency) of the bending vibration may get quite high, resulting in overlapping regions of instability. So, [19] introduces a term called severity, which is the same as η in the above equation, and was defined previously by for the case without wall contact, and is given again here.

$$\eta = severity = (\frac{S_{ij}S_{ji}}{4\omega_i\omega_j})^{\frac{1}{2}} \tag{4.31}$$

where S_{ij} is the ij-element of matrix [S]. But, with high modal density, it is difficult to plot the unstable regions, which may correspond to 20 or 30 modes that fall into the frequency range at which the collar would rotate. Instead of attempting to plot the regions of unstable response, we can plot the parameter η versus the frequency, $\omega_i+\omega_j$. This parameter gives the relative sizes of the unstable regions. So, η can be thought of as an indication of the likelihood of operating in the unstable region. The larger the opening of the unstable region, the more likely the drill string will encounter it. Therefore, the peaks in the severity versus frequency plot give information on the excitations frequencies that are likely to drive the collars above the uppermost stabilizer into unstable responses. One example of this calculation is shown in Figure 4.10. The inputs for this calculation are given in Figure 4.9 for a BHA with no stabilizers. The confirmation of this prediction with field or lab model has not yet been obtained and published. But once confirmed, one engineering application of this result is to avoid these peaks in the actual drilling conditions. For example, if a tricone bit is used for the drilling, strong axial excitation occurs at 3 and 6 times the rotation rate. These axial excitation frequencies should not be the same as the frequencies of high severity peaks, in order to avoid potential high bending responses.

Equation 4.30 shows that the width of an instability region is proportional to both the severity and the dynamic fluctuations in the weight on bit, T_b. One interpretation is that the severity is a measure of the instability risk per unit of excitation force, T_b. The severity calculation includes the longitudinal dynamic properties of the entire drill string. The severity is likely to be worse at frequencies which correspond to

longitudinal resonances.

All of the foregoing discussion was based on the assumption that the drill collar was not rotating and that the bit forces were the result of operation with a mud motor. Rotation introduces many potential complications which are not addressed in this thesis. However, the argument has been made but not proven, that the wall contact constraint nullifies the effects of the rotation on the natural frequencies, ω_i and ω_j, which are to be included in the severity calculation. Therefore, the results are the same as in the non-rotating case.

However, the examination of the Shell-NL downhole data taken in experiments described in [52] shows that the dynamic response in bending close to the bit is usually a very complex superposition of many simultaneous phenomena. The prediction of the instabilities under such circumstances may be much more difficult than describe here. In chapter 7, there is one example with evidence of parametrically excited bending vibration, thus, verifying the existence of the phenomena for a BHA with stabilizers in a region without wall contact.

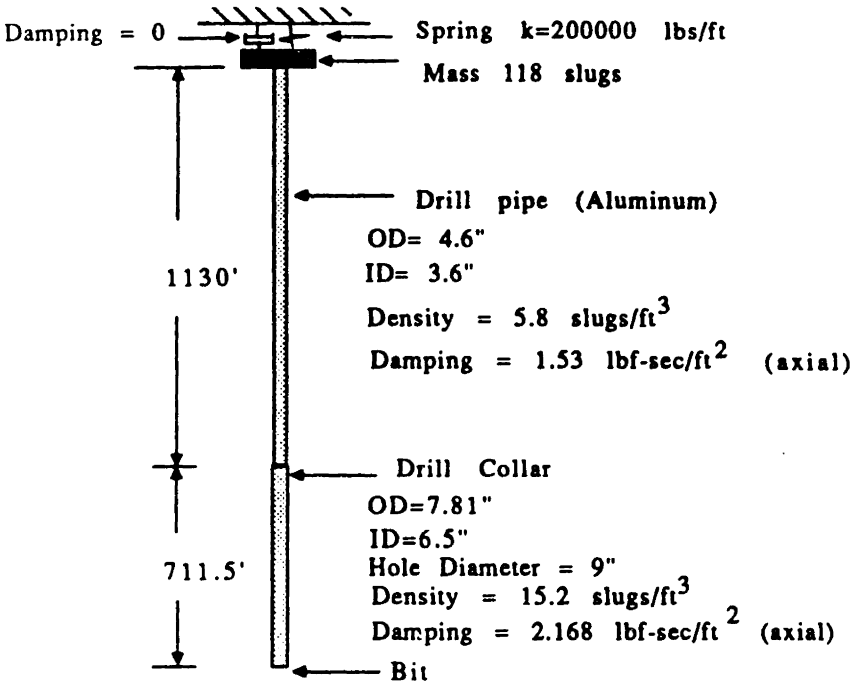

Figure 4.9: Inputs for the Severity Calculation

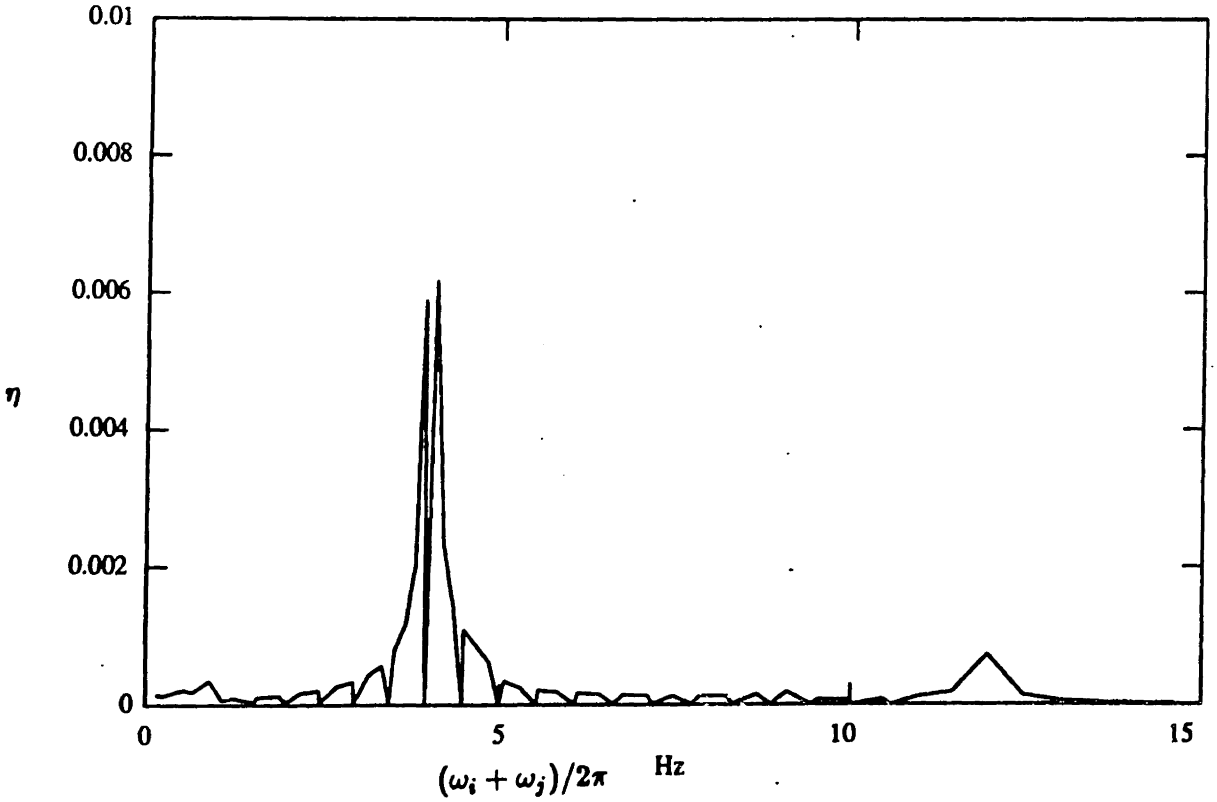

Figure 4.10: Severity versus Frequency Plot

Chapter 5

Rubbing of the Drill Collars

The drill string is designed to rotate, from 40 to about 100 RPM for conventional tri-cone and PDC bit drilling. As the drill collar rotates, whirling motion can be introduced. Whirling is simply the centrifugally induced bowing of the drill collar. Consider a drill collar in Figure 5.1 If the center of the gravity of the drill collar in not initially located precisely on the axis of rotation, then, as the collar rotates, a centrifugal force acts on the center of gravity, causing the collar to bend. The magnitude of the force is proportional to the mass of the collar, the square of the rotation rate, and the initial eccentricity of the mass center to the axis of rotation (usually the center of the hole). The initial eccentricity of the drill collar can result from several causes, including an initially bent drill collar, or sag due to an inclined borehole and gravity, or an eccentrically loaded weight on bit. This eccentricity can result in dynamic imbalance as the collar starts to rotate.

Whirling has been long known to occur in a destructive form in rotating machinery when the rotation rate of the shaft equals the natural frequency of that shaft in bending. When this happens, the machine is known to be operating at a critical speed. There is an enormous established literature on the subject of whirling of machines, such as turbine engines, axial flow compressors, and generators. An excellent tutorial on the subject may be found in reference [34], which presents a mathematical description of the simple whirling of a rotating shaft.

A great deal of effort and money is spent on balancing shafts and on developing

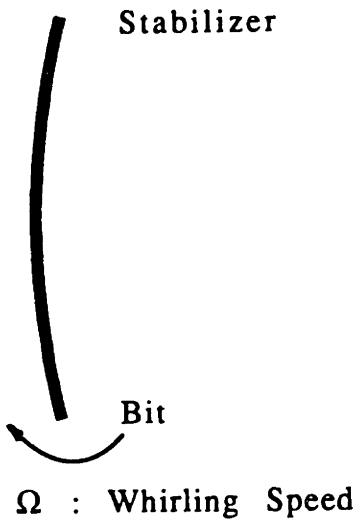

Figure 5.1: A Whirling Drill Collar

operating guidelines for machinery, so as to prevent serious whirling. This is generally not done with drill strings. One reason is that drill strings operate in the confinement of the borehole. Whirling does not generally result in precipitous failures of drill collars, because deflection amplitudes are limited by wall contact. There are, however, undesirable consequences of drill collar whirling behavior, not necessarily recognized in the drilling industry. One is abrasion of the surface of drill collars caused by rubbing on the wall.

The presence of the wall imposes displacement constraints on the bending and the whirling motion of the drill collar. Wall constraints not only limit the displacement of the collar, but also increase the stiffness of the collar if the collar comes in contact with the wall. There are several possible kind of rubbing behavior

- partial rub
- synchronous full annular rub
- backward full annular rub

Partial rub is characterized by the occasional contacts between the collar and the wall. If the collar maintains constant contact with the wall, the term "full annular rub" is used. It can be either in a forward or a backward direction with respect to the direction of the collar rotation. From an engineering point of view, synchronous rub, in which the same side of the collar is in constant contact with the side of the borehole, is the probable cause when a collar comes out of the hole worn flat in one place. In pure backward rub, the drill collar rolls without slipping on the inside of the hole in a direction opposite to the surface rotation rate (hence the name "backward whirl"). Your eye, if it could follow backward whirl, would see the center of the drill collar moving around the hole at a frequency much higher than the rotation rate of the drill collar itself. This phenomenon does not cause substantial surface abrasion, because there is little, if any, relative velocity between the drill collar and the wall. High frequency stress cycles, caused by bending of the drill collar, occur at many times the rate of rotation and may possibly lead to connection fatigue failure. These phenomena are explained in more detail in the following sections.

5.1 Kinematics of Whirling

The relative tangential slip velocity V between the drill collar and the borehole wall is given in chapter 2, as reproduced here :

$$V = (R_b - R_c)\Omega + R_c\omega \tag{5.1}$$

The tangential slip velocity is a measure of the amount of abrasion experienced by the drill collar on the wall. This velocity may vary from zero under conditions of perfect backward whirl with no slip to a maximum of $R_b\Omega$ under conditions of forward synchronous whirl. For fixed drill collar rotation rate ω, the tangential slip velocity V is a linear function of whirl rate Ω. Figure 2.2 in chapter 2 shows this linear relationship, and also indicates values of Ω where forward and backward whirl occur.

Backward whirl occurs for values of Ω less than zero. Backward whirl without slip

occurs when V is zero. By requiring the tangential slip velocity to be zero, equation 5.1 may be used to solve for the whirl rate Ω_b, which is defined as the condition of backward whirl without slip:

$$\Omega_b = -\frac{\omega_c}{R_b - R_c} \tag{5.2}$$

Backward whirl with slip occurs for values of Ω algebraically greater than Ω_b but less than zero. No whirl occurs if $\Omega = 0$ (i.e., the drill collar rotates but does not whirl around the hole center). Forward whirl with slip occurs for values of Ω greater than zero. The special case of forward synchronous whirl occurs when the whirl rate is equal to the drill collar rotation rate, $\Omega = \omega$. Drill collar whirl is considered unlikely for $\Omega < \Omega_b$ and $\Omega > \omega$, since "negative" wall friction would most likely be necessary to drive the whirling motion.

The whirl ratio is defined as the ratio of the actual whirl speed to the backward whirl speed with no slip:

$$s = -\frac{\Omega}{\Omega_b} \tag{5.3}$$

Substitution in equation 5.1 leads to the following useful variation for the expression for tangential velocity :

$$V = (R_b - R_c)s\Omega_b + R_c\omega \tag{5.4}$$

5.2 Partial Rubs

Partial rubbing is characterized by the occasional impact between wall and the collars. The motion of the drill collars before the first impact is most likely synchronous whirl. The normal impact force will be small in comparison with WOB because of the the relatively small clearance between wall and the collars. After the impact, the collar responds with lateral and torsional motion. The direction of rebound depends on the whirling velocity of the drill collar at the instance of impact. It either follows the original whirling direction or reverses into backward whirl. Muszynska [37] investigated the problem of partial rotor to stator rub and concluded that partial rub will

excite bending vibration at a subharmonic of the rotational speed as observed from a fixed reference frame. Although this mechanism has not yet been identified in field tests, it is likely to occur frequently in BHAs.

5.3 Forward Synchronous Rub

The mechanism of synchronous rubbing of a horizontally mounted rotor has been explained by Stackley [45], and experimentally evaluated by Joglekar [27].

Synchronous forward rub is a likely cause for the drill collar worn on one side only, therefore, the driller should know the likely operating range for which this phenomena will occur. Recalling equation 3.3 and adding the centrifugal force produced by the eccentricity of the drill collar to the right hand side of the equation yields

$$\ddot{s}' + \frac{C_E + C_I}{A\rho C_M}\dot{s}' + \frac{EI}{A\rho C_M}\frac{\partial^4 s'}{\partial z^4} + i\frac{Q}{A\rho C_M}\frac{\partial^3 s'}{\partial z^3} + \frac{gh\cos\phi}{C_M}[(l-z)\frac{\partial^2 s'}{\partial z^2} - \frac{\partial s'}{\partial z}] = \omega^2 e'(z)e^{i\omega t} \tag{5.5}$$

where $e'(z)$ is the eccentricity of the drill collar between the bit and the first stabilizer, and is a function of z measured along the neutral axis of the drill collar.

This equation can be solved by the finite difference procedures similar to those mentioned in chapter 3. But, instead of solving the eigenvalue and eigenvector problem, a system of simultaneous equations is solved with respect to a single rotating frequency. It is similar to equation 3.5,

$$[D][s] = [F] \tag{5.6}$$

except that right hand side is equal to [F], instead of a zero vector. The single column vector [F] is

$$[F] = \frac{\omega^2}{\omega_0^2}\begin{bmatrix} e(1) \\ e(2) \\ \vdots \\ e(N-1) \end{bmatrix} \tag{5.7}$$

where $e(1)$ to $e(N-1)$ are dimensionless eccentricities normalized with respect to the length of the drill collar between the bit and the first stabilizer.

Figure 5.2 shows the displacement of the collar at one quarter and one half the length. The inputs for this example are shown in Table 5.1.

Table 5.1: Inputs for the Example

100	L , Ft, Total length of the collar between the bit and the first stabilizer
0	Ci, Lbs/(Ft/sec)/Ft of pipe, Internal damping
7.5	OD, Inches
2.81	ID, Inches
10000.	Q , Lbs.Ft, Torque
3. 2. 200	Initial, increment, and ending value of rpm
10	Phi, Degrees, Slant angle of the borehole
12	RHOMUD, Lbs/Gallon, Density of the mud
0.8	Ce, Lbs/(Ft/sec)/Ft of pipe, External damping
30000	Lbs, Weight on Bit
19	N Segments (type 4M-1)
1.0	C (0=Pinned, 1=Clamped)
0.1 0.	e'1, Eccentricity of Lower Quarter of the drill collar
	Magnitude in inches, Phase in degrees
0.1 0.	e'2 Eccentricity of 2nd Quarter
0.1 0.	e'3 Eccentricity of 3rd Quarter
0.1 0.	e'4 Eccentricity of the Top Quart of the drill collar
1.	added mass coefficient of the mud
4.32E+09	Young's Modulus of the collar material

The displacements at quarter and half points on the collar are plotted assuming no wall contact. Normal operating speeds for a 100 foot pendulum BHA are from 40 RPM to 200 RPM. This range includes the natural frequencies for the first two bending

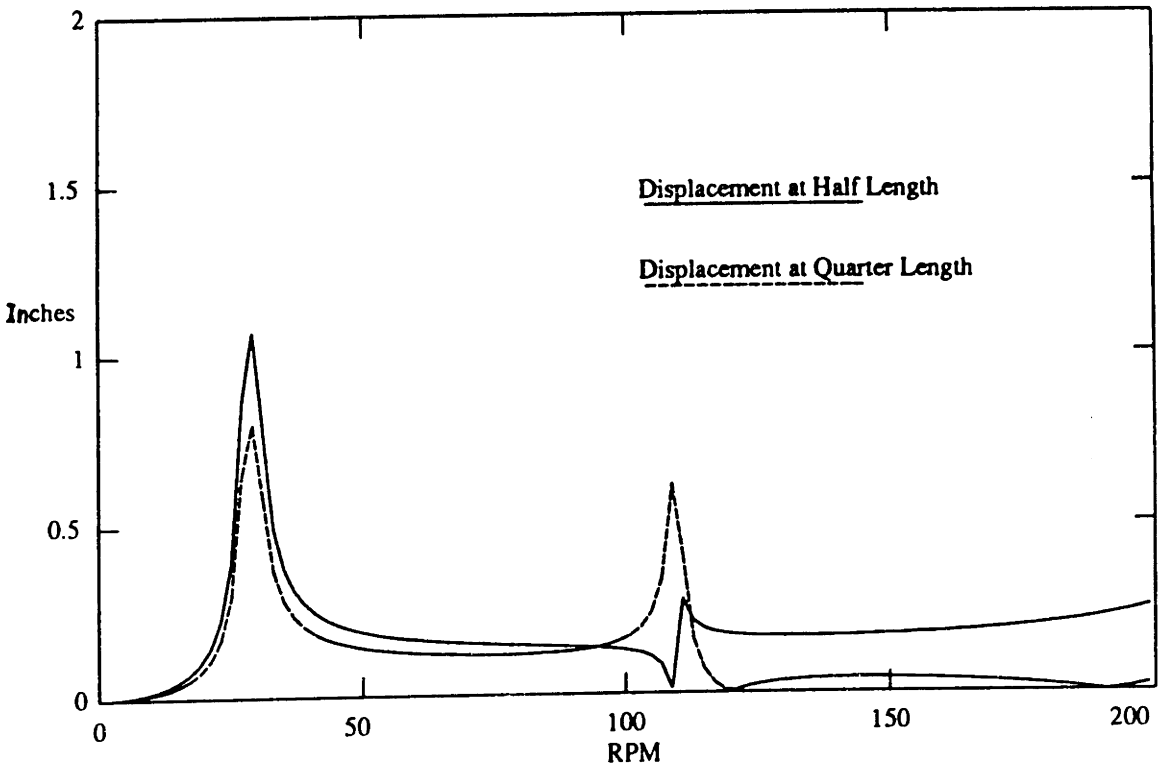

Figure 5.2: The Displacement at Quarter Length and Half Length above the Bit

modes. The first mode shape is a half sine wave, and the maximum displacement is at the half length point. The second mode shape is a full sine wave, and the maximum displacement is near the quarter length point. If the maximum displacement of the collar is less than the clearance, then, no rub is initiated, and the possible whirling motion of the drill collar is forward synchronous whirl. If the maximum displacement equals or exceeds the clearance, the rub is initiated. The clearance limit in Figure 5.2 would be indicated as a horizontal line, whenever the predicted amplitude crosses this limit, rub of some kind will result.

According to Stackley, the frequency range of the rubbing is likely to be wider than the frequency range in which the collar displacement exceeds the clearance, due to the modification of the collar stiffness as it touches the wall of the borehole. No attempt has been made in this thesis to predict the extension of the RPM range that the collar engages in forward synchronous rubbing. The analysis here gives only the

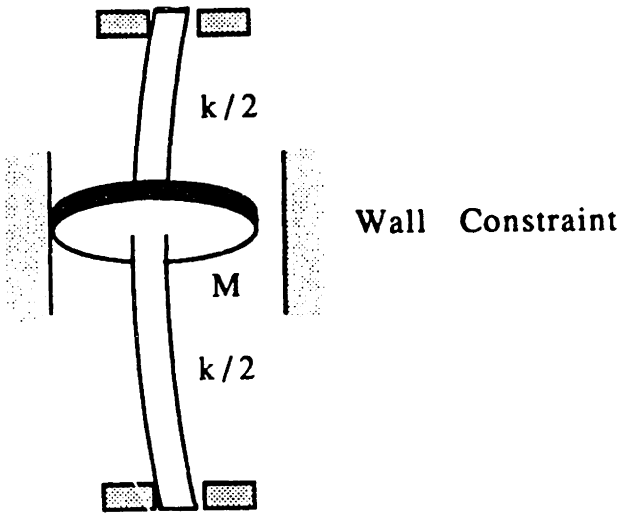

Figure 5.3: A Vertically Mounted Rotor Model

information on the frequencies at which collar rub would be initiated. More detailed analysis is recommended in future research.

5.4 Backward Whirl with Wall Contact

The following is a very simple attempt to model the onset of backward whirl. Much more work is yet to be done to refine and verify this initial attempt.

Backward whirl occurs if the direction of the motion of the center of gravity of the collar is opposite to the direction of rotation as described in chapter 2. Backward whirl with full annular rub is initiated if the friction force between the collar and the wall exceeds the structural and hydrodynamic damping forces, and drives the collar into backward whirl. During a full cycle of revolution, the collar keeps in close contact with the wall and may or may not slip. This phenomenon not only induces high amplitude bending stress cycles, but also may wear the collars if slippage occurs. Beginning with a simple model, a vertically mounted rotor, as shown in Figure 5.3, an explanation of the mechanism of backward rubbing is presented.

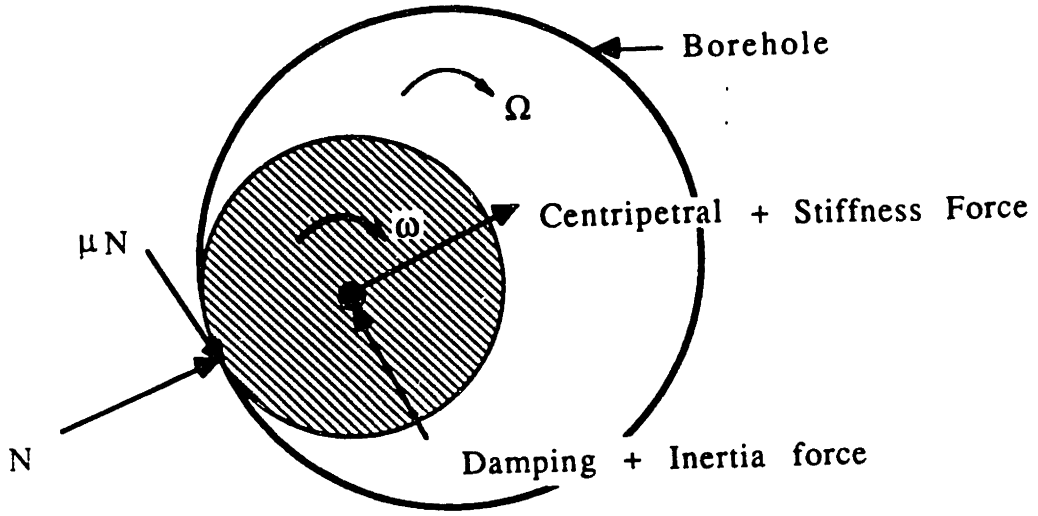

Figure 5.4: Force Diagram of Backward Rubbing

The model shown in Figure 5.3 has a disk of mass M, and a massless shaft with lateral stiffness K. This model is enclosed by an infinite rigid casing with fluid in it. Figure 5.4 shows the forces involved in the backward whirl. The equation of motion describing this mechanism in the tangential direction is

$$Mr_c\dot{\Omega} = -Dr_c\Omega - \mu N \tag{5.8}$$

and the force equilibrium in the radial direction is

$$R + Mr_c(\Omega^2 - \omega_n^2) = N \tag{5.9}$$

where

M : mass of the rotor

r_c : radial clearance

Ω : whirling speed of the rotor

D : damping forces

μ : friction coefficient between wall and the collar

N : normal force acting on the wall by the collar

R : portion of the normal force acting on the wall due to the coupling between the axial force and the curvature of the BHA

ω_n the first natural frequency of the system

If we assume that the damping is caused mainly by hydrodynamic mechanisms, D can be expressed as

$$D = \frac{1}{2}\rho_m C_D (2r) r_c^2 \Omega^2 \tag{5.10}$$

where ρ_m is the density of the surrounding fluid, and C_D is the hydrodynamic drag coefficient, and r is the radius of the disk. Note that the hydrodynamic drag coefficient ranges from 0.2 to 2.0 for cylinders in an unbounded fluid. The correct values for these condition is not known. Substituting the expression for N into the radial direction, we have

$$\dot{\Omega} = -p^2\Omega^2 + q^2 \tag{5.11}$$

where

$$p^2 = \frac{\mu M r_c + \rho_m C_D r r_c^2}{M r_c} \tag{5.12}$$

$$q^2 = \frac{-\mu R + \mu M r_c \omega_n^2}{M r_c} \tag{5.13}$$

If equation 5.3 is substituted into equation 5.11, and taking the whirl ratio, $\frac{\Omega}{\Omega_b}$, as the dependent variable, then

$$\dot{s} = \frac{1}{\Omega_b}(-p^2\Omega^2 + q^2) \tag{5.14}$$

This equation can be numerically integrated in the time domain to show the behavior of this equation. Following is an example with a hole diameter of 8.75 inches, a collar diameter of 7 inches, and a ratio of rotation rate to natural frequency of 1.0. The damping ratio and friction coefficient are assumed to be 0.05 and 0.3, respectively.

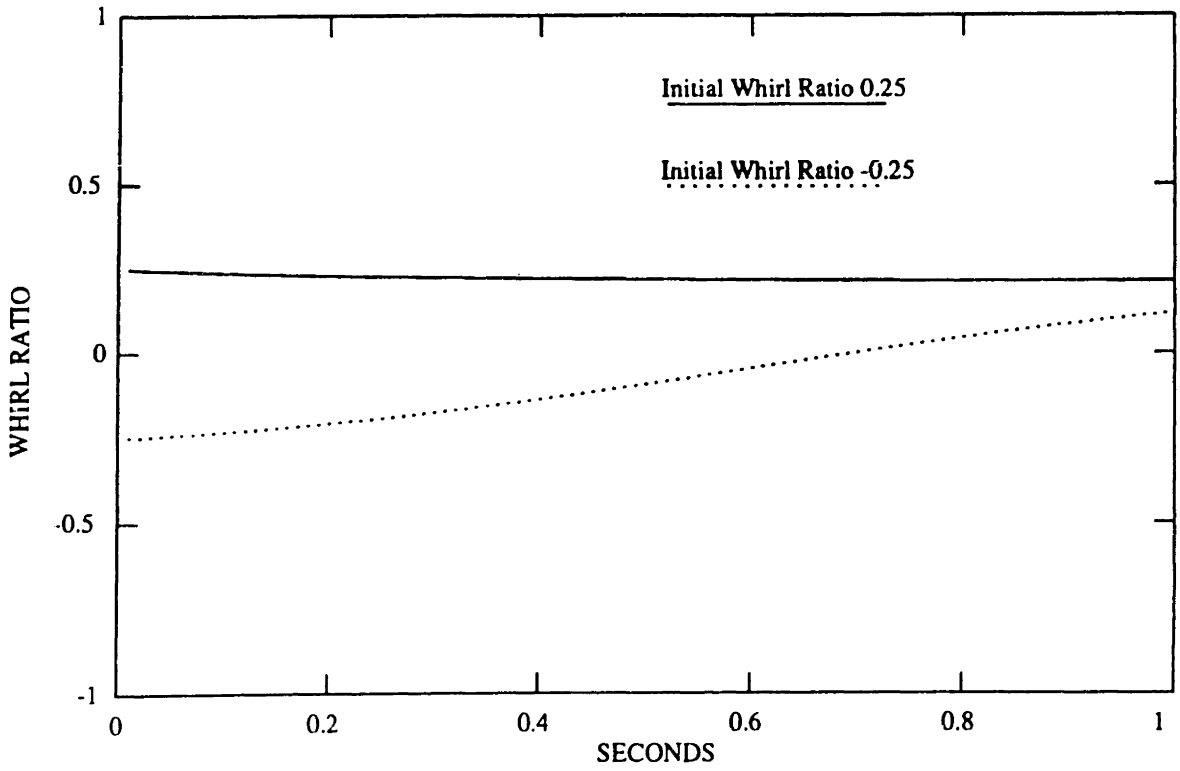

Figure 5.5: Time Domain Integration, With Initial Whirl Ratio -0.25, and 0.25

Under forward whirl conditions, the whirl rate and rotation are the same, which in this case would yield a whirl ratio of 0.25. Under perfect backward whirl conditions with no slip, the slip ratio as defined in equation 5.3 would be -1.0. Figure 5.5 shows the result of time domain integration which converged to a condition of synchronous whirl. In this case, R, the wall reaction due to static WOB, is assumed to be zero, and the initial condition of s_0= -0.25 was selected. Similar integration with initial s_0= 0.25 is shown in Figure 5.5, which shows the same convergence to forward synchronous whirl. Figure 5.6 shows a case of introducing R=20 pounds, which is assumed to be induced by the WOB, in the integration scheme. In this case, the result does not converge when starting from a initial condition of 0.25, but decreases to minus values, which indicates backward rubbing, then diverges. The divergence indicates the inadequacies of the mathematical model, which needs to be refined in further research.

Zhang [53] performed a similar analysis on the full annular rub of a horizontally

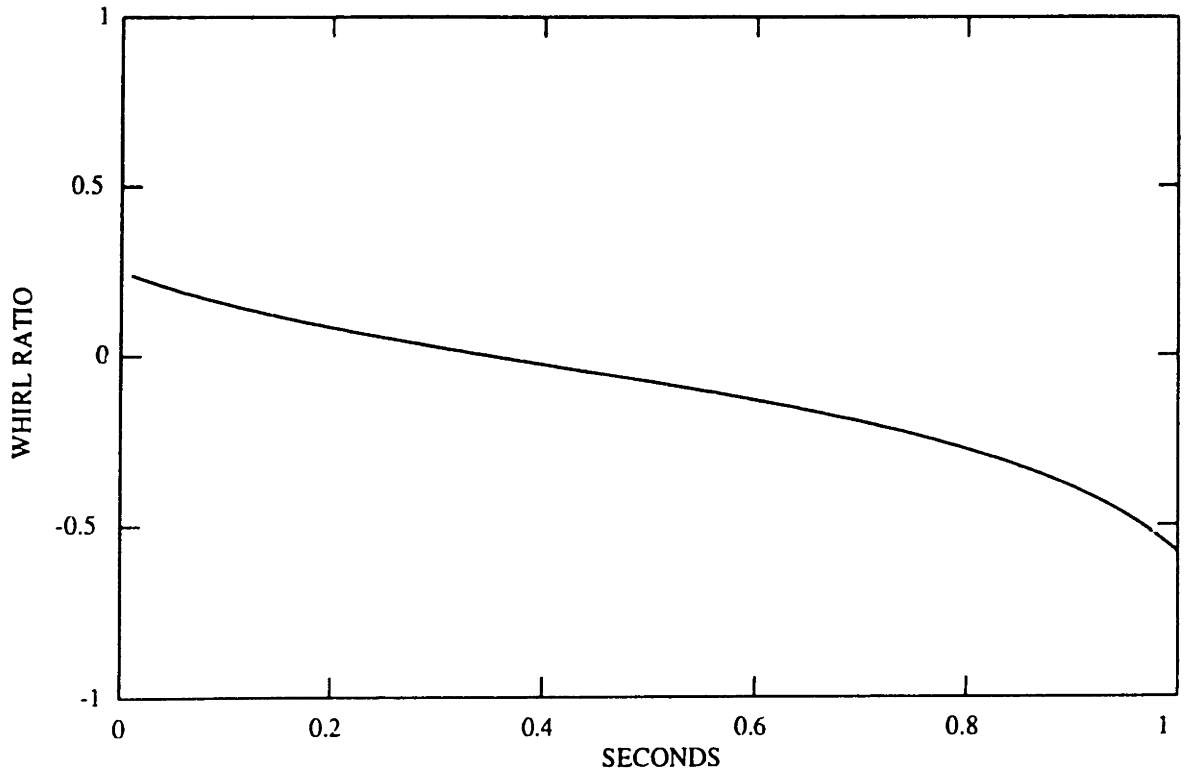

Figure 5.6: Time Domain Integration, With Initial Whirl Ratio 0.25, and Additional Wall Reaction

mounted flexible rotor system, and concluded that the conditions when the backward rub occurs are dependent on the initial contact velocity between the collar and the wall. Detailed experimental work is needed to verify this result.

The discussion presented above describes the collar motion by assuming the collar is in constant contact with the wall, and the equation of motion describing the forces in radial and tangential directions is derived under this assumption. This analysis gives only a preliminary mathematical model for the prediction of whirl conditions. Further refinements in prediction techniques and experimental work are left as future research topics.

Chapter 6

Laboratory Experiments

To demonstrate the validity of the theories detailed in previous chapters, experiments were carried out on a scale model in the laboratory. These experiments were conducted also with the purpose of better understanding the phenomena of whirling and coupling mechanisms. From these experiments, we also learned to recognize what these phenomena look like when observed in a rotating coordinate system, such as with a downhole tool.

6.1 Dimensional Analysis

Before proceeding with the scaled model experiments, a dimensional analysis was performed to estimate a suitable model.

In dimensional analysis, a group of parameters that reflect the dynamics of the system are selected to be modeled. For bending vibration of Bottom Hole Assemblies, the following 10 parameters were chosen and their relationship is stated by the following equation :

$$s = f(l, d, D, E, \rho, \rho_m, T, g, \phi, \Omega) \tag{6.1}$$

where

s : lateral displacement of the drill collar

l : characteristics length of the drill collar

d : drill collar outside diameter

D : diameter of the bore hole

E : Young's Modulus of the collar material

ρ, ρ_m : density of the collar and mud

T : weight on bit

g : gravity

ϕ : slant angle of the bore hole

Ω : rotation speed of the collar

If the independent parameters l, $\rho - \rho_m$, and E were selected, they can be arranged into 7 independent dimensionless groups. Let's denote length by L, mass by M, and time by S, then l, ρ, and E will have the following units:

l : L

ρ : $\frac{M}{L^3}$

E : $\frac{M}{S^2 L}$

Using Buckingham π method, a nondimensional relationship can be found for equation 6.1:

$$\frac{s}{l} = f^*(\theta_1, \theta_2, \theta_3, \theta_4, \theta_5) \tag{6.2}$$

where

$$\theta_1 = \frac{d}{l} \tag{6.3a}$$

$$\theta_2 = \frac{D}{l} \tag{6.3b}$$

$$\theta_3 = \frac{T}{l^2 E} \tag{6.3c}$$

$$\theta_4 = \frac{E}{gl(\rho - \rho_m)} \tag{6.3d}$$

$$\theta_5 = l\Omega\left(\frac{\rho - \rho_m}{E}\right)^{\frac{1}{2}} \tag{6.3e}$$

$$\theta_6 = \phi \tag{6.3f}$$

If the following notations are used

$$\lambda_1 = \frac{l_M}{l_P} \tag{6.4a}$$

$$\lambda_2 = \frac{(\rho - \rho_m)_M}{(\rho - \rho_m)_P} \tag{6.4b}$$

$$\lambda_3 = \frac{E_M}{E_P} \tag{6.4c}$$

where subscript M denotes the model , subscript P denotes prototype, then

$$\frac{d_M}{d_P} = \lambda_1 \tag{6.5a}$$

$$\frac{D_M}{D_P} = \lambda_1 \tag{6.5b}$$

$$\frac{T_M}{T_P} = \frac{(l^2E)_M}{(l^2E)_P} = \lambda_1^2\lambda_3 \tag{6.5c}$$

$$\frac{(\rho - \rho_m)_M}{(\rho - \rho_m)_P} = \frac{E_M l_P}{E_P l_M} = \frac{\lambda_3}{\lambda_1} \tag{6.5d}$$

$$\frac{\phi_M}{\phi_P} = 1 \tag{6.5e}$$

$$\frac{\Omega_M}{\Omega_P} = \frac{(l(\frac{\rho - \rho_m}{E})^{\frac{1}{2}})_P}{(l(\frac{\rho - \rho_m}{E})^{\frac{1}{2}})_M} = (\frac{\lambda_3}{\lambda_2\lambda_1^2})^{\frac{1}{2}} \tag{6.5f}$$

The same results can also be found by examining the nondimensionalized equation of motion for bending vibration.

The equations above show the relationships which should be satisfied in order to achieve dynamic similitude in bending vibration for both the prototype and the model. In reality, it is difficult to satisfy all of these equations, nonetheless, they are useful in selecting model properties that are compatible with the experimental equipment available. For example, the compression force needed to excite an instability must be within the output limit of the shaker.

6.2 Model Selection

From preliminary analysis, the plastic material, acrylic, was selected. The density of this material is about 2.48 slugs per cubic foot, and the Young's modulus is about 380,000 psi. The sample chosen for the experiment was a rod, 3.25 feet long and 0.25 inches in diameter. It was used to approximately model a 60 foot drill collar with mass density of 15.2 slugs per cubic foot, Young's modulus of 30,000,000 psi, and with drilling mud of 8.8 pounds per gallon. The value for λ_1 is 0.054, λ_2 is 0.188, and λ_3 is 0.0126. With these numbers, we can calculate the ratio of weight-on-bit, which is 0.0000367, between model and prototype. So, if we are simulating a dynamic WOB of 10,000 pounds, the dynamic force needed for the experiment is only about 0.3 pounds, which is within a output range of a relatively small shaker. The model to prototype ratio of rotational speeds is 4.8, as determined using the same values of λ_1, λ_2, and λ_3. If the operating speed of the actual drill string is 60 to 200 RPM; then, the corresponding speed in the model would be 288 to 960 RPM (4.8 to 16 RPS). This range of speed can be achieved by using a very simple variable speed electric motor. Note that because of the material chosen for the experiment and the limitations of the experimental equipment, the relation in equation 6.5 did not hold exactly for the this experiment. Nonetheless, we were able to make, for example, the rotational speed close to the modelling criteria. In the experiment, a rotational speed of 2.5 Hz was used. Also the shaker used in the experiment can put out a few pounds of force, and was capable of 0.3 pounds required by the modelling.

6.3 Setup of the Experiment

Figure 6.1 is the layout of the experiment. A supporting frame 5 feet long was used so that experiments could be performed at any angle of inclination. An electric motor was placed near the top of the supporting frame. This motor could be operated from 1.5 to 25 revolutions per second. A slip ring was attached to the motor's shaft, and

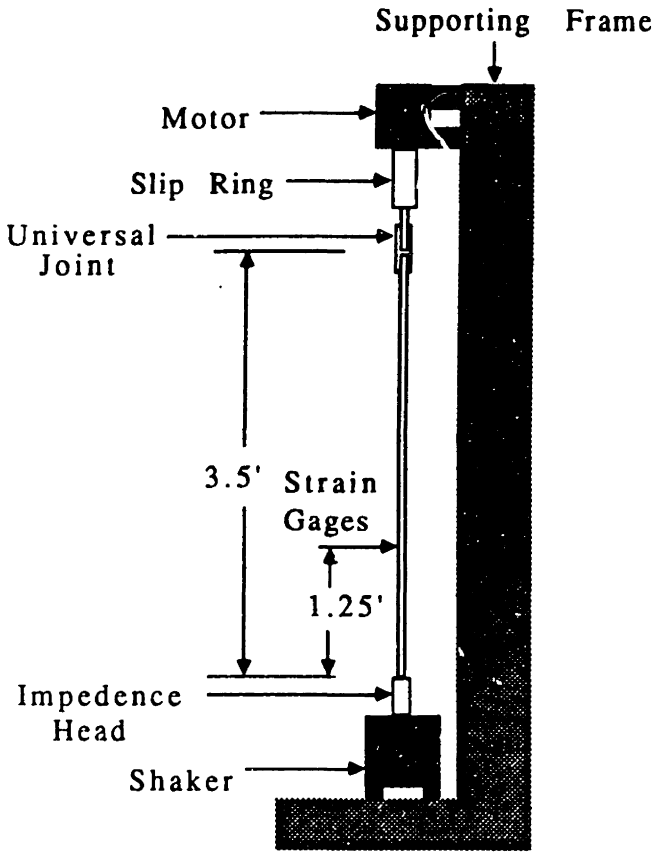

Figure 6.1: Layout of the Experiment

a universal joint was connected to the other end of the slip ring. Then, the universal joint was connected to the testing rod. The universal joint was used here to provide a pinned-like boundary condition for the bending vibration at the top of the testing rod. A pinned boundary condition was accomplished at the bottom and by running a metal point in a small hole. The purpose of the slip ring was to provide for the connection between the strain gages on the shaft and the strain gage amplifier. The slip ring created about 50 micro-ohms of noise; well below the problem level. A B&K mini-shaker simulating the forces of bit-rock interaction was placed at the bottom. It was driven by a power amplifier and a function generator. Two strain gages were installed 90 degrees apart to measure two axes of bending as shown in figure 6.2. The slip ring was used to carry the gage signals from the rotating shaft to a strain gage amplifier. A WR impedance head was placed between the shaft and the shaker to

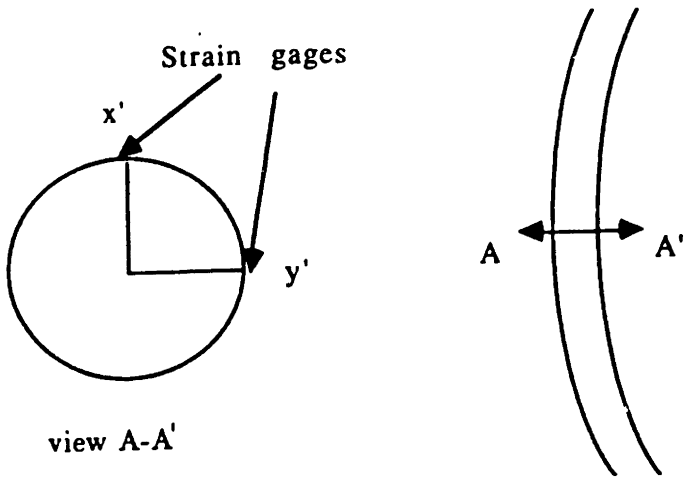

Figure 6.2: The Location of the Strain Gages

measure the axial forces. It was fixed to the top of the shaker, so it did not rotate during the experiment. A small pin of 0.5 inches long protruded from one end of the rod. The pin was inserted in a small hole on top of the impedance head. This provided rotational freedom for the shaft as well as a pinned-like condition for the bending vibration.

One strain gage was used to measured bending strain for each bending plane. A two gage bridge was not used to cancel out the unwanted axial strain in the bending strain measurements. The ratio of axial strain to bending strain caused by linear coupling can be shown to be given approximately by

$$\frac{\epsilon_a}{\epsilon_b} = \frac{d}{8\Delta} \tag{6.6}$$

where d is the diameter and Δ is the amount of displacement caused by the initial shaft curvature. For these experiments, the initial shaft displacement at the strain gage location was always greater than two diameters. Therefore, the dynamic axial strain was always less than 6% of the dynamic bending strain, and usually much less.

For parametric excitation, which happens with no initial curvature, the ratio of

dynamic axial strain to dynamic bending strain is given by

$$\frac{\epsilon_a}{\epsilon_b} = \frac{8PL^2}{\pi E d^3 A} \tag{6.7}$$

where

P = dynamic axial force

L = length

E = Young's Modulus

d = diameter

A = midspan bending deflection in the first mode

For a bending vibration amplitude of one diameter and an axial load of 0.3 pounds, this ratio for the experiment was less than 8%. At resonance, the response amplitude was much larger, and this ratio was proportionately smaller. The contamination of the bending strain measurements by the axial strain was not a significant factor in the conclusions of the tests.

6.4 Data Acquisition

An IBM AT compatible machine with a MetraByte Das-16 A/D Board was used to sample the signals. The A/D software used was capable of writing digitized data directly onto the hard disk. Each data point is written in two byte integer format. The maximum sampling rate of this system is around 5K Hz. Two stain gages signals and the signals from the impedance head, which are force and acceleration, were taken during the experiments. The sampling frequency was fixed at 200 Hz per channel throughout the experiments.

Figure 6.3 shows the connections between the transducers and the computer.

6.5 Experimental Procedures

The first natural frequency of the non-rotating shaft varied from 3.5 to 3.9 Hz depending on the amount of mean (constant) component of compressive axial force,

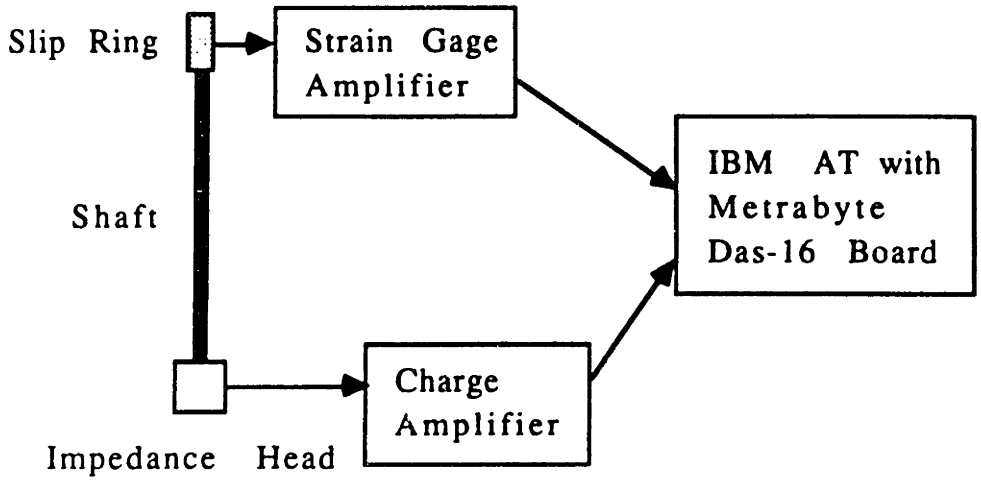

Figure 6.3: Signal Path of the Experiment

and upon the mean curvature. A constant axial force was required to support the weight of the shaft as well as to prevent any bouncing of the lower bearing point in the retaining hole. Increase in either axial force or curvature (such as due to whirling) reduced the natural frequency. Of course, the same is also true in a real drill collar. During the rotating experiments, the mean curvature changed in an uncontrollable way due to the combined effects of whirling and mean axial force, thus causing the equivalent non-rotating natural frequency to vary from 3.5 to 3.9 Hz. For the prediction calculations shown here, an average value of 3.7 Hz is used. Resonance frequencies under actual conditions varied by a small amount due to changes in mean curvature and mean axial force.

The experiments were carried out by holding the rotation speed constant at 2.5 Hz, and varying the shaker frequency from 1 to 15 Hz in increments of about 1 Hz. This sweep test allowed the estimation of the correlation between the input force and

the bending response.

6.6 Discussion of the Results

The specific purpose of the experiments was to observe and describe both linear coupling between axial force and bending vibration and parametrically excited bending vibration. Before conducting the experiments, we understood in a mathematical sense that vibration could result, but we would have been hard pressed to clearly describe it. The experiment had a significant self education component.

In chapter three, it was predicted that resonances at natural frequencies when experienced on a rotating beam would occur at frequencies which are different than that predicted for a non-rotating beam. The predicted natural frequencies as observed on the rotating beam are given by the following equation in (rad/sec)

$$\omega_n^- = \omega_n - \omega \tag{6.8a}$$

$$\omega_n^+ = \omega_n + \omega \tag{6.8b}$$

or expressed in Hz as

$$f_n^- = f_n - \frac{\omega}{2\pi} \tag{6.9a}$$

$$f_n^+ = f_n + \frac{\omega}{2\pi} \tag{6.9b}$$

where $\frac{\omega}{2\pi}$ is the rotation rate in Hz and $f_n = \frac{\omega_n}{2\pi}$ is a bending natural frequency for a non-rotating beam. These equations indicate that as the beam begins to rotate, the natural frequencies bifurcate in frequency. Resonant conditions no longer correspond to excitation at the non-rotating natural frequency f_n but occur when the excitation corresponds to either of the two bifurcated frequencies given above.

The bifurcated natural frequencies correspond to mode shapes which are seen as orbits in the rotating frame. In other words, the beam not only bends into the mode shape as expected in the non-rotating case but also makes elliptical orbits about

its mean radial position. At any section of the beam, the center of gravity of the section will appear to move in an elliptical or circular path. The direction of the orbit is different for the two bifurcated modes. The f_n^+ mode represents orbits in the direction of the rotation and the f_n^- mode represents motion opposite to the rotation direction when f_n^- is positive, and in the direction of rotation when it is negative. An objective of the experiment was to visualize these motions, as well as test out the predictions of linear coupling and parametric excitation.

As discussed earlier, the natural frequency of first bending mode was approximately 3.7 Hz. The rotation speed of the model was 2.5 Hz. So the bifurcated natural frequencies with respect to the rotating reference frame were expected at:

$$f_n^- = 3.7 - 2.5 = 1.2Hz$$

$$f_n^+ = 3.7 + 2.5 = 6.2Hz$$

Under synchronous whirl conditions at the natural frequency, the shaft bows out to a deflected position and stays there. Any point on the shaft stays at the same distance relative to the center of the hole, and in the moving reference frame, does not appear to move. In the fixed reference frame, a proximity probe would see large vibration at the shaft rotating speed. Depending on the reference frame of the observer, the vibration frequency takes on different values. The one most important to drilling is the one seen in the rotating reference frame because this is the frame in which measurements are made on. Figure 6.4 shows the force spectra as measured by the impedance head for the control case that the shaft was not rotating. Each spectrum in the stack was generated with the control signal to the shaker at different frequencies beginning at 3 Hertz, then, progressing up to 9 Hertz in steps of 1 Hertz. The shaker frequency is indicated on the right hand side of the plot. Each spectrum shown in the plot in the force spectrum was observed by the impedance head, when the control signal to the shaker was at a single frequency. For each spectrum the major peak, measured on the horizontal axis, should correspond to the frequency indicated on the

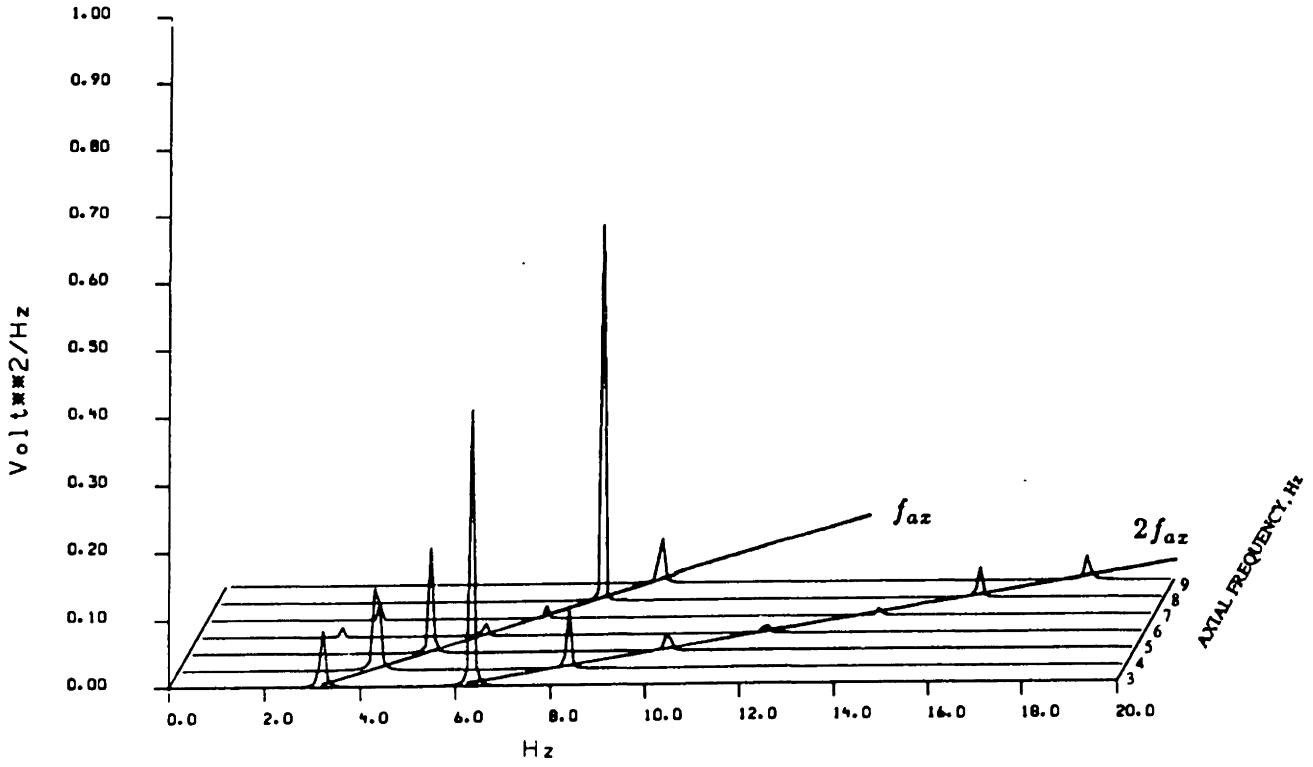

Figure 6.4: Force Spectra, Non-Rotating

right hand side. Since the spectra are stacked in ascending order, the major peaks fall on the line labelled f_{az}. There is also a second line of peaks labelled $2f_{az}$. These exist because the motion of the shaker is not perfectly sinusoidal, even though the input signal may be. The motion is periodic, and has higher Fourier components of the basic periodic signal, f_{az}. In this case, the second harmonic is reasonably strong and may also excite some bending response of the shaft.

Figure 6.5 is an example of the bending response from one of the strain gages, revealing the bending moment in one of two orthogonal measurement planes. Again each spectrum in this stack corresponds to the ascending frequencies in axial force, from 3 to 9 Hz. In the first spectrum with three Hertz excitation there is a small linear coupled response peak at 3.0 Hz. The response is small because the excitation and the natural frequency did not quite coincide. The largest response peak on the figure occurs at 3.5 Hz. with an excitation frequency of 7.0 Hz. This is an example

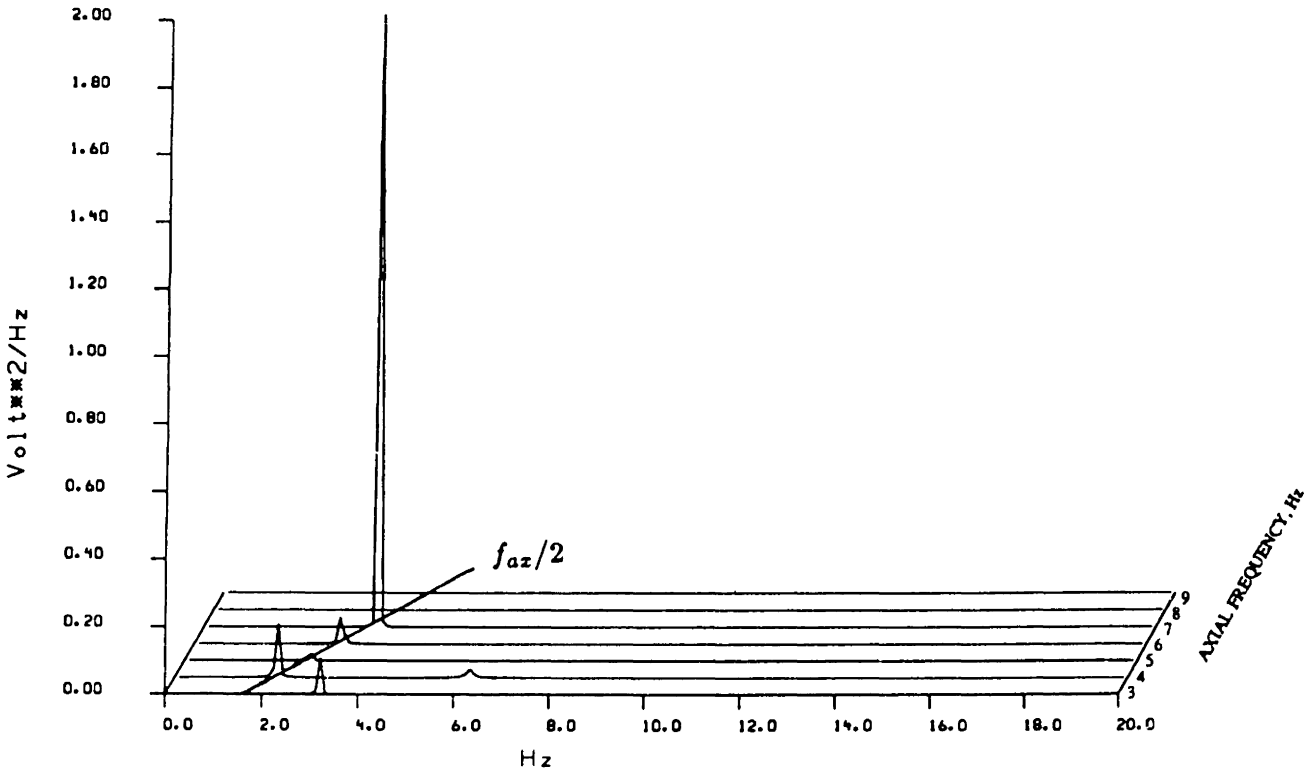

Figure 6.5: Bending y' Spectra, Non-Rotating, Parametric Resonance

of a parametric excitation of the first mode of the non-rotating shaft which has an approximate natural frequency of 3.7 Hz in response to an axial excitation at twice the response frequency. Recall that from Figure 4.5 the unstable region is a band of excitation frequencies centered on $2f_1$.

Moving on, a rotating example is shown in Figure 6.6. This figure is again a cascade sequence of the spectra of the force signal. But, in this case the motor was running and the rotation rate was at 2.5 Hertz. Each successive plot in this cascade was taken when the axial force signal was set at successively higher frequencies from 1 to 15 Hertz. There is a small straight line of peaks at 2.5 Hertz. This is at the rotation rate and is likely caused by irregularities in the thrust bearing or the universal joint, causing a once per revolution perturbation, which can be seen in the force signal. It is helpful because it shows that the beam was indeed rotating and reveals the rotation frequency. There are many other peaks in this spectral plot, but the most important

one is the line of peaks at the excitation frequency, labelled f_{az}. In the figure, second and third harmonics of exciting force are also evident.

Figure 6.7 is the response spectra that result from these input spectra. Several different phenomena occur, including linear and nonlinear coupling. The first natural frequency in a nonrotating reference frame is approximately 3.7 Hertz. The natural frequency may decrease a little once the shaft starts to rotate, due to the curvature induced by whirling. In a rotating frame of reference, one would expect to observe resonances occurring at the bifurcated natural frequencies, which are 6.2 Hz. and 1.2 Hz. These are then the approximate first natural frequencies of this beam in the rotating reference frame.

Beginning at the bottom of this stack plot, the axial excitation is at 1.2 Hertz, which is resonant with the lowest natural frequency. An amplified response due to linear coupling is seen at 1.2 Hz. As the axial excitation is increased to 2.1 Hertz in the second spectrum, the linearly coupled response decreases, because there is no close relationship between the axial excitation and any resonance. At 3, 4.2, and 5 Hertz the response drops even further for the same reason. Observed in the rotating frame the non-rotating resonance at 3.7 Hz. does not exist. As the excitation reaches 6 Hertz a very high response peak is evident. This is linearly coupled resonant response of the mode expected at 6.2 Hz, resulted from curvature of the shaft. In the experiment, the shaft had substantial initial curvature, which was caused in part by forward synchronous whirl and the mean axial force.

Moving on, the next highest response peak occurs on the spectrum for which the axial excitation was at 7.1 Hz. The excitation was at 7.1 Hertz, but the response is observed at two peaks, one at approximately 6.2 Hertz and a smaller one down at 0.9 Hz. It happens that the sum of the two natural frequencies in the rotating frame is close to 7.1 Hz. as shown below.

The excitation at 7.1 Hertz is close enough to cause a small combined response in both modes; the one nominally at 1.2 Hz. and the one at 6.2 Hertz. This is an

example of parametric excitation at a sum frequency of the natural frequencies as observed in the rotating reference frame.

Moving on to the next highest peak for which the axial excitation was at 12.6 Hz. The peak is at 6.3 Hz, and there is no visible peak at 12.6 Hz. This is an example of parametric excited bending vibration of a rotating shaft at twice f_n^+.

Another interesting way to evaluate the motion under these complicated whirling and coupled vibration conditions is to plot the outputs of the two strain gages simultaneously so one may visualize the bending x' versus bending y' time history.

Figures 6.8, 6.9 ,and 6.10 are for the case when the axial excitation was at 1.2 Hz. A time history of the x' and y' strain gages plotted against one another reveals essentially circular orbits. The plot you see in Figure 6.8 is for one second of data and shows that in one second the bending cycles went through approximately one orbit. The direction of the orbit is clockwise.

Figure 6.9 shows the individual time histories of $B_{x'}$ and $B_{y'}$, the outputs of the x' and y' strain gages. What is not known in this particular case is the actual orientation of x' and y' with respect to the tangential or radial directions as seen from a fixed reference frame. What is clear is that they are both at the same frequency, but with a 90 degree phase shift with respect to each other, thus resulting in the circular orbits. Figure 6.10 is a plot of the magnitude of the bending strain versus the phase angle of $\tan^{-1}\frac{Bx}{By}$.

The phase between Bx' and By' is useful in revealing the motion of the drill collar. It will be used frequently later on. The technique used in presenting phase angle is called phase unwrapping. Consider the function arctangent

$$\phi(t) = \tan^{-1}(g(t))$$

where $g(t)$ is any given time function. The principal values of the arctangent range from -180 to 180 degrees. Therefore, if $\phi(t)$ is plotted, discontinuities may occur. Phase unwrapping is a method to make $\phi(t)$ continuous. One way to achieve phase

unwrapping is the following, assuming that ϕ_{i+1} and ϕ_i are two adjacent points in time,

1. Determine the absolute value of ϕ_{i+1}-ϕ_i, if this value is greater than 180 degrees, then do the phase unwrapping, otherwise proceed to next point

2. Determine the sign of ϕ_{i+1}-ϕ_i, if phase unwrapping is needed

3. If the sign is plus, subtract 360 degrees from every point after ϕ_i; if the sign is minus, add 360 degrees to every point after ϕ_i

By performing the above procedure for every data point, one can obtain the unwrapped phase plot of the function, arctangent.

Figures 6.11, 6.12 ,and 6.13 are for the case when the axial excitation was at 6 Hertz, which coincided with a natural frequency and resulted in linear coupling. A time history of the x' and y' strain gages plotted in Figure 6.11 is for one second of data and shows that in one second the bending cycles went through six orbits. The trajectory of the orbit is in the counterclockwise direction.

Figure 6.12 shows the individual time histories of $B_{x'}$ and $B_{y'}$, the outputs of the x' and y' strain gages. Figure 6.13 is a plot of the magnitude of the bending strain versus the phase angle.

Figures 6.14, 6.15 and 6.16 are for the case that the excitation was at 7.1 Hertz. This was an example of parametric excitation at the sum of the resonances at 0.9 Hz. and 6.2 Hz. Figure 6.14 shows $B_{x'}$ versus $B_{y'}$ time history for 1.0 second of data. This time, a precession of loops occurs. The direction of precession is clockwise, with precession frequency of 0.9 Hz. On top of the precession motion is the 6.2 Hz component, with a counterclockwise direction. Figure 6.15 shows the independent time histories of $B_{x'}$ and $B_{y'}$. In both of these time histories, a slow 0.9 Hz. modulation of the 6.2 Hz vibration is evident. Figure 6.16 is a plot of the magnitude and phase for that case.

Figures 6.17, 6.18, and 6.19 are for the case when the axial exciting force was at 12.6 Hertz. The shaker was tuned to give a maximum in the parametric resonance at a driving frequency which was approximately at twice the natural frequency of 6.3 Hz. In this case, it was possible to determine that the x' oriented strain gage was in fact sensitive to bending in the radial direction and the y' one was sensitive to bending in the tangential direction. In this case of parametric resonance, it was determined that the principal vibration of the shaft was essentially along a tangent with respect to the whirling orbit of the shaft. $B_{x'}$ and $B_{y'}$ time histories are plotted in x' versus y' form in Figure 6.17. The tangential component is by far the larger. The independent time histories of $B_{x'}$ and $B_{y'}$ are shown in Figure 6.18, and the magnitude and phase are shown in Figure 6.19. The zero offset in the By' time series ia an instrumentation error and is not real.

The experiment verified the prediction of linearly and parametrically excited bending vibration of rotating and non-rotating shafts at natural frequencies which bifurcate and vary linearly with rotation speed. The two bifurcated modes exhibit orbital motions of opposite sign.

In closing the discussion on the results of the experiment, it must be emphasized that the parametric excited vibration is the least well understood as a potential source of failures in real bottom hole assemblies. The effect of the contact with the wall is not at all well understood. Realistic amounts of damping are not yet known. Whether or not significant levels of this form of vibration actually occur under realistic conditions has yet to be verified.

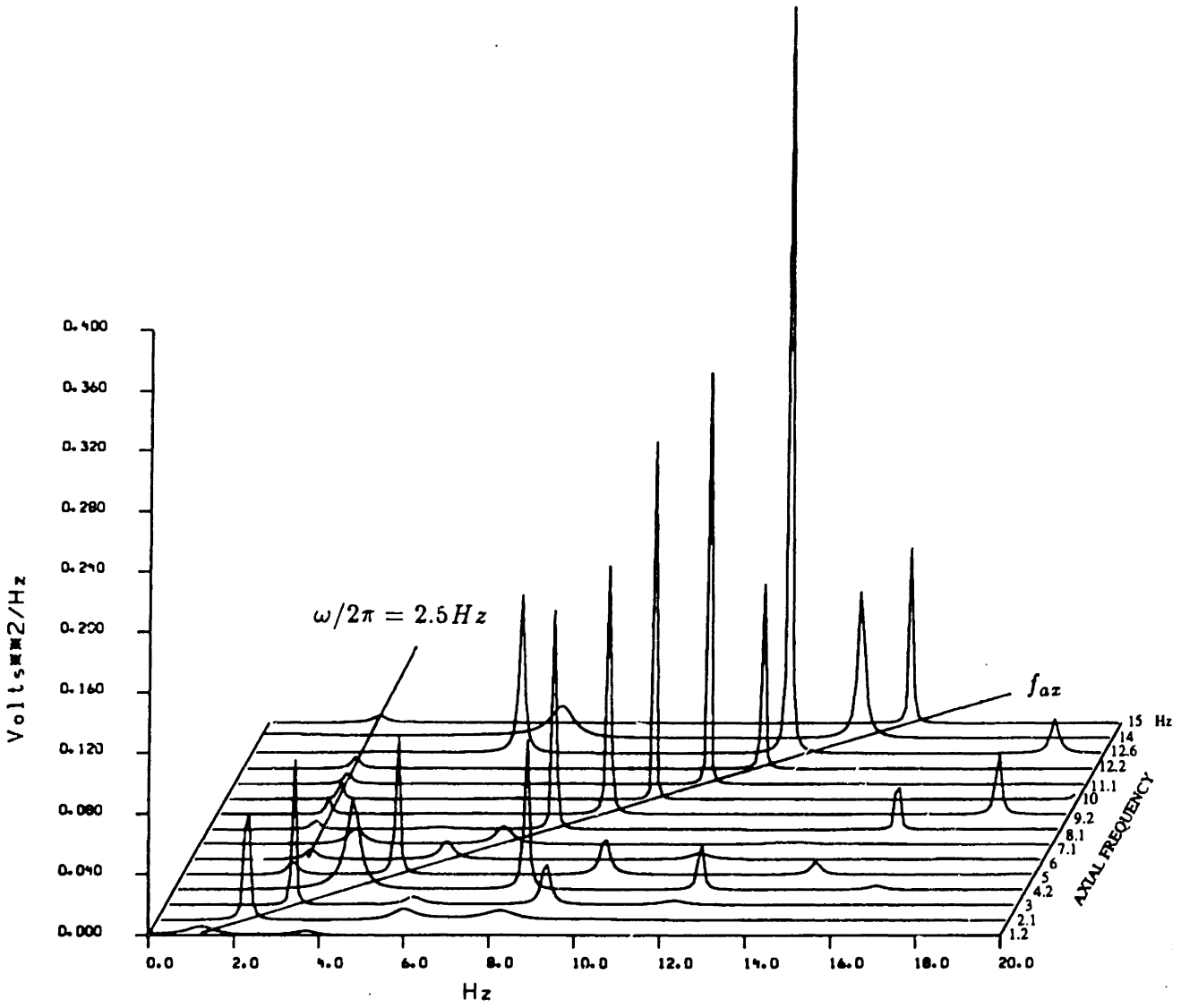

Figure 6.6: Cascade of Force Spectra, Rotating at 2.5 Hz

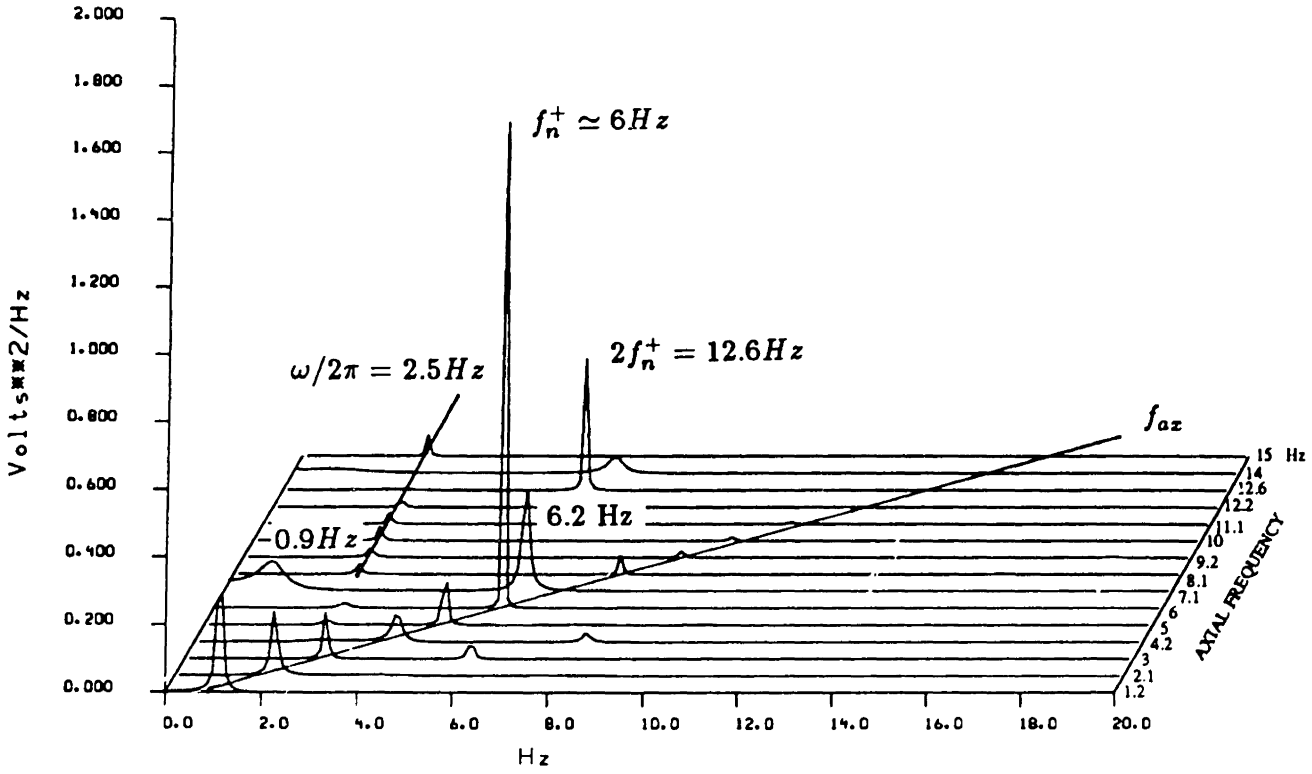

Figure 6.7: Cascade of x' Bending Spectra, Rotating Clockwise at 2.5 Hz.

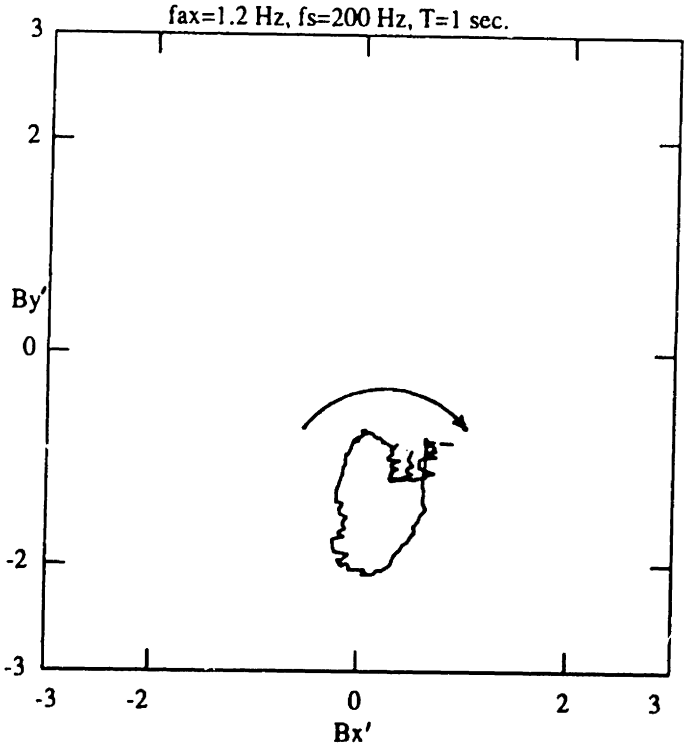

Figure 6.8: Bending x' versus Bending y', $f_{az} = 1.2$ Hz

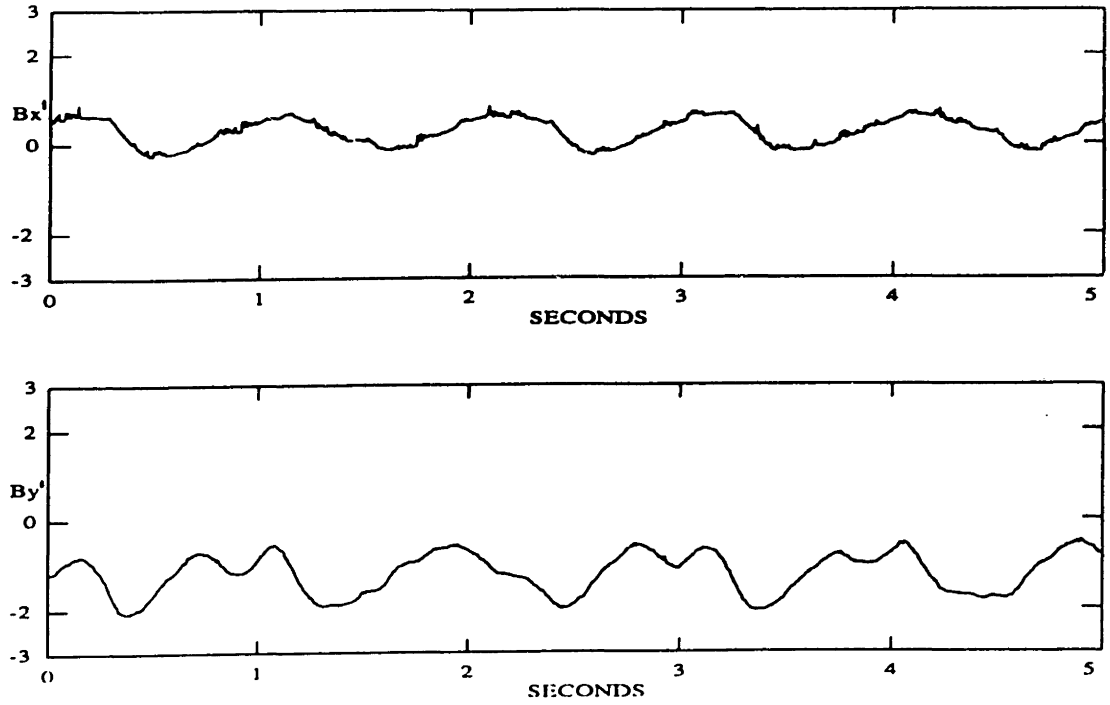

Figure 6.9: Bending x' and Bending y' Time History, $f_{az} = 1.2$ Hz

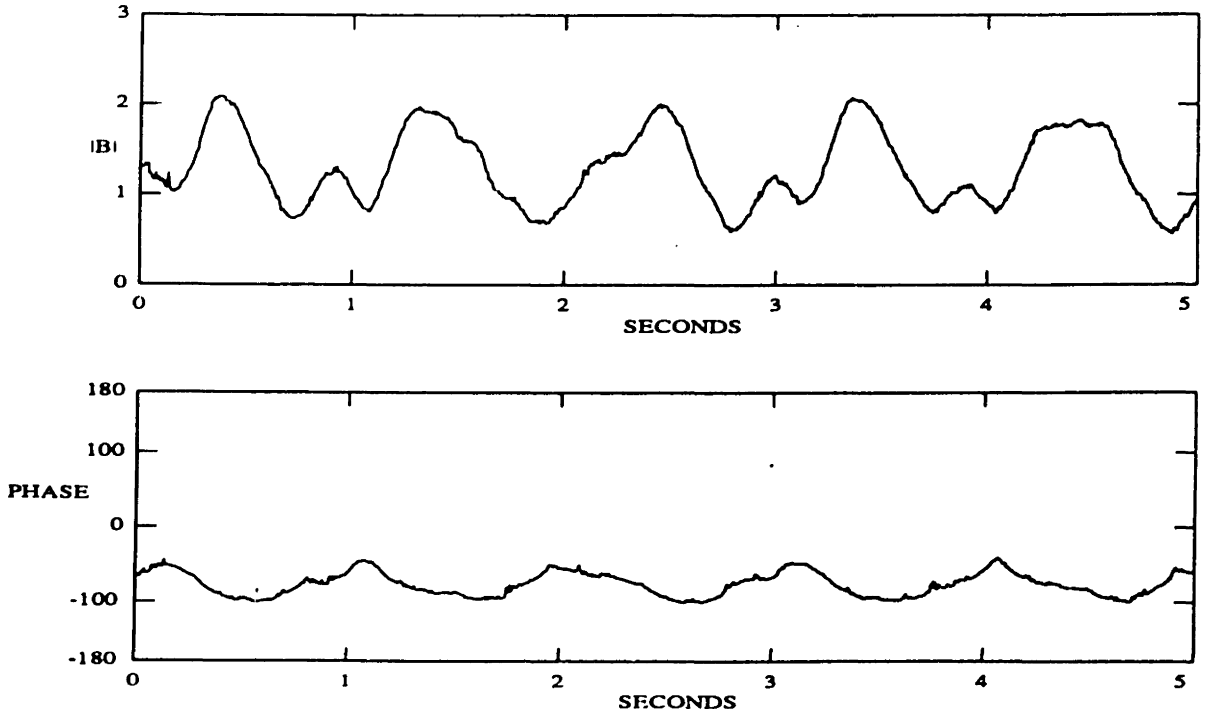

Figure 6.10: Bending Magnitude and Phase, $f_{az} = 1.2$ Hz

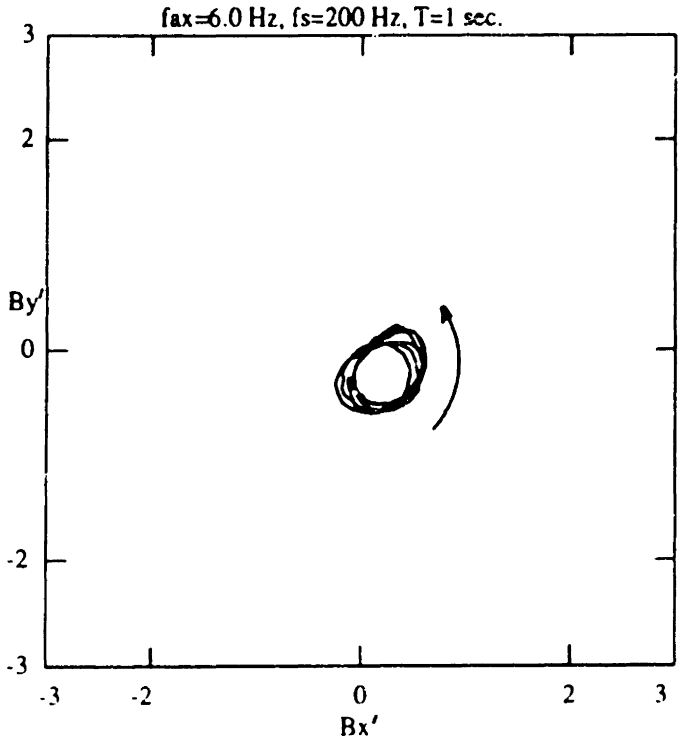

Figure 6.11: Bending x' versus Bending y', f_{ax} = 6.0 Hz

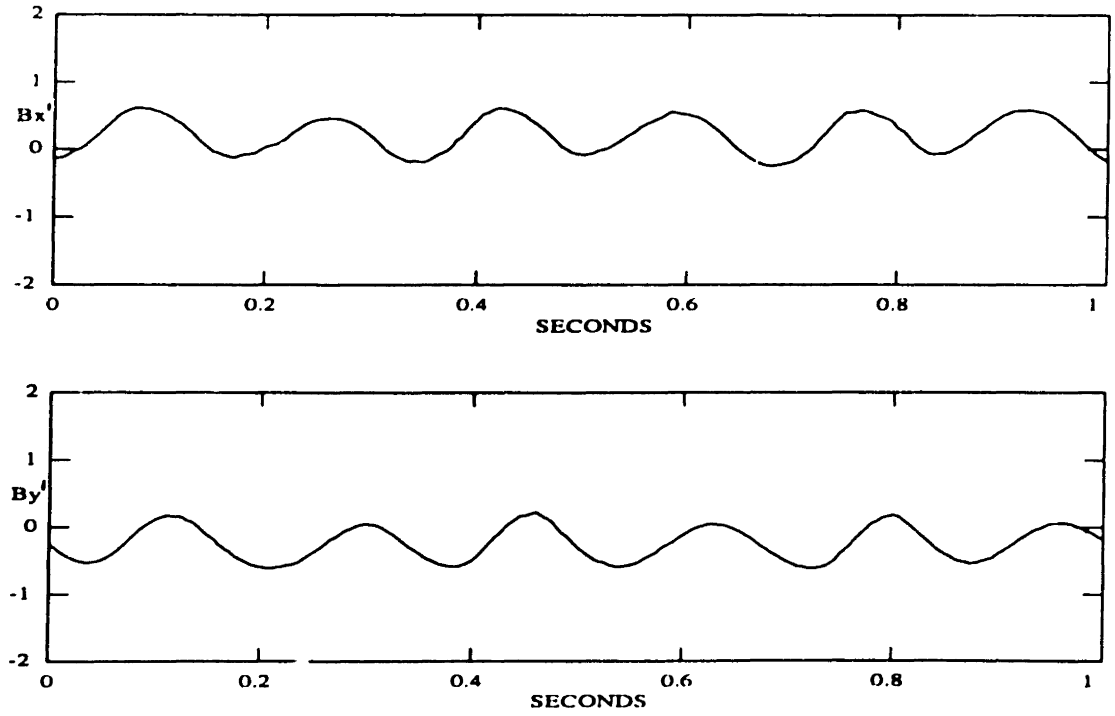

Figure 6.12: Bending x' and Bending y' Time History, f_{ax} = 6.0 Hz

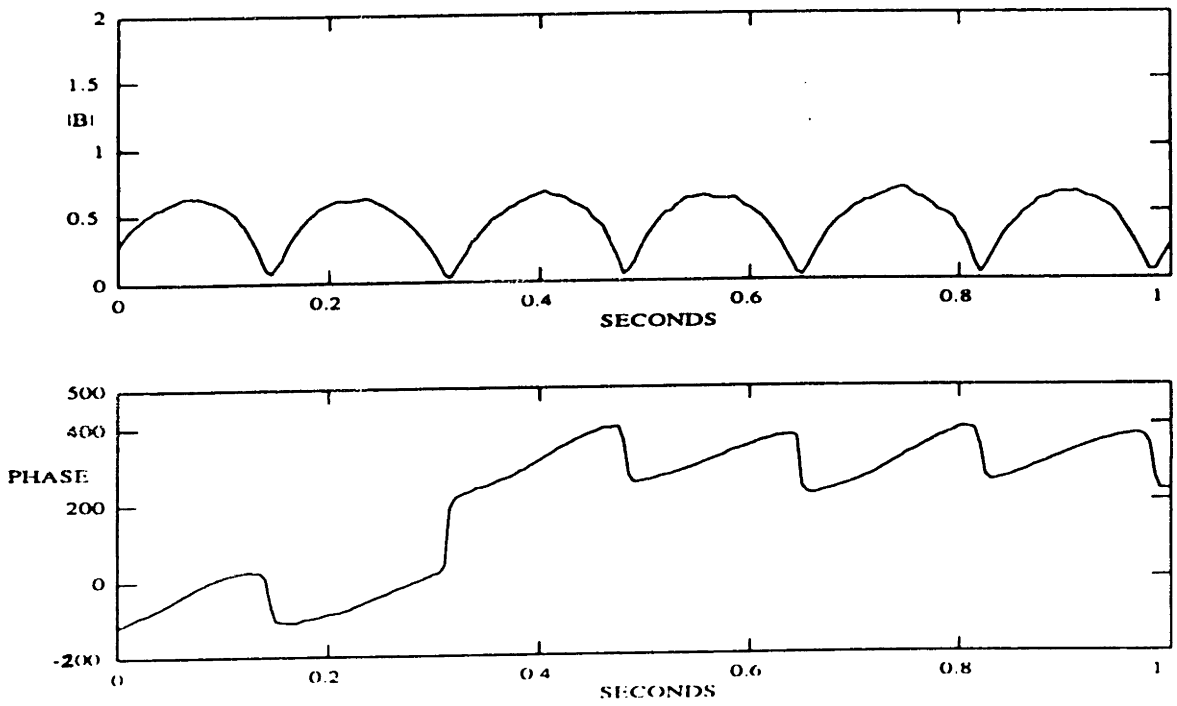

Figure 6.13: Bending Magnitude and Phase, f_{az} = 6.0 Hz

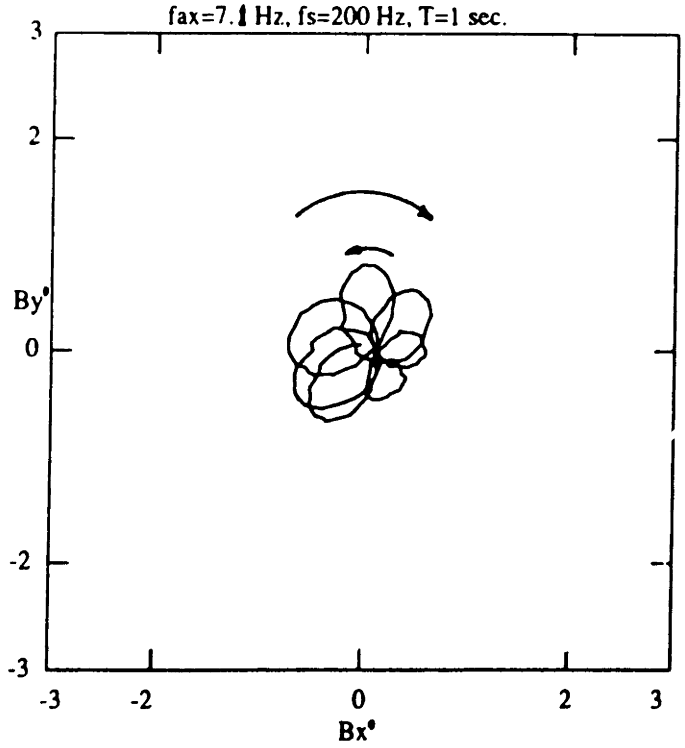

Figure 6.14: Bending x' versus Bending y', f_{az} = 7.1 Hz

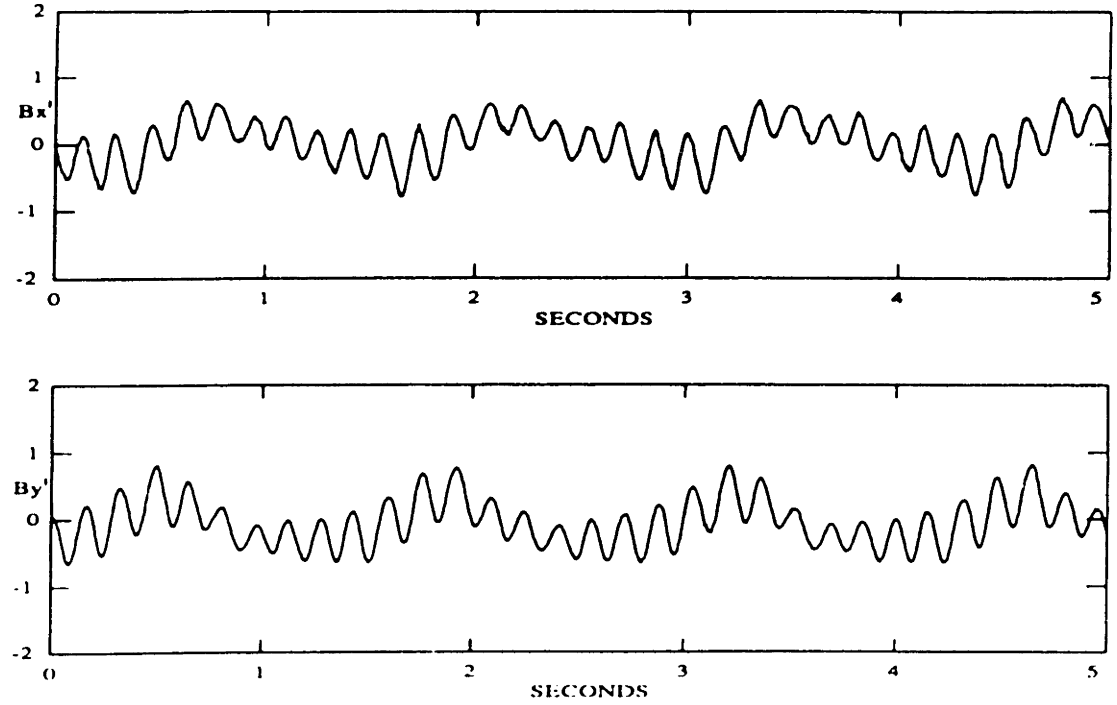

Figure 6.15: Bending x' and Bending y' Time History, $f_{az} = 7.1$ Hz

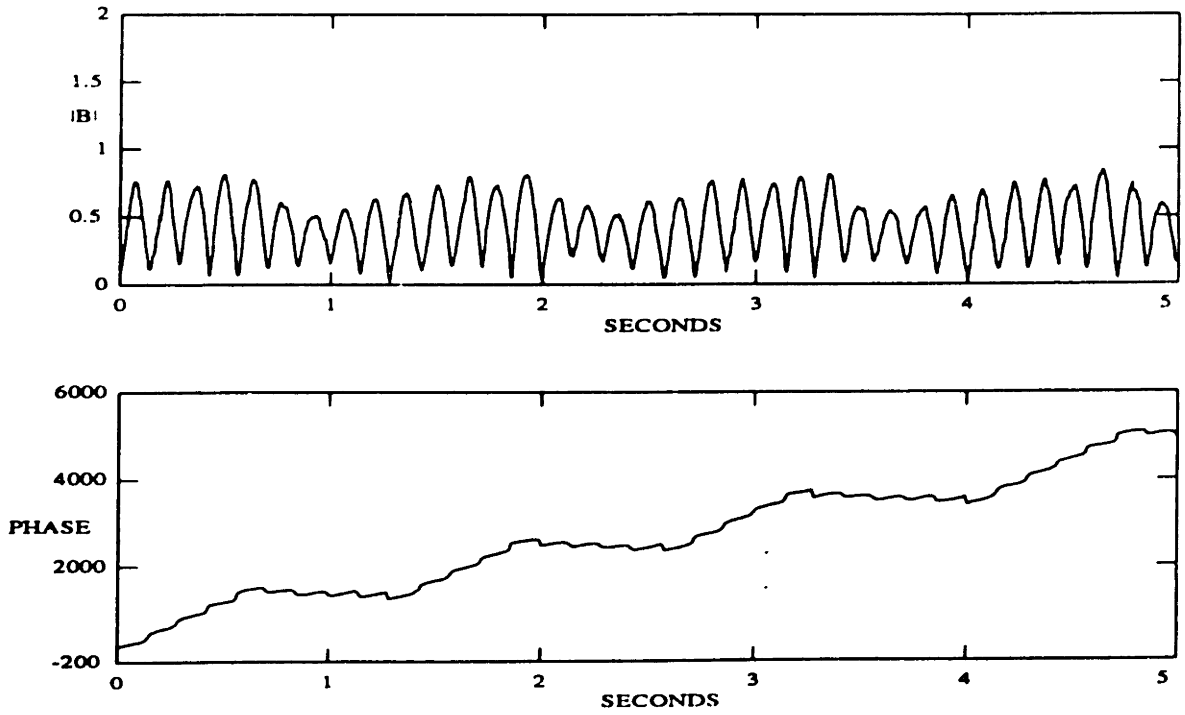

Figure 6.16: Bending Magnitude and Phase, $f_{az} = 7.1$ Hz

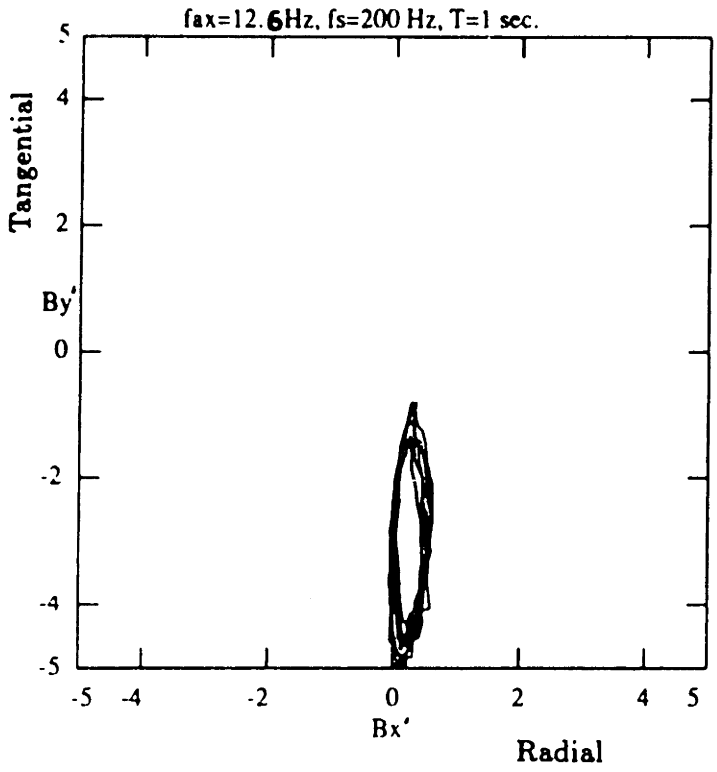

Figure 6.17: Bending x' versus Bending y', f_{az} = 12.6 Hz

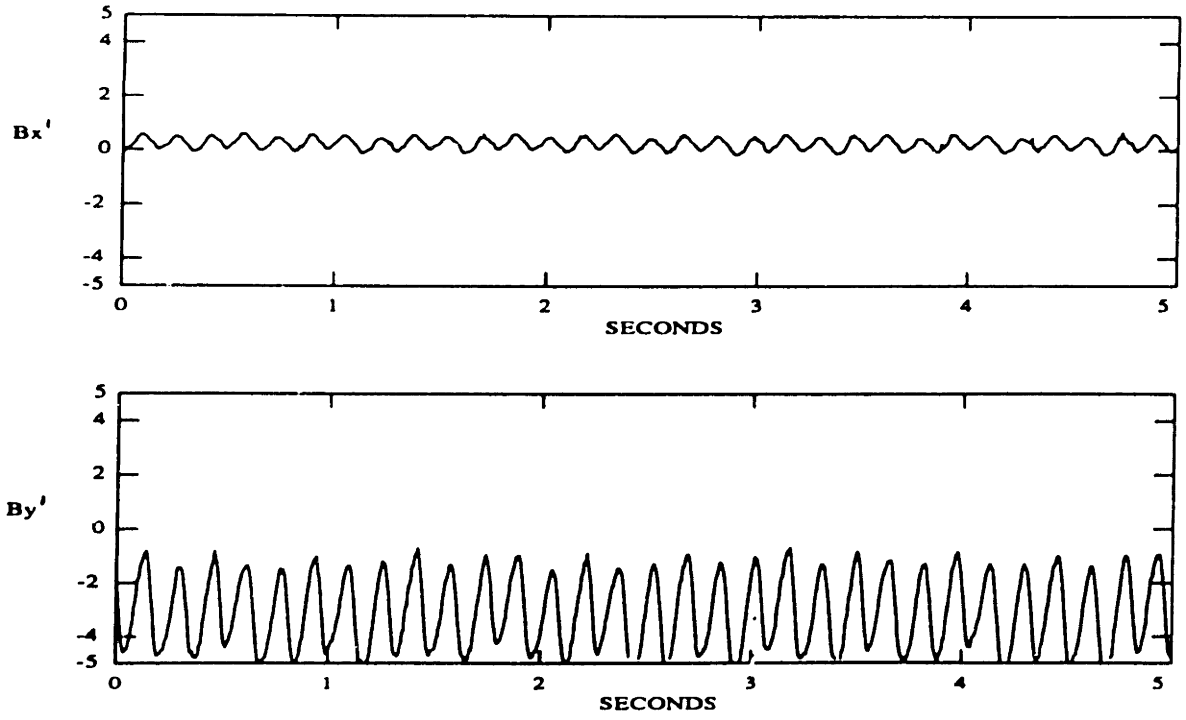

Figure 6.18: Bending x' and Bending y' Time History, f_{az} = 12.6 Hz

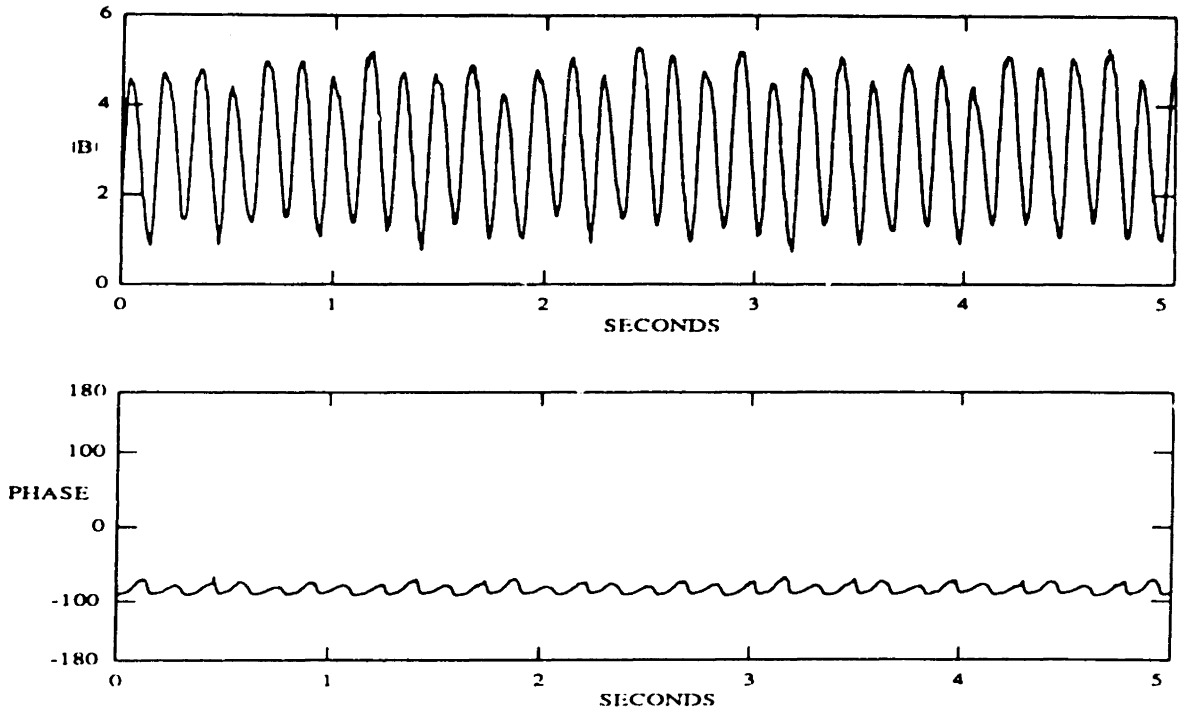

Figure 6.19: Bending Magnitude and Phase, $f_{az} = 12.6$ Hz

Chapter 7

Field Tests

A series of downhole vibration tests were conducted in Quitman, Texas, in August of 1984. This experiment was a joint effort of Shell Development Co. and NL Industries. The purpose of the test was to record the BHA vibration near the bit. The data from this experiment were made available to this research project.

7.1 Background

The downhole sensors package of this experiment included the transducers for WOB, TOB, two perpendicular bending measurements, and three axes of acceleration measurements. The sensor package has been described in [52]. A sketch of the sensor package is shown in Figure 7.1 . The signals from the sensors were first sampled by an A/D system, then, the data were transmitted to the surface by a hardwired telemetry system. For the results presented here five sensors were sampled in a given test at 130 Hz per channel. The channels to be sampled were selected by the control system at the surface. A total of 60 hours of data were taken during this experiment. Following is a summary of the experiment

- Bit type used : Tri-cone and PDC bits
- Footage drilled : 4000' to 7000' in a vertical well through shale, limestone, and sandstone

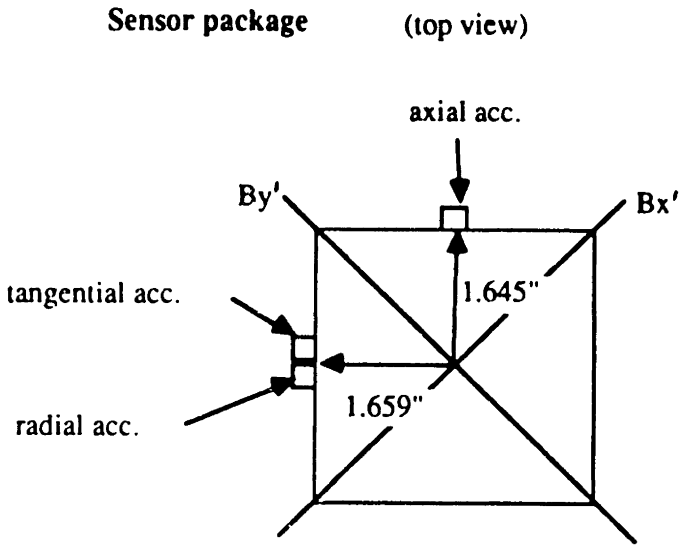

Figure 7.1: Top View of the Sensor Package

- RPM : 50 to 200

This set of data is unique because of the high data rate provided by the hardwired telemetry system.

7.2 Data Processing

The accelerometers used were not suitable for making low frequency measurement, such as experienced in forward synchronous whirl. Furthermore, the accelerometers are much more sensitive to wall impact than strain gages. For these reasons, the bending moment data are emphasized in the results shown below which specifically emphasize whirling behavior.

From the raw time histories, we have learned that the measurements are often very random in nature, seldom remaining stationary for a long period of time. In order to resolve the spectral peaks, the Maximum Entropy Method (MEM) was used

exclusively to estimate the spectral results. This method is known for its ability to give high resolution estimates of the spectrum from relatively short records, making it suitable for processing these data.

7.3 Case Studies of the Bending Vibration and Whirling Motion

Due to a lack of adequate downhole vibration data, very little has been known about the actual bending dynamics experienced by the drill string while rotary drilling, and about the contributions of bending vibration to drill string deterioration and failure. Recently, downhole vibration recorders and systems with hardwires to the surface have provided much needed data and insight into events downhole. At first glance, the data appears, even to the experienced vibration analyst, extremely complex. Many different vibration phenomena occur simultaneously, making it difficult to isolate, evaluate, and explain any one of them. To varying degrees, axial, torsional and bending vibration are all present and at times intimately coupled. Bit bounce, stick slip, forward and backward whirl, and linear and parametric coupling between axial and bending vibration all occur.

Several authors have made recent contributions to the measurement of bending vibration of BHA's. Wolf et al, [52], present samples of downhole vibration data acquired in the same well as the data presented here. Included in the paper are several suspected cases of whirling. The paper by Besaisow et al, [6], also shows suspected examples of bending vibration and whirling. Burgess, et al, [9], specifically conclude that transverse vibration is a source of downhole MWD tool failure, and cite a method for reducing downhole failures. Close et al, [13], present downhole recordings of large amplitude bending vibration.

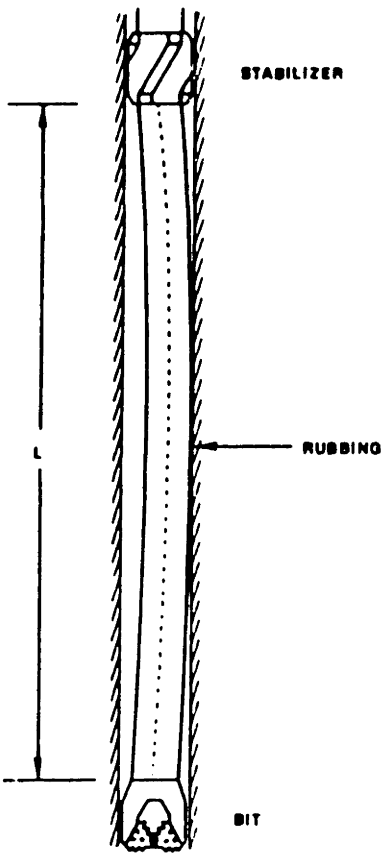

Figure 7.2: Whirling Drill Collar

7.3.1 Bending Moment Measurements

Bending moments are determined by the curvature of the drill collar. Referring to Figure 7.2, let the deflection of the collar center as a function of z, the axial coordinate, be designated by $v_o(z,t)$. As an approximation to the actual deflection assume that the whirl deflected shape of the drill collar is the half sine wave given by:

$$v_o(z,t) = (R_b - R_c)sin(\pi z/L)F(t) \tag{7.1}$$

where L is the length of the drill collar section from the bit to the stabilizer and F(t) is an arbitrary function of time. Thus, in this instance, Figure 7.3 depicts a cross section at the midspan of the drill collar. The bending moment corresponding to $v_o(z,t)$ is given by the moment-curvature relationship

$$B(z,t) = EI\frac{d^2v_o}{dz^2} = -(R_b - R_c)(EI\pi^2/L^2)sin(\pi z/L)F(t) \tag{7.2}$$

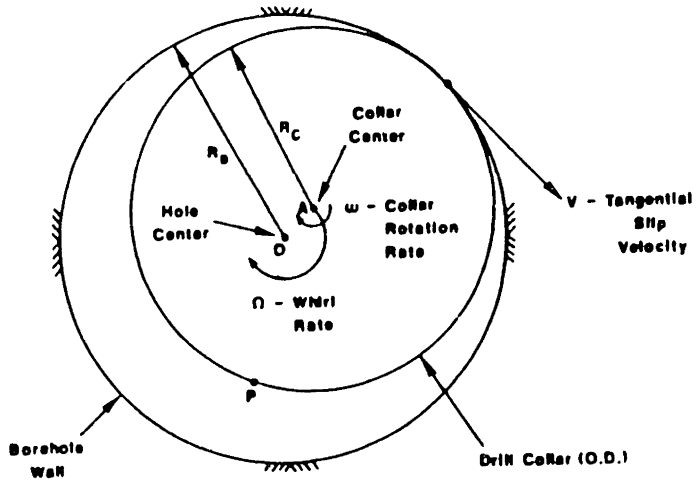

Figure 7.3: Cross Section of Borehole and Whirling Drill Collar

where E is the modulus of elasticity and I is the moment of inertia of the collar.

In the field test, the bending moment B(z,t) was measured at a single location by two orthogonally oriented strain gage bridges, mounted in the rotating drill collar at a location about nine feet above the bit. These bridges yielded the two vector components $B_{x'}(t)$ and $B_{y'}(t)$. The measured bending moment is then a vector in an orthogonal $x' - y' - z$ coordinate system, attached to the centerline of the hole and rotating with the drill collar at ω. z is assumed to increase with depth so that ω is clockwise positive looking down hole. The coordinate system, measured bending moment and phase angle are defined in Figure 7.4, and in the following equation,

$$\vec{B}(t) = B_{x'}(t)\vec{i} + B_{y'}(t)\vec{j} \tag{7.3a}$$

$$\vec{B}(t) = |B|\,[cos(\phi(t))\vec{i} + sin(\phi(t))\vec{j}] \tag{7.3b}$$

where $\phi(t)$ is the angle that the bending moment vector makes with the rotating $x' - y'$ coordinate system and i and j are unit vectors in the x' and y' directions. If it is assumed that the drill collar is rotating at ω and whirling at Ω, then this equation

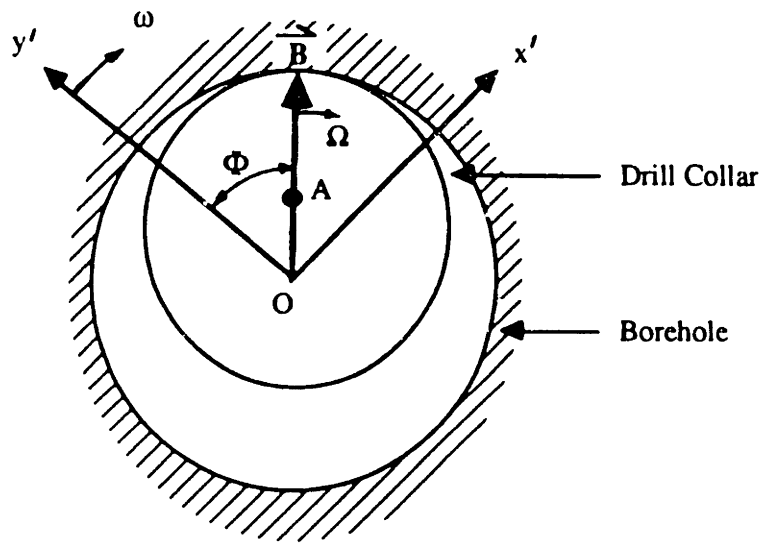

O : Center of the Borehole

Figure 7.4: Coordinate System, Bending Moment, and Phase Angle Definition

may be expressed as shown below:

$$\vec{B}(t) = |B|\,[cos((\omega - \Omega)t)\vec{i} + sin((\omega - \Omega)t)\vec{j}] \tag{7.4}$$

The rotating $x' - y'$ coordinate system representation is particularly useful, because it represents the bending moment time history that is experienced by the collar and is therefore a measure of the stress time history which is relevant to cyclic fatigue damage. An important feature of this expression is that the bending moment, and hence the bending stresses, vary as the difference between the drill collar rotation rate, ω, and the whirl rate, Ω. The difference frequency is the frequency of stress cycles which would be experienced by the drill collar under whirling conditions.

Equation 7.4 is valid for all whirling conditions, whether or not in contact with the wall. One must only evaluate the magnitude and correct sign (plus for clockwise rotation and minus for counter-clockwise rotation) of the drill collar rotation and whirl rates. The unwrapped phase angle, $\phi(t)$ can be estimated from $B_{x'}(t)$ and

$B_{y'}(t)$, the independently measured bending moment components, as follows, where ϕ_o is a constant depending on initial conditions.

$$\phi(t) = \arctan[B_{y'}(t)/B_{x'}(t)] + \phi_o \quad (7.5a)$$

$$= \arctan[sin((\omega - \Omega)t)/cos((\omega - \Omega)t)] + \phi_o$$

$$= (\omega - \Omega)t + \phi_o \quad (7.5b)$$

$$\dot{\phi}(t) = \frac{d\phi}{dt} = (\omega - \Omega) \quad (7.5c)$$

Therefore, from two independent and orthogonal bending moment measurements the difference between the whirl rate and drill collar rotation rate can be determined. In the case studies, plots of $\phi(t)$ will often be presented. The slope of these plots is the phase rate, $\dot{\phi}$, which from equation 7.5c for whirling, is the difference frequency $(\omega - \Omega)$. Since the rotation rate ω is usually known from surface observation, then the whirl rate Ω can be deduced. The term 'unwrapped' phase angle refers to the way the arctan function is computed from real data. The arctan function used here is not restricted to a range of $-\pi$ to $+\pi$. Rather, the phase angle is meant to accumulate linearly with time as shown in equation 7.5b.

Linear coupling between axial force and lateral deflection also produces time varying changes in bending moment. Unfortunately, because whirling produces curvature, and curvature is needed for linear coupling to occur, then the two phenomena are likely to occur together. As a result, bending moment measurements would contain components due to the whirling at the difference frequency $(\omega - \Omega)$ and also components due to the linear coupling to the axial force at the bit, which for the purpose of discussion is assumed to be at a frequency ω_a. When both sources of vibration are present to a significant degree in the measurement, then attempts to use the unwrapped phase $\phi(t)$ from equation 7.5a may be impossible. However, computation of the autospectra of either the x or y components of the bending moment should reveal strong peaks at both $(\omega - \Omega)$ and ω_a.

As discussed above, the various bending vibration mechanisms do not generally

occur one at a time, but in fact many phenomena may occur simultaneously. As a consequence, the bending moment and phase angle time histories are rarely as simple as those shown in equations 7.5b and 7.5c. They are usually much more complex. On occasion, single phenomena do dominate. The case studies shown below have been carefully selected to separately reveal dominant examples of each mechanism.

7.3.2 Drilling Case Studies

In this section, examples of drill collar whirling, linear coupling of axial and bending vibrations, and parametric excited bending vibration are presented. All cases described here were for pendulum BHA's. In Cases 1, 2 , 3 , and 6, the sensor package was placed just above the bit, with 59.8 feet separating the bit and the center of the first stabilizer, and 35.2 feet between the centers of the first and second stabilizers. The drill collar between the first and second stabilizer was 6.25 inches, outside diameter. The remainder of the BHA was typically composed of 19 to 23, 6.25 inch drill collars above the second stabilizer. In Cases 4 and 5, the sensors are placed just above the second stabilizer. The length from the bit to the middle of the first stabilizer was approximately 65 feet, and from the first to the second stabilizer, 35 feet.

Six case studies are presented here, carefully chosen to illustrate the variety of phenomena described in previous chapters. Considerable use is made of the bending moment measurements, $B_{x'}(t)$ and $B_{y'}(t)$, and the bending moment phase angle $\phi(t)$, which is useful in determining the type of whirl and the whirl rate. For the Quitman experiment, RPM was not electronically recorded. For some tests downhole magnetometer data was available, from which RPM can be deduced. For the six cases presented here, which best represent the phenomena under study, magnetometer data were not available. Occasional surface logbook entries were the only record of RPM. This handicap was overcome by extracting the information from the other measurements, for example, dynamic WOB.

7.3.3 Case 1: No Whirl And Simple Rotation of a Curved Drill Collar.

Figure 7.5 shows a two second time history for the bending moment components $B_{x'}$ and $B_{y'}$ and Figure 7.6 shows $\phi(t)$, the unwrapped phase angle. The data was acquired while drilling with a PDC bit through shale at an average rate of penetration of 11 ft/hr at depth of approximately 6846 feet. There were 16 drill collars, jars, and 5 more drill collars above the second stabilizer. From only the bending moment time series, it is impossible to deduce the behavior of the drill collar. The plot of the time history of the phase angle $\phi(t)$ reveals a mean phase rate or slope of about 500 degrees/sec., which is equal to approximately 1.4 Hz (84 RPM). This is confirmed by computing the spectrum of $B_x(t)$, as shown in Figure 7.7, which has its highest peak at 1.36 Hz. If it is assumed that there was no whirl, then from equation 7.4 with Ω set equal to zero, we conclude that the rotary speed ω was 1.36 Hz (81.6 RPM). For this data set, there was no magnetometer recording of RPM. However, a manual record kept in a surface logbook indicated that the surface rotation rate was approximately 80 RPM.

It is interpreted that the drill collar was bent, probably rubbing against the wall, but not whirling. The strain gages were exposed to a bending moment of approximately 10000 ft-lb peak to peak. Some additional bending vibration was superimposed on top of that due to the curvature and rotation. This vibration was probably caused by coupling with bit forces or bumping against the wall.

7.3.4 Case 2: Forward Synchronous Whirl $\omega = \Omega$

Figure 7.8 shows the time histories for the bending moments and Figure 7.9 shows the unwrapped phase angle. The data was acquired while drilling through shale with a PDC bit at an average rate of penetration of 60 ft/hr at depth of 4366 feet. The rotary speed, manually logged at the surface, was 116 RPM. There were 23, 6.25 inch drill collars above the second stabilizer. The time history for the phase angle, shown

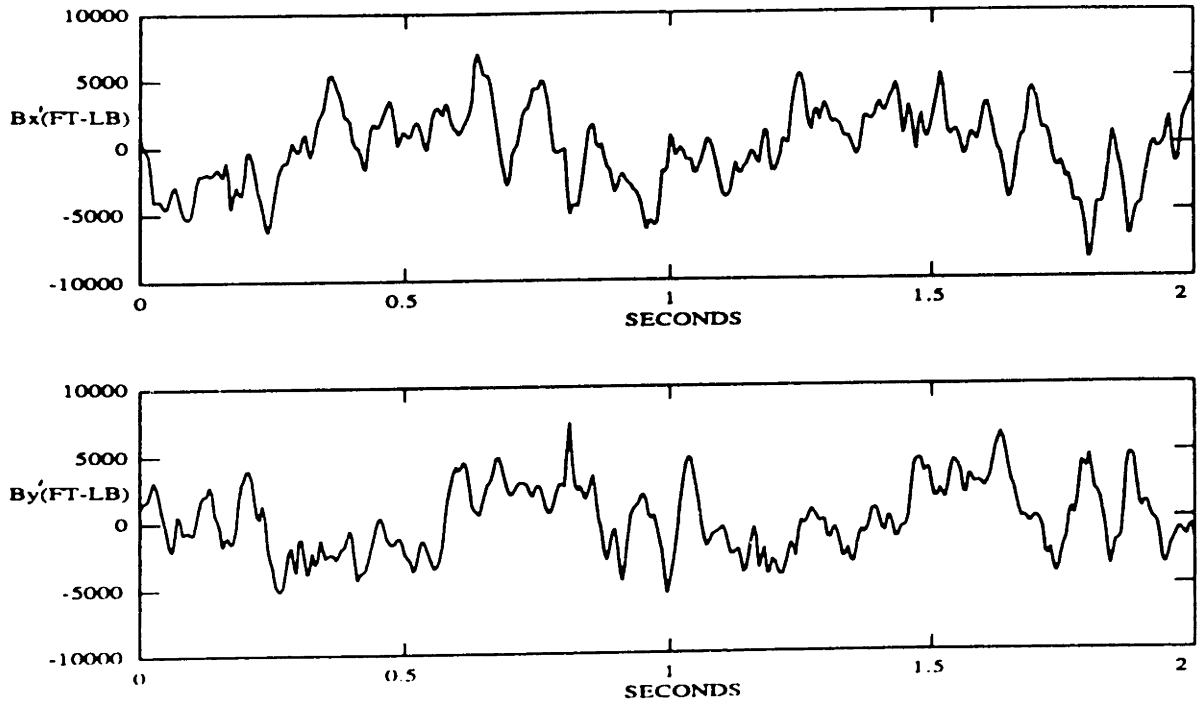

Figure 7.5: Time History of the Bending Moments for Case 1: No Whirl, Pure Rotation

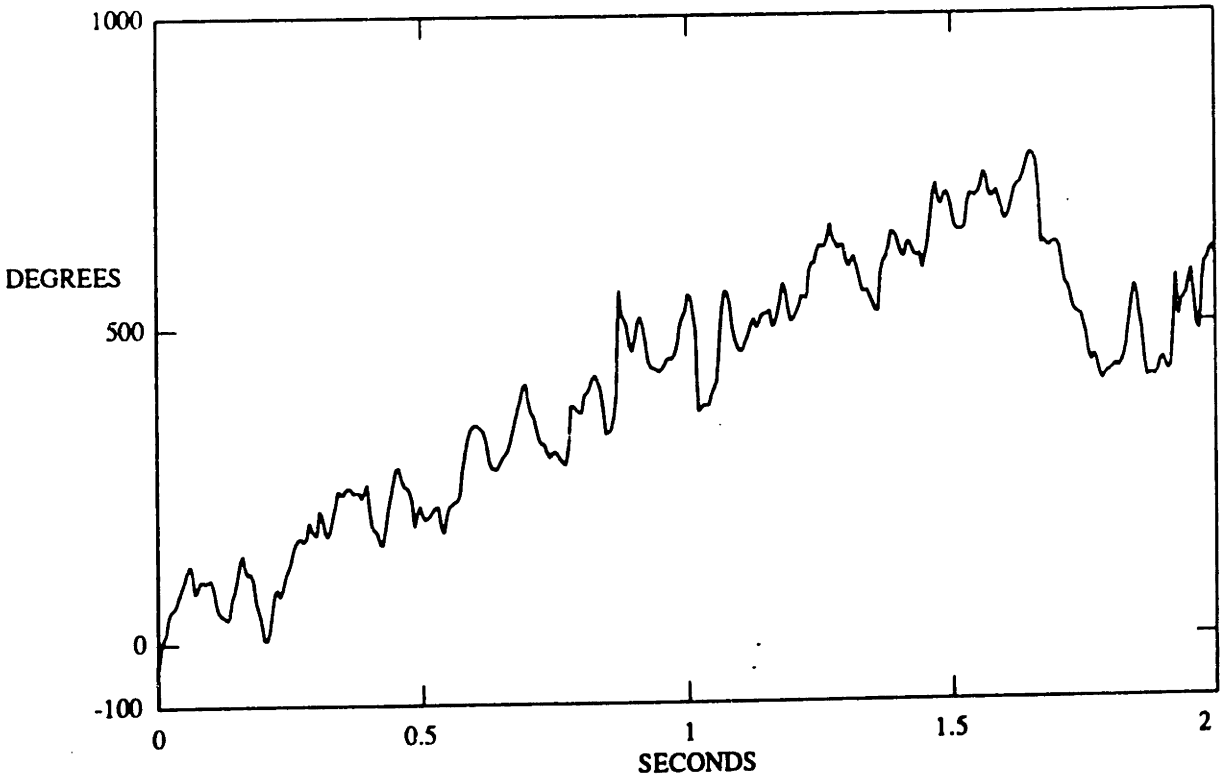

Figure 7.6: Time History of Unwrapped Phase Angle for Case 1: No Whirl, Pure Rotation

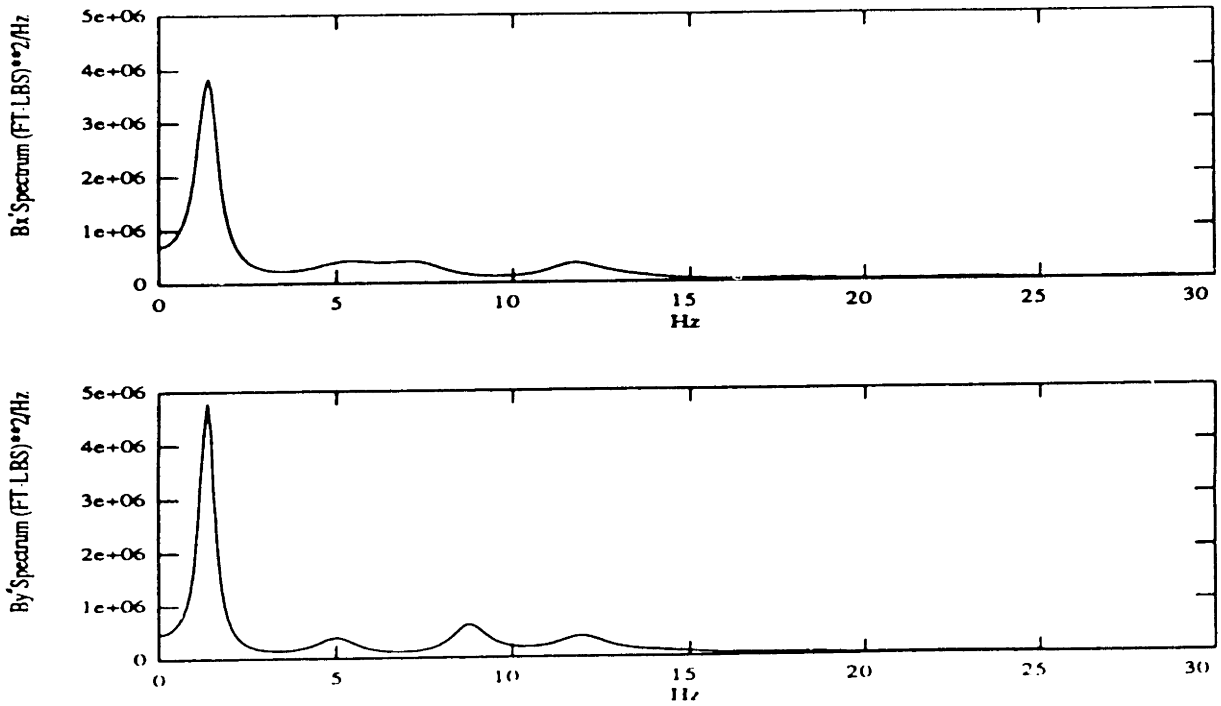

Figure 7.7: Bending Moment Spectra for Case 1: No Whirl, Pure Rotation

in Figure 7.9, reveals that the mean phase angle remained constant. Vibration, not whirling, is revealed as additional fluctuations in phase angle about the mean. Figure 7.10 shows the bending moment spectra, which reveal peaks at 1.85 Hz.(111 RPM), which is close to the reported rotation rate of 116 RPM.

The interpretation for this case is that the zero average phase rate indicates that the drill collar was exhibiting forward synchronous whirl. The peak in the bending moment spectra at 1.85 Hz.(111 RPM) indicates that some additional rotation rate vibration was also occurring. This vibration was probably caused by the collar hitting the wall once per rotation. However, any cause which would result in a once per revolution perturbation in the circular whirl orbit would have the same result.

7.3.5 Case 3: Backward Whirl With Little Slip

Figure 7.11 shows the time history for the bending moments and Figure 7.12 shows the phase angle. The data was acquired while drilling through limestone with a tri-cone bit at an average rate of penetration of 18 ft/hr at depth 5259 feet. The BHA

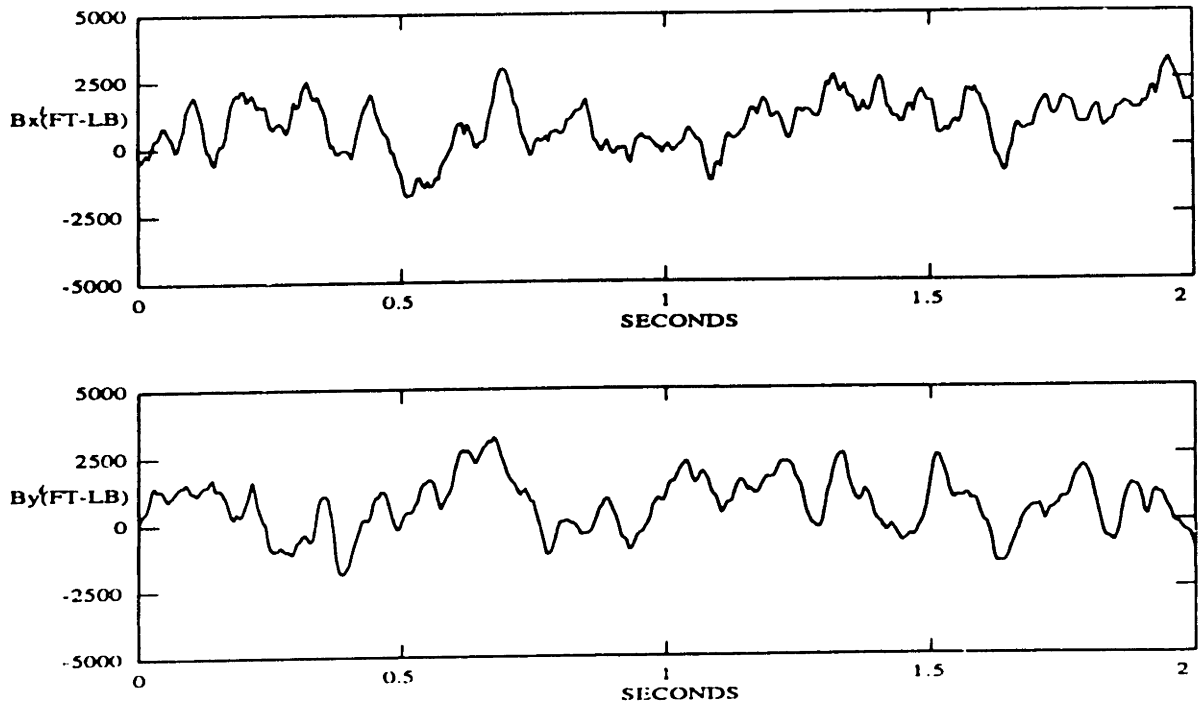

Figure 7.8: Time History of Bending Moments for Case 2: Forward Synchronous Whirl

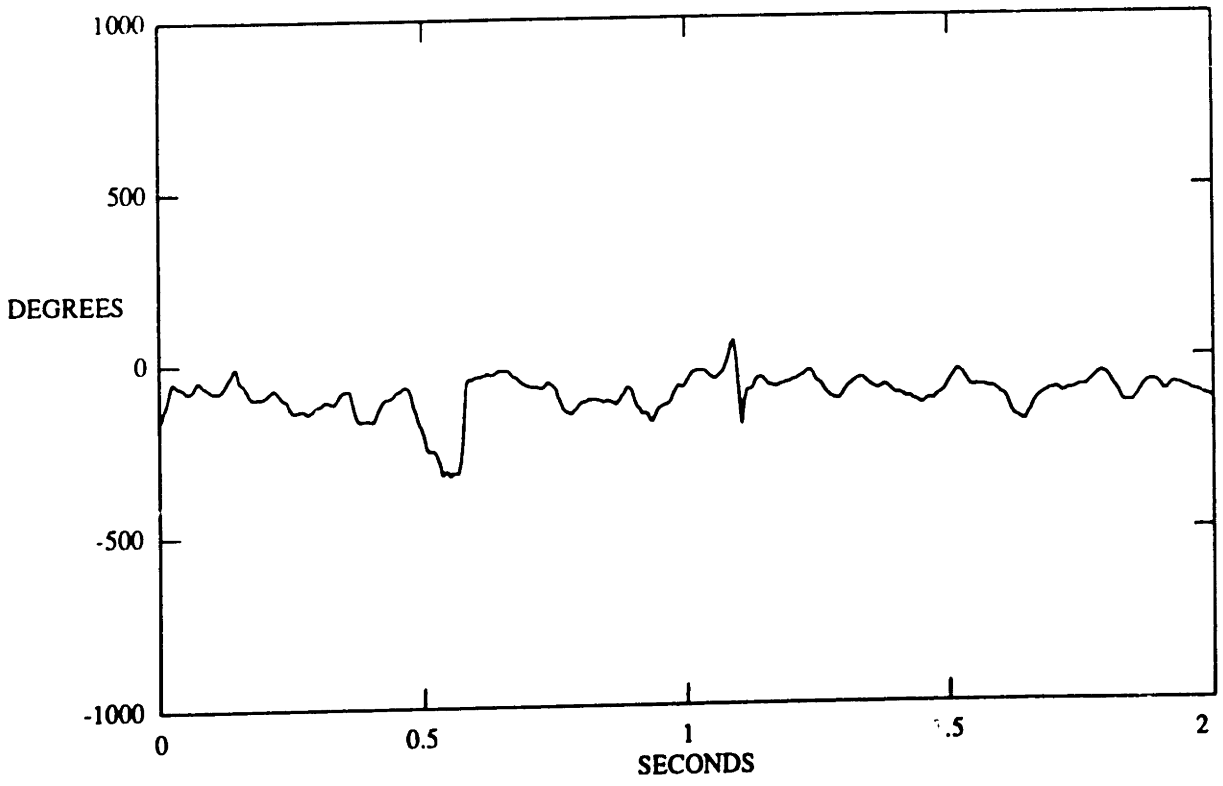

Figure 7.9: Time History of Phase Angle for Case 2: Forward Synchronous Whirl

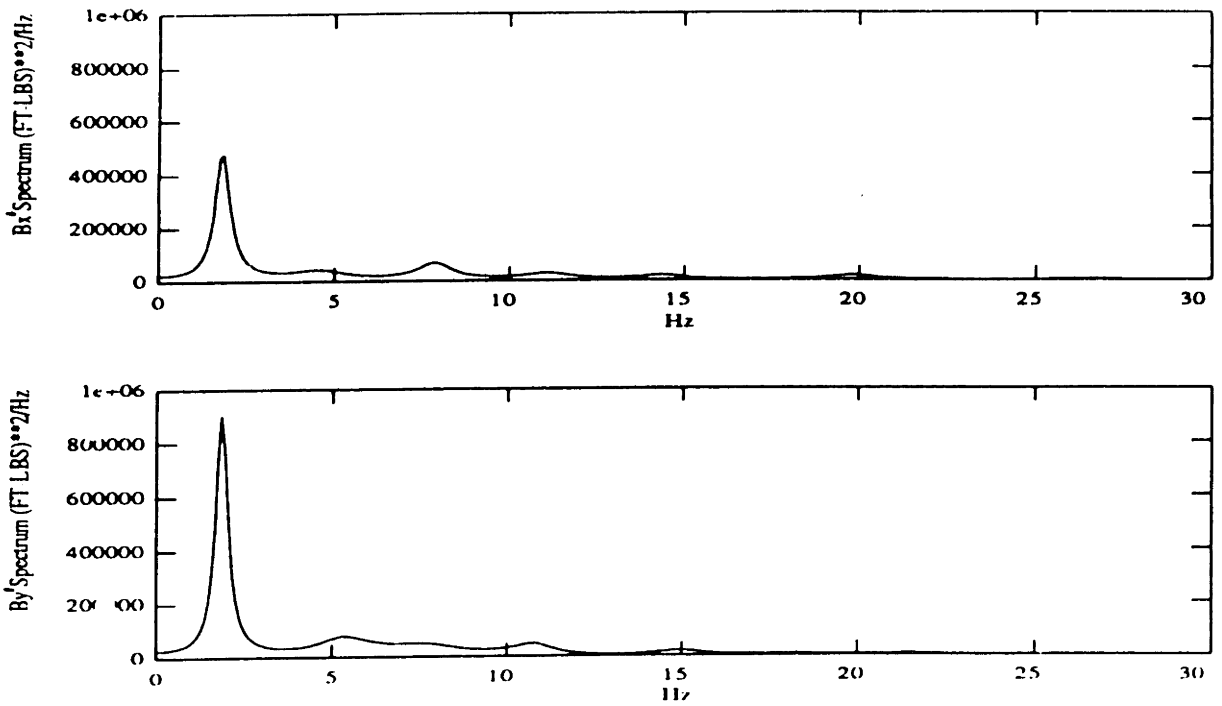

Figure 7.10: Bending Moment Spectra for Case 2: Forward Synchronous Whirl

was a pendulum assembly with 20 drill collars, jars and 9 heavy weight drill pipe above the second stabilizer. The bending moment time series reveal peak to peak amplitudes of about 25,000 ft-lbs, which is several times greater than seen in the two previous examples. Figure 7.12 reveals an excellent example of the phase angle $\phi(t)$ during backward whirl. The mean phase rate or slope of the plot is a constant 1900 deg./sec., which equates to 5.28 Hz. The spectra for $B_{x'}$ and $B_{y'}$ shown in Figure 7.13 also reveal strong peaks at 5.28 Hz.

If the assumption is made that this is a case of backward whirl with no slip, then equation 5.2 would predict that Ω_b = -4ω, and the difference frequency or phase rate predicted by equation 7.5c would be at five times the rotation rate, as shown in the following expression:

$$(\Omega_b - \omega)/2\pi = -5\omega/2\pi = 5.28Hz$$

From this, the conclusion is reached that the rotation rate $\omega/2\pi$ was 1.06 Hz (63 RPM). For this case, the surface speed was reported in the logbook as 80 RPM.

The explanation for the discrepancy between the reported rotary speed of 80 RPM

and the calculated drill collar rotation rate of 63 RPM is not certain. One possibility is a reporting error, because the RPM was only occasionally written down. However, a more likely explanation is that the collar was slipping some as it whirled. If it is required that the rotation rate be as recorded, $\omega/2\pi$ = 1.33 Hz (80 RPM), then it is concluded from Equation 7.5c that

$$(\omega - \Omega)/2\pi = 5.28Hz$$

$$\Omega/2\pi = -3.95Hz$$

as opposed to

$$\Omega_b/2\pi = 4\omega/2\pi = -5.32Hz$$

which would be expected under no slip conditions. From equation 5.2, the whirl ratio, s, is concluded to be 0.74. In the absence of an accurate determination of surface rotation rate, it is concluded that this is an example of backward whirl with some slip, although it is possible that there was no slip. Figure 7.14 is plot of $B_{x'}(t)$ versus $B_{y'}(t)$ for this example. Each of the four images presents 0.5 seconds of the total 2.0 seconds of bending moment data. In the absence of superimposed vibration, the whirling would be expected to produce orbits in a plots such as these with a frequency equal to the phase rate of 5.28 Hz. These plots make it clear that even though whirling is the dominant phenomenon in this example, there is substantial additional motion of the drill collar due to other sources of vibration.

7.3.6 Case 4: Backward Whirl With Substantial Slip

Figure 7.15 shows the time history for the bending moments and Figure 7.16 shows the phase angle. The data was recorded while drilling with a tri-cone insert bit, in shale, at a depth of 6897 feet. The reported rotary speed was 60 RPM (1.0 Hz). The BHA was a pendulum assembly, as described earlier, with the NBMS, followed by fourteen, 6.25 inches collars between the second stabilizer and the jars and five drill collars above the jars. The reported measurements thus came from a point a few feet

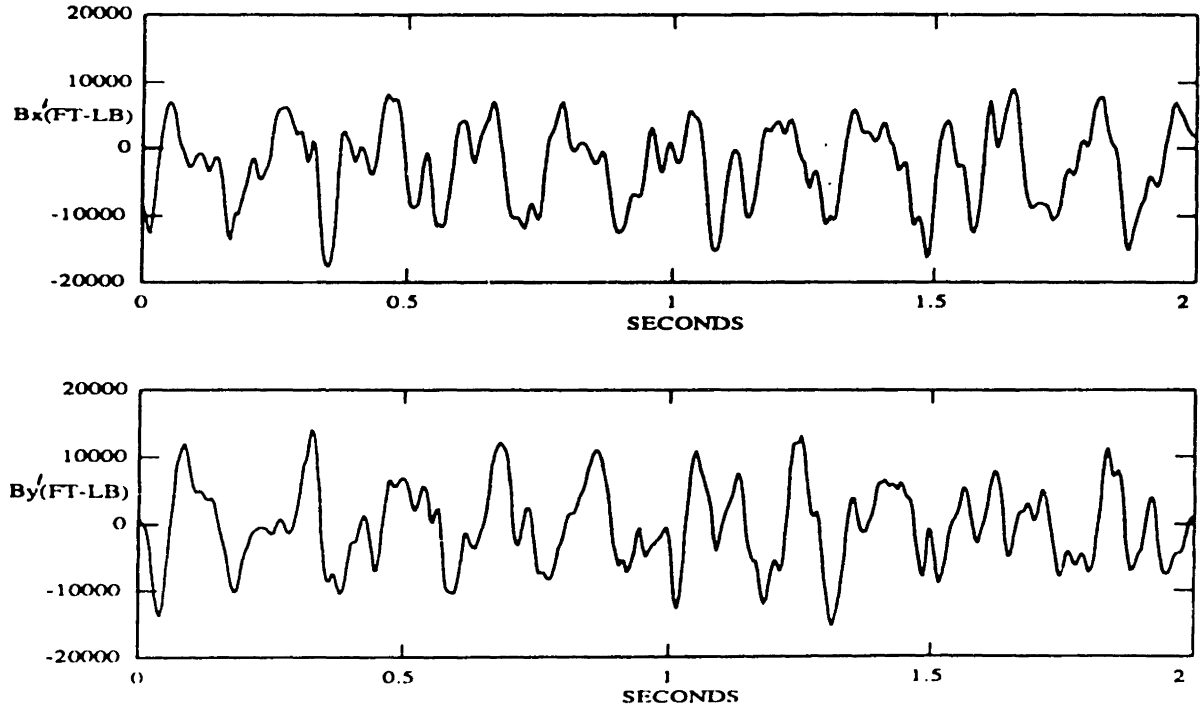

Figure 7.11: Time History of Bending Moments for Case 3: Backward Whirl with Little Slip, s = .75

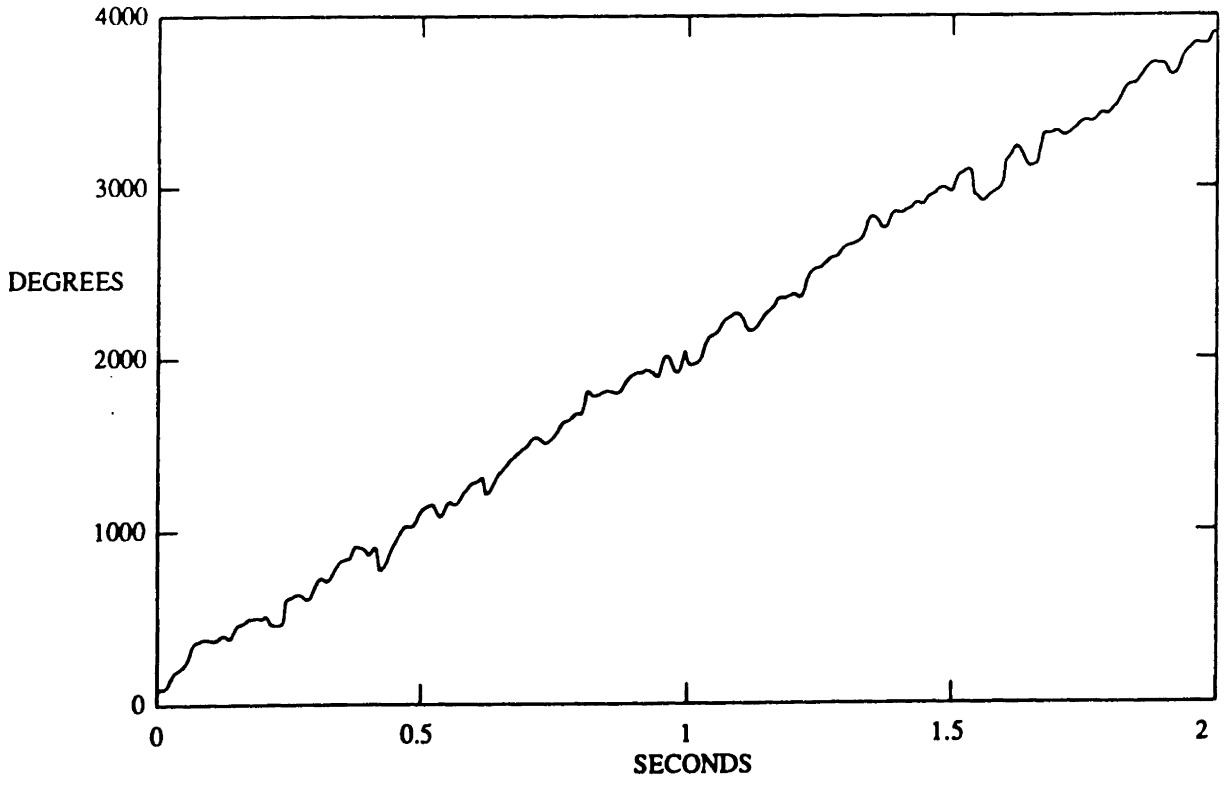

Figure 7.12: Time History of Phase Angle for Case 3: Backward Whirl with Little Slip, s = .75

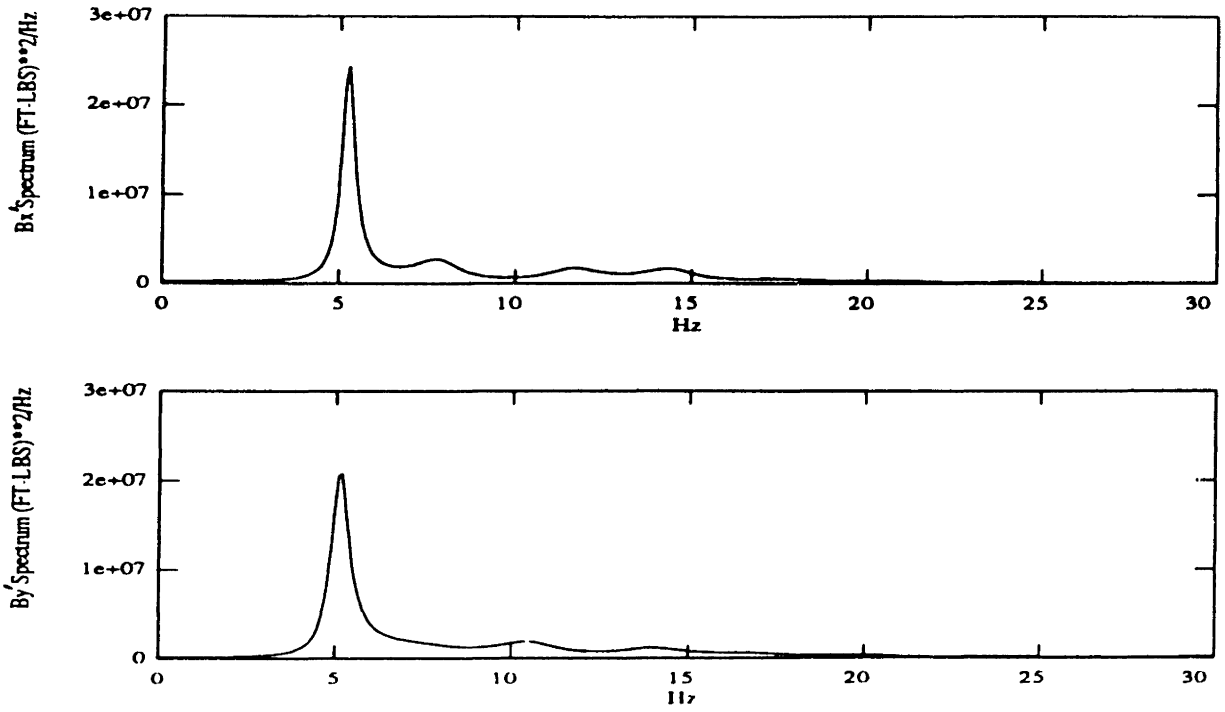

Figure 7.13: Bending Moment Spectra for Case 3: Backward Whirl with Little Slip, s = .75

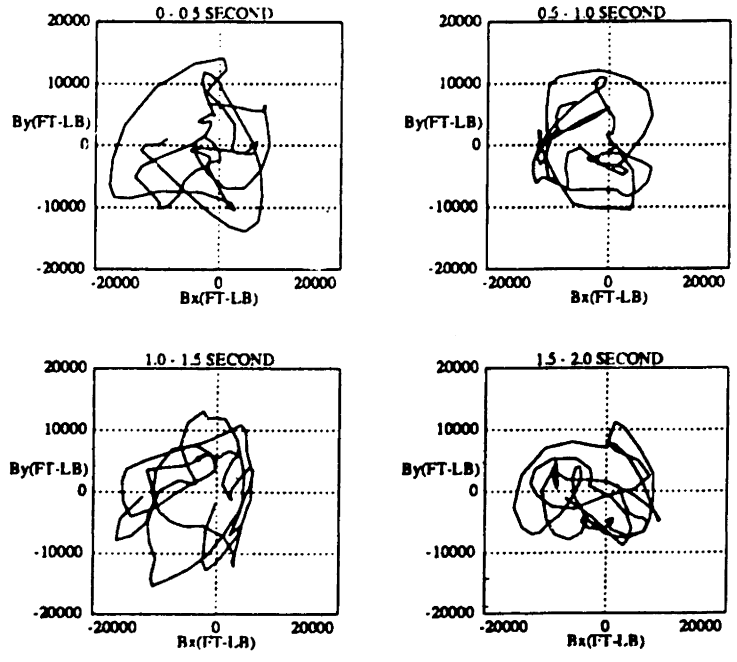

Figure 7.14: Orbital Plots of Bending Moments for Case 3: Backward Whirl with Little Slip, s = .75

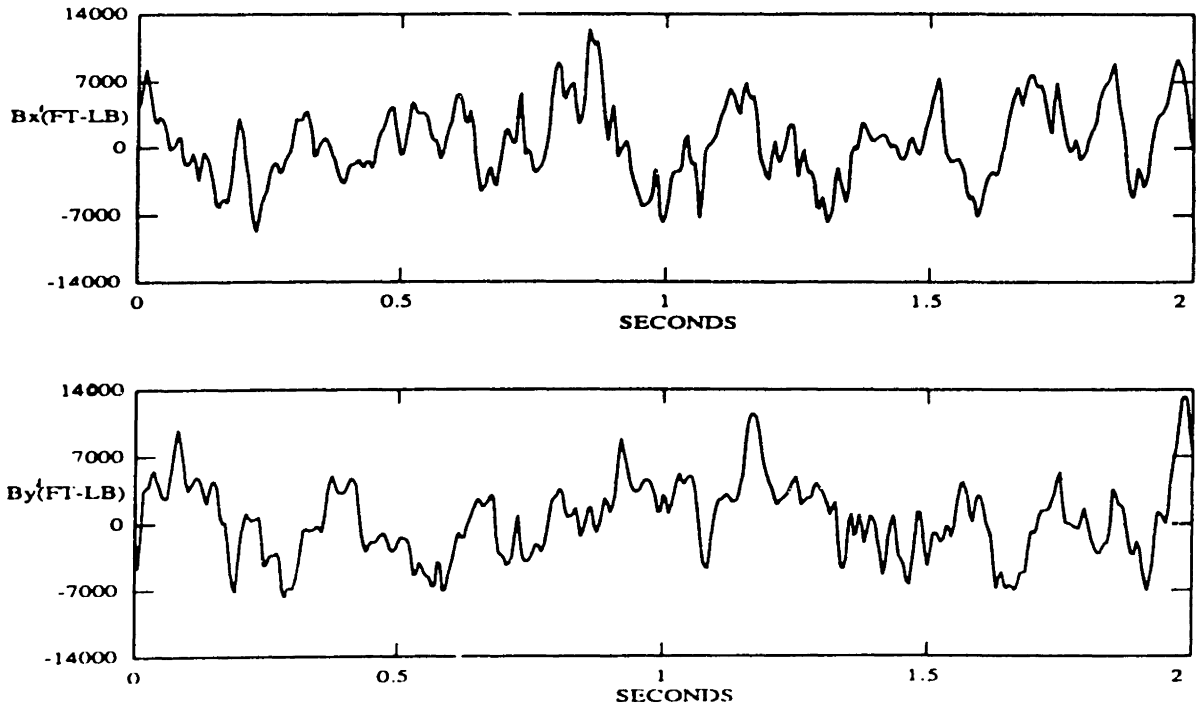

Figure 7.15: Time History of Bending Moments for Case 4: Backward Whirl with Substantial Slip, s = .58

above the second stabilizer.

Figure 7.16 shows that the mean phase rate was 1200 degrees/sec (3.33 Hz). Thus, the difference frequency, $(\omega - \Omega)/2\pi$, was 3.33 Hz. This is verified by the location of the peaks of the bending moment spectra, shown in Figure 7.17. Requiring $\omega/2\pi$ to be 1.0 Hz. results in an estimate for $\Omega/2\pi$ of -2.33 Hz. Using Equation 5.2, the backward whirl rate without slip is predicted to be $\Omega_b = -4\omega$ = -4.0 Hz. The actual backward whirl rate is about half that expected with no slip, and the whirl ratio computed from equation 5.3 is, therefore, s = 0.58. The drill collar was backward whirling and slipping at the same time.

Even with the admitted uncertainty in the recorded RPM, it is extremely unlikely that the surface RPM was less than 60. If the surface RPM was greater than 60 RPM reported, then calculations similar to the ones conducted above would reveal that the drill collar was backward whirling and slipping even more.

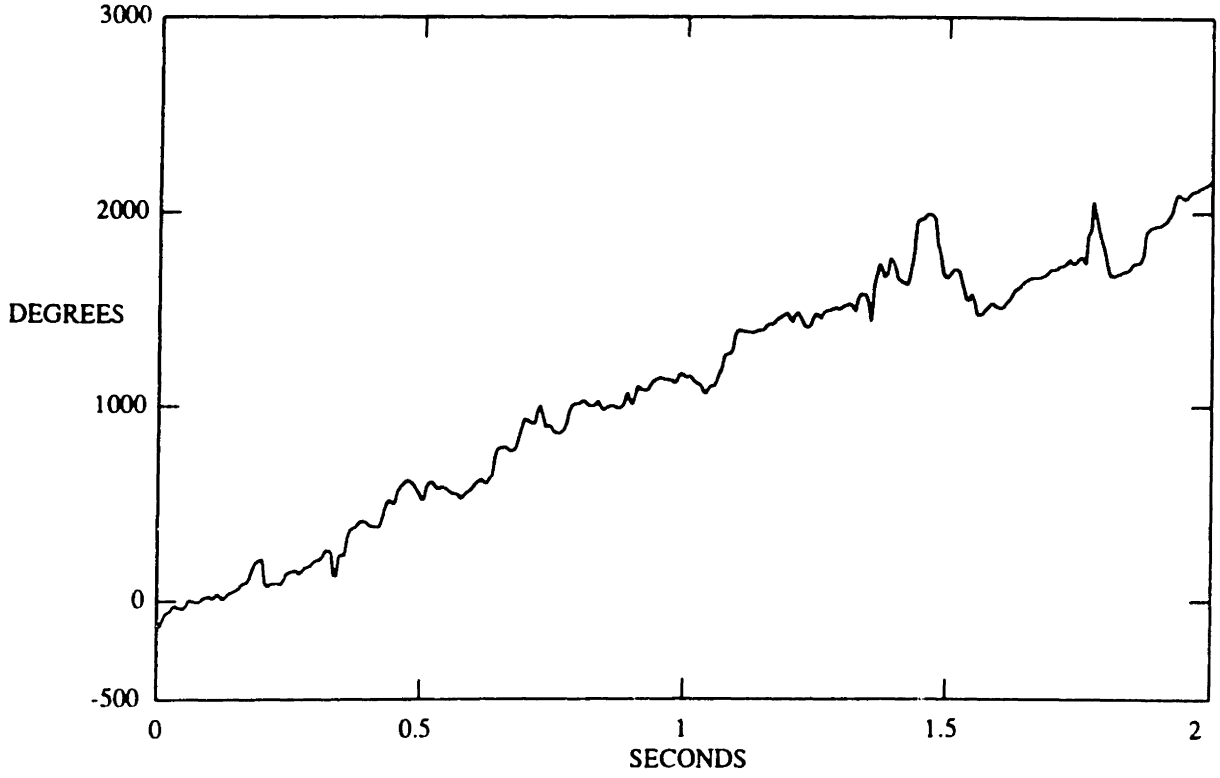

Figure 7.16: Time History of Phase Angle for Case 4: Backward Whirl with Substantial Slip, s = .58

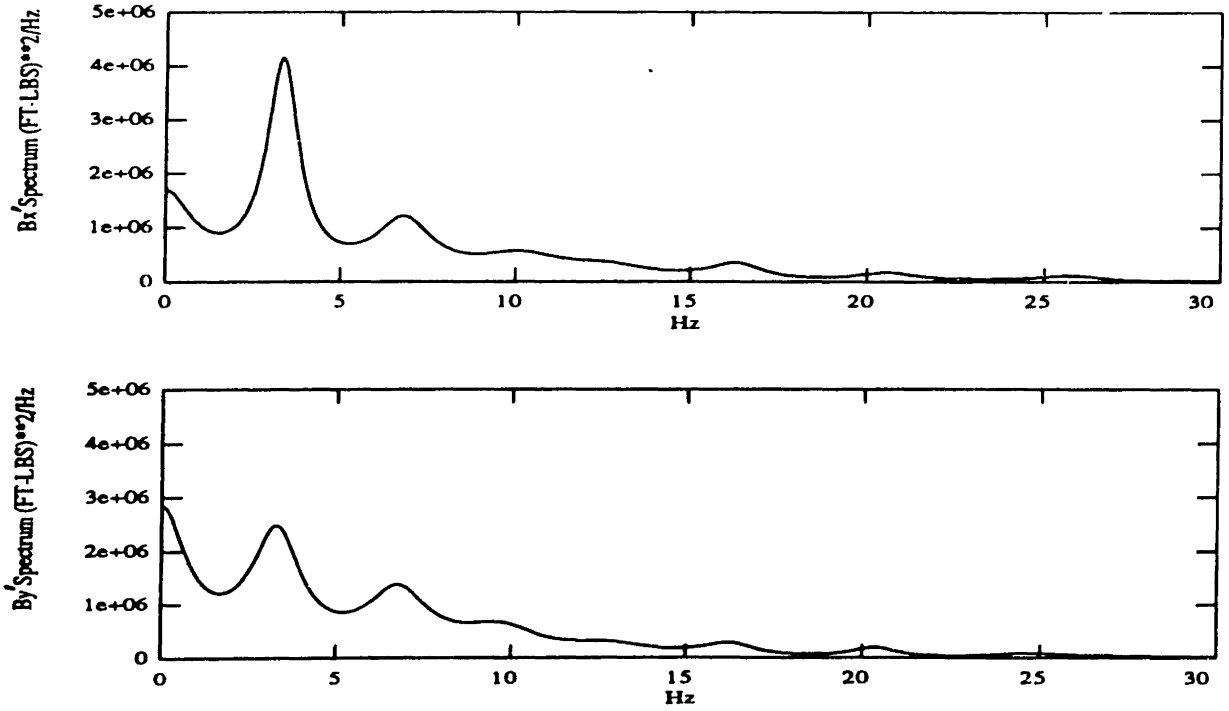

Figure 7.17: Bending Moment Spectra for Case 4: Backward Whirl with Substantial Slip, s = .58

7.3.7 Case 5: Linear Coupling of Axial and Transverse Vibrations

Figure 7.18 shows the time histories of weight on bit and one component of bending, $B_{x'}(t)$, while drilling through shale with a tri-cone bit at an average rate of penetration of 7 ft/hr. The depth was 6899 feet, and the approximate reported rotation rate was 60 RPM. The BHA the same as in case 4 above, with the measurements originating from a point just above the second stabilizer. This is a classic case of bit bounce, as can be seen by the large variation in WOB (45000 pounds peak to peak) and the flat bottoms at zero weight on bit when the bit leaves the bottom. In this figure, compression is positive. At first glance, the bending moment time series appears to contain little useful information.

Figure 7.19 shows the autospectra of the WOB and $B_{x'}$ time series. Both spectra show dominant peaks at the same frequency of 2.9 Hz. In this case, 2.9 Hz is the three times RPM cone rate which would result from a rotation rate of 0.97 Hz (58 RPM). This is consistent with the reported rotation rate of 60 RPM. In the WOB spectrum, the 6 times RPM higher harmonic is also evident. The reason that multiples of the 3 times RPM cone rate exist is that cone rate excitation is a periodic but not sinusoidal process. Therefore, higher order components at 6, 9, and even 12 times RPM frequently occur in axial and torsional vibration measurements, because they are necessary terms in the Fourier series, which make up the periodic, but non-sinusoidal, shape of the time series.

In this example, bit bounce occurs because of probable coincidence of strong 3 times RPM axial excitation and a longitudinal resonance of the drill string. The fact that both the WOB and $B_{x'}$ spectra have dominant peaks at the same frequency is a significant initial indication of linear coupling. Further evidence can be acquired by computing the cross spectrum and the coherence between $B_{x'}$ and WOB. Figure 7.20 shows the phase portion of the cross spectrum and the coherence. The coherence is a measure of the degree to which a linear cause and effect relationship can be established

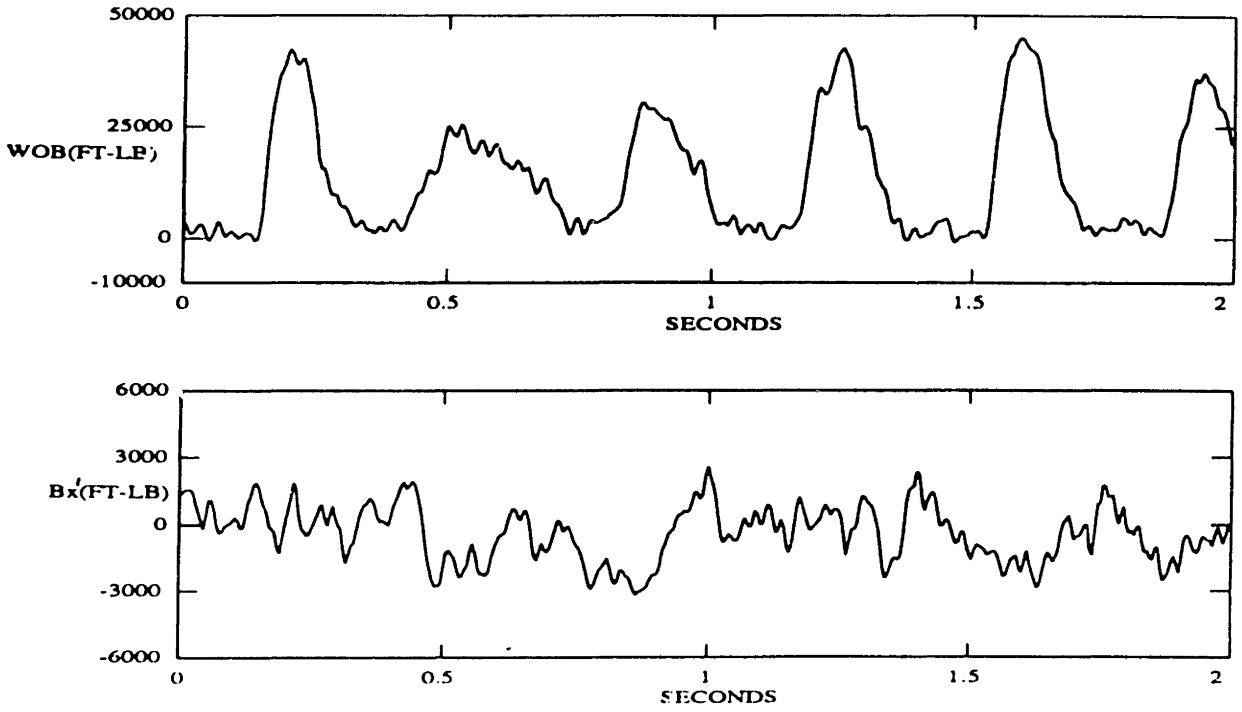

Figure 7.18: Time Histories of Weight on Bit and Bending Moment for Case 5: Linear Coupling Between Axial Force and Bending Vibration

between two time series. In this case, the coherence at 2.9 Hz is 0.97 with 1.0 being perfect coherence.

It can be concluded that the 2.9 Hz bending vibration is caused by a linear coupling mechanism to the WOB. At many other frequencies up to 30 Hz the coherence is also quite high. The phase at 2.9 Hz is 180 degrees, an indication that the bending vibration response is not at a resonance, which would be indicated by a phase angle nearer to 90 degrees. In this case, the WOB variations are so large, due to the bit bounce and axial resonance, that strong coupling exists even in the absence of a bending resonance.

Bit bounce is not a necessary condition for linear coupling to occur between axial force and bending. Since bit bounce involves large variations in axial force, the linear coupling to bending motion may become large enough to be the dominant bending phenomenon, which in this case provided an excellent example of both phenomena.

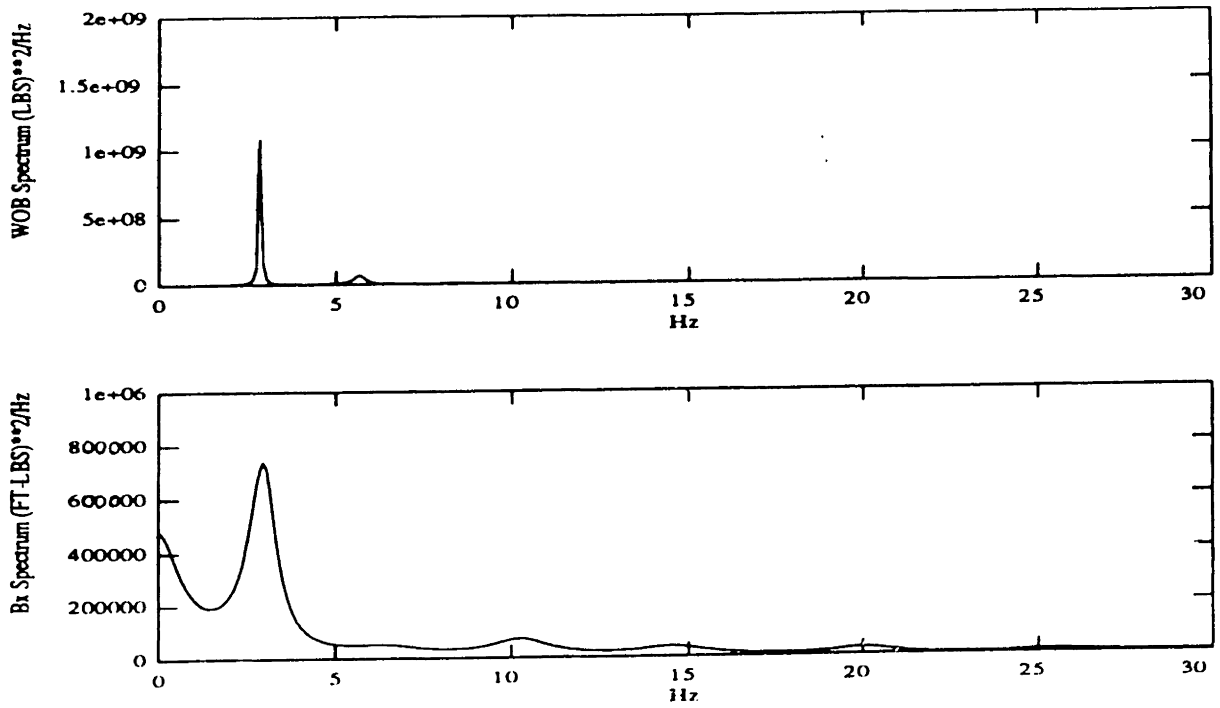

Figure 7.19: WOB and Bending Moment Spectra for Case 5: Linear Coupling Between Axial Force and Bending Vibration

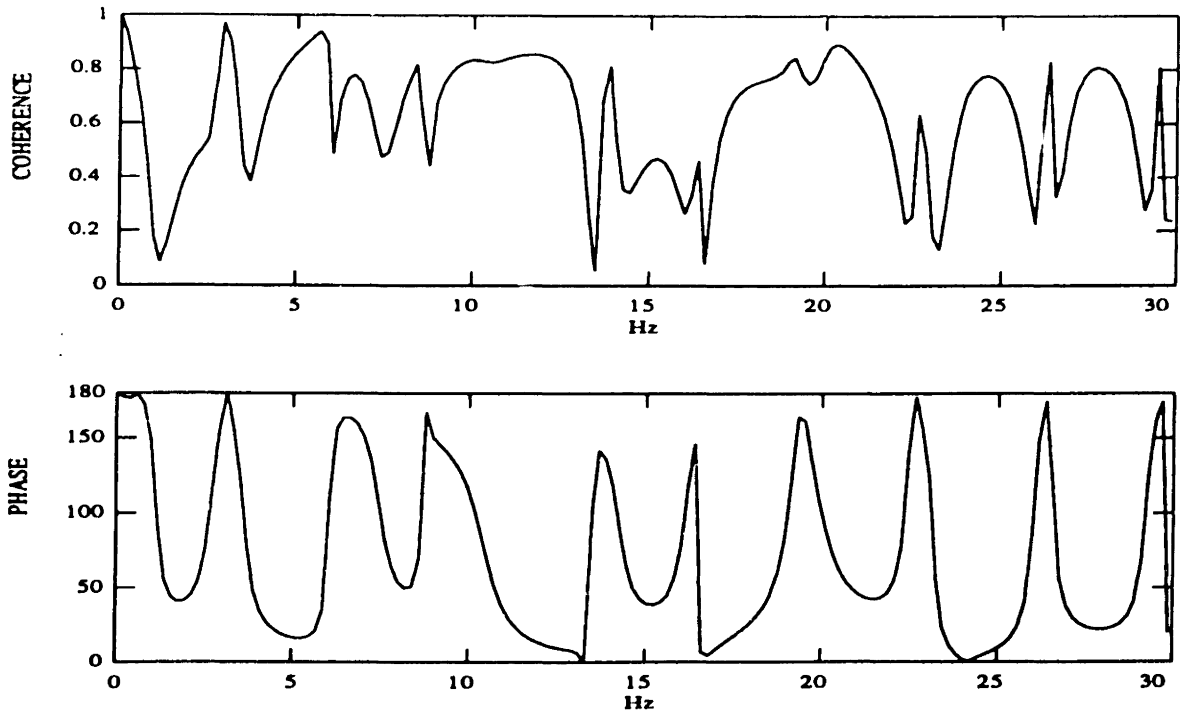

Figure 7.20: Coherence and Cross Spectrum Phase Between Axial Force and the x Component of Bending Moment

7.3.8 Case 6: Parametric Excited Bending Vibration

The mechanism for the parametric excited bending vibration is described in chapter 4. This phenomenon involves a quadratic relationship between WOB(input) and bending(output). To verify this phenomenon, a large number of data points are needed for the signal processing FFT algorithm. From the experience in evaluating, the BHA bending vibration seldom remained stationary for more than 10 seconds. Therefore, a special signal processing technique was developed to extract parametric excited bending vibration form a record length of only several seconds. The method is described below. Assuming that x(t) is the input and y(t) is the output, to a quadratic system, the input-output relationship is $x = y^2$, The following steps may be used to verify the quadratic relationship between input and output:

1. square the time history of x(t)

2. compute the linear coherence between the squared time history of x(t) and the y(t) time history using the two channel Maximum Entropy spectral analysis method

The coherence function thus obtain is termed quadratic coherence. The quadratic relationship between input and output is revealed as the peaks in the quadratic coherence. For example, if a peak of quadratic coherence is at 4 Hz, this indicates that the 4 Hz component in y resulted from squaring the 2 Hz component in x. Now we proceed to the example from the Shell data.

The example is drawn from data taken at 5138 feet, using a Hughes J22 tri-cone bit. The RPM is deduced from the WOB spectrum, which is shown in Figure 7.21. The principal peak is approximately 3 Hz. This peak usually corresponds to three times RPM generated by the cone passage. Thus, we can infer infer that the rotation was about 60 RPM.

Figure 7.22 shows the bending moment spectra measurements in two perpendicular planes. They reveal principal peaks at 1.5 Hz, half of the peak frequency from the

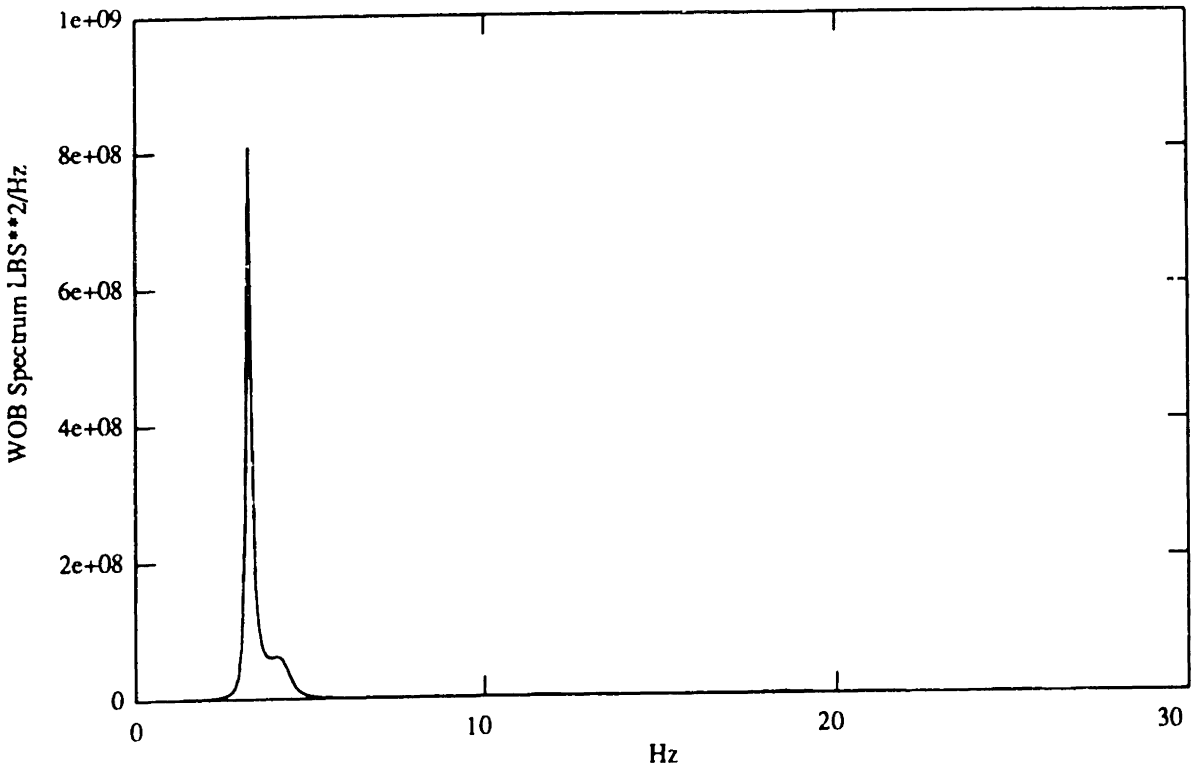

Figure 7.21: WOB Spectrum for Case 6

WOB spectrum.

A test for linear coupling was performed by computing the linear coherence between $B_{x'}$ and the WOB time history. The upper trace of Figure 7.23 is the linear coherence, which reveals a coherence of 0.65 for both peaks at 1.5 Hz and 3 Hz. This indicates that some bending vibration was resulting from linear coupling mechanisms with WOB dynamic fluctuations. The lower trace of Figure 7.23 is a quadratic coherence plot. It reveals a coherence of 0.75 at 3 Hz, which is twice the frequency of the bending peak and corresponds to the WOB dominant peak. This is an example of parametric excited bending vibration of the BHA.

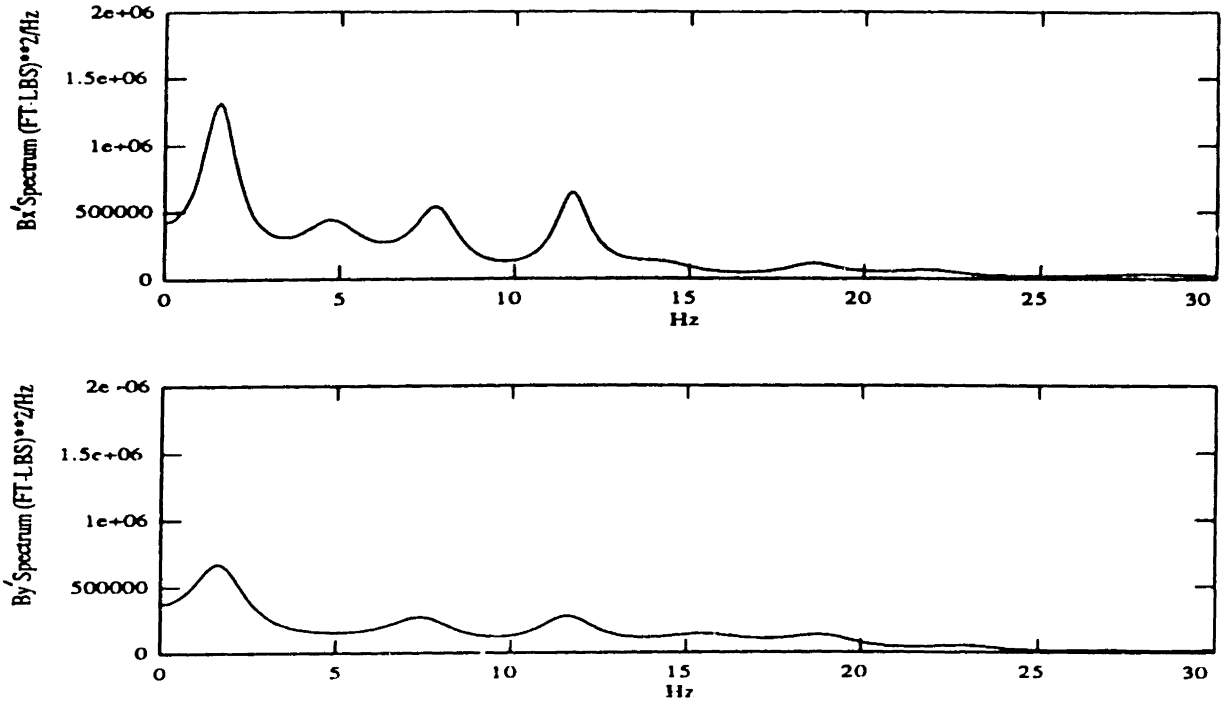

Figure 7.22: Bending x'and Bending y'Spectrum for Case 6

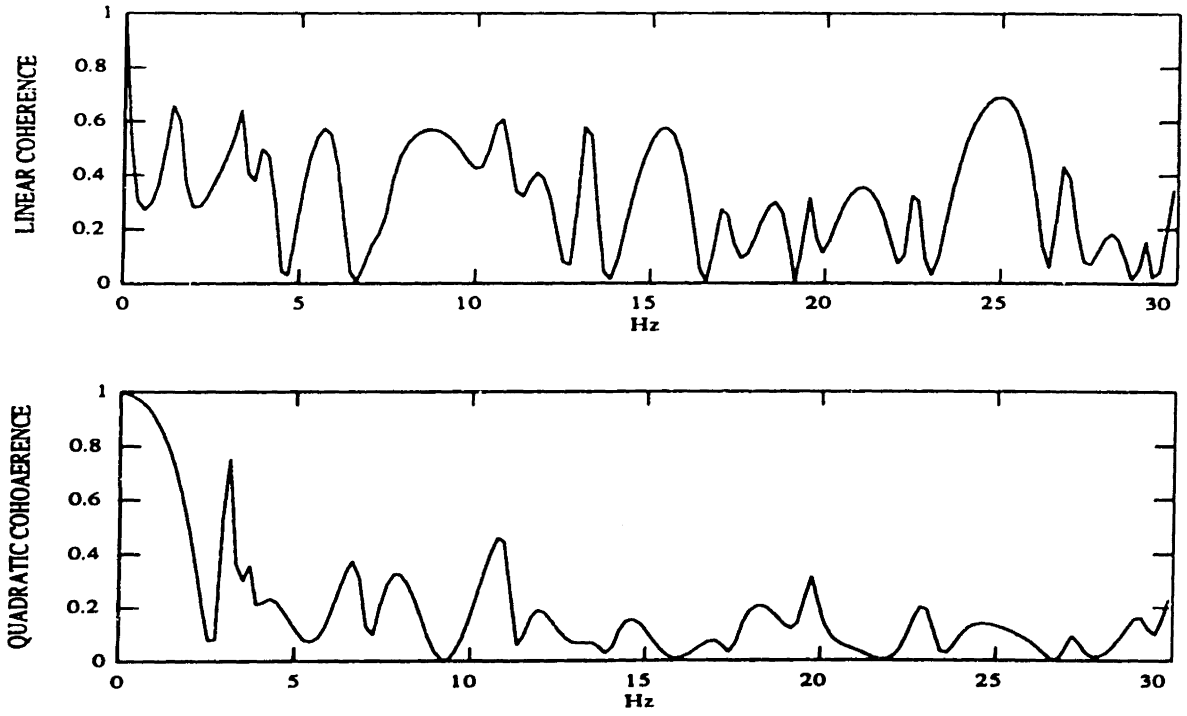

Figure 7.23: Linear and Quadratic Coherence Between WOB and Bending x for Case 6

Chapter 8

Conclusions and Suggestions

The goal of this thesis was to provide insights into the bending vibration of Bottom Hole Assemblies. Unlike axial and torsional vibrations, bending vibrations generated at the bottom are not transmitted to the surface through the drill string. Though, it may be possible to see the evidence of downhole bending vibration in in the surface axial and torsional vibration signals, the relationships are not well enough understood to be used diagnostically.

We started out by examing the mechanisms that cause the bending vibration in the BHA. These mechanisms are described in Chapters 3, 4, and 5. The laboratory tests revealed the important properties of linear and parametric coupling between axial and bending vibration. The tests also showed that the excitation frequency needed to drive the shaft at resonance for either type of coupling, varies linearly with respect to rotational frequency of the shaft.

Evidence of these two types of coupling were also found in the the data acquired during a field test. This data set also provides examples of the whirling behavior. Forward synchronous whirl and backward whirl with slip have been found in this data set. Forward whirl can cause abrasive wear of the drill collar outside diameter, and is a probable cause of flat spots. Backward whirl usually associated with high bending moments and high bending cycles. Therefore, it can shorten the fatigue life of drill collars and tool joints.

This research indicates that further work needs to be done in

1. predicting the onset of backward whirling

2. verifying the existence of parametrically excited bending vibration in cases of extensive wall contact as would be experienced in slick assemblies or above all stabilizers.

3. investigating the influence of bending dynamics on directional drilling

Bibliography

[1] T. D. Aarrestad, H. A. Tennesen, and A. Kyllingstad. "Drill String Vibrations: Comparison Between Theory and Experiments on a Full-Scale Research Drilling Rig". In *Proceedings of IADC/SPE Conference*, February 1986.

[2] J. A. Baird and M. C. Apostal. "Analyzing the Dynamic Behavior of Some Typical Rotary Bottom Hole Assemblies During Startup". *Transaction of Geothermal Resources Council*, 9:83–89, August 1985.

[3] J. A. Baird and B. C. Caskey. "Analyzing the Dynamic Behavior of Downhole Equipment During Drilling". *Transaction of Geothermal Resources Council*, 8:243–247, August 1984.

[4] J. A. Baird and et. al. "GEODYN2: A Bottom Hole Assembly-Geological Formation Dynamic Interaction Computer Program". *SPE Conference Paper Number 14328*, September 1985.

[5] A. A. Besaisow, Y. M. Jan, and F. J. Schuh. "Development of a Surface Drillstring Vibration Measurement System". *SPE Conference Paper Number 14327*, September 1985.

[6] A. A. Besaisow and M. L. Payne. "A Study of Excitation Mechanisms and Resonances Inducing BHA Vibrations". *SPE Conference Paper Number 15560*, October 1986.

[7] R. D. Blevins. *Formulas for Natural Frequency and Mode shape*. Van Nostrand Reinhold Co., New York, New York, 1979.

[8] M. J. Briggs. *Multichannel Maximum Entropy Method of Spectral Analysis Applied to Offshore Structures.* Ocean Engineer thesis, Massachusetts Institute of Technology, 1981.

[9] T. M. Burgess, G. L. McDaniel, and P. K. Das. "Improving BHA Tool Reliability with Drillstring Vibration Models: Field Experience and Limitations". In *Proceedings of 1987 IADC/SPE Conference*, New Orleans, March 1987.

[10] R. B. Campbell. *The Estimation of Natural Frequency and Damping Ratio of Offshore Structures.* PhD thesis, Massachusetts Institute of Technology, 1980.

[11] S. S. Chen, M. W. Wambsganss, and J. A. Jendrzejczyk. "Added Mass and Damping of a Vibrating Rod in Confined Viscous Fluids". *Journal of Applied Mechanics*, 326–329, June 1976.

[12] Wilson C. Chin. "Fatal Tubular Bending Motions Difficult to Detect Uphole". *Offshore*, 32–36, April 1988.

[13] D. A. Close, S. C. Owens, and J. D. MacPherson. "Measurement of BHA Vibration Using MWD". In *Proceedings of 1988 IADC/SPE Conference*, Dallas, March 1988.

[14] S. H. Crandall. "The Physical Nature of Rotor Instability Mechanisms". In *Rotor Dynamical Instability*, June 1983.

[15] R. A. Cunningham. "Analysis of Downhole Measurement of Drill String Forces and Motions". *Transaction of ASME*, 208–216, May 1968.

[16] D. W. Dareing. "Drill Collar Length is a Major Factor in Vibration Control". *Journal of Society of Petroleum Engineers*, 637–644, April 1984.

[17] F. H. Deily and et. al. "Downhole Measurement of Drill String Forces and Motions". *Journal of Engineering for Industry*, 217–225, May 1968.

[18] S. M. Dickinson. "The Lateral Vibration of Slightly Bent Slender Beams Subject to Prescribed Axial End Displacement". *Journal of Sound and Vibration*, 68(4):507–514, 1980.

[19] V. A. Dunayevsky, A. Judzis, and W. H. Mills. "Dynamic Stability of Drillstrings Under Fluctuating Weight-on-Bit". *SPE Conference Paper Number 14329*, September 1985.

[20] V. A. Dunayevsky, A. Judzis, and W. H. Mills. "Onset of Drillstring Precession in a Directional Borehole". *SPE Conference Paper Number 13027*, September 1984.

[21] F. B. Hilldebrand. *Advanced Calculus for Applications.* Prentice-Hall, Englewood Cliffs, New Jersey, 1976.

[22] C. S. Hsu. "Further Results on Parametric Excitation of a Dynamic System". *Journal of Applied Mechanics*, 373–377, June 1965.

[23] C. S. Hsu. "On the Parametric Excitation of a Dynamic System Having Multiple Degrees of Freedom". *Journal of Applied Mechanics*, 367–372, September 1963.

[24] T. Iwatsubo and M. Saigo. "Parametric Instability of Clamped-Clamped and Clamped- Simply Supported Columns Under Periodic Axial Force". *Journal of Sound and Vibration*, 30(1):65–77, 1973.

[25] T. Iwatsubo, Y. Sugiyama, and S. Ogino. "Simple and Combination Resonances of Columns Under Periodic Axial Loads". *Journal of Sound and Vibration*, 33(1):211–221, 1974.

[26] G. M. Jenkins and D. G. Watts. *Spectral Analysis and its Applications.* Holden-Day, 1968.

[27] N. R. Joglekar. *Experimental Evaluation of Rotor Motion With Radial Rub.* Master's thesis, Massachusetts Institute of Technology, June 1987.

[28] J. Y. Jong. *The Quadratic Correlation Between In-Line and Cross-Flow Vortex-Induced Vibration of Long Flexible Cylinders.* PhD thesis, Massachusetts Institute of Technology, 1984.

[29] John L. Kennedy. *Fundamentals of Drilling.* PennWell Publishing Company, Tulsa, Oklahoma, 1983.

[30] C. S. Kim and S. M. Dickinson. "The Flexure Vibration of Slightly Curved Slender Beams Subject to Axial End Displacement". *Journal of Sound and Vibration*, 104(1):170–175, 1986.

[31] Y. C. Kim. *Nonlinear Vibration of Long Slender Beams.* PhD thesis, Massachusetts Institute of Technology, 1983.

[32] Y. C. Kim and E. J. Powers. "Digital Bispectral Analysis and Its Applications to Nonlinear Wave Interaction". *IEEE Transactions on Plasma Science*, PS7(2), 1979.

[33] H. Y. Lee and J. K. Vandiver. "DSDYN2: A Longitudinal and Torsional Drill String Vibration Program". June 1987. An internal report to the industrial sponsors.

[34] R. G. Loewy and V. J. Piarulli. *Dynamics of Rotating Shafts.* The Shock and Vibration Information Center, United States Department of Defense, 1969.

[35] J. Lutz and et. al. "Instantaneous Logging Based on a Dynamic Theory of Drilling". *Journal of Petroleum Technology*, 750–758, June 1972.

[36] K. K. Millheim and M. C. Apostal. "The Effect of the Bottom Hole Assembly Dynamics on the Trajectory of a Bit". *Journal of Petroleum Technology*, 2323–2338, December 1981.

[37] A. Muszynska. "Partial Lateral Rotor to Stator Rubs". In *Vibrations in Rotating Machinery*, September 1984.

[38] A. H. Nayfeh and D. T. Mook. *Nonlinear Oscillation.* John Wiley & Sons, New York, New York, 1979.

[39] A. V. Oppenheim and R. W. Schafer. *Digital Signal Processing.* Prentice Hall, 1975.

[40] P.R. Pasley and D.B. Bogy. "The Stability of a Circular Rod Laterally Constrained to Be in Contact With an Inclined Circular Cylinder". *Journal of Applied Mechanics*, 605–610, December 1965.

[41] M. Reis. *Wave Propagation in Elastic Beams and Rods.* PhD thesis, Massachusetts Institute of Technology, 1978.

[42] O. F. Rey. *Dynamics of Unbalanced Drill Collar in a Slanted Hole.* Master's thesis, Massachusetts Institute of Technology, May 1983.

[43] H. J. Rice and J. A. Fitzpatrick. "An Alternative to the Bispectral Approach fo the Analysis of Flow Induced Vibration". In *Proceedings of Symposium on Flow Induced Vibration*, ASME, 1988.

[44] R. J. Shyu and J. K. Vandiver. "BEND2PC : A Bending Natural Frequency Prediction Program for Bottom Hole Assembly". July 1987. An internal report to the industrial sponsors.

[45] S. J. Stackley. *Dynamics of Full Annular Rotor Rub.* Master's thesis, Massachusetts Institute of Technology, June 1986.

[46] C. M. Stone, T. G. Carne, and B. C. Caskey. "Qualification of a Computer Program for Drill String Dynamics". *Transaction of Geothermal Resources Council*, 9:157–162, August 1985.

[47] S. P. Timoshenko and J. M. Gere. *Theory of Elastic Stability.* Mcgraw-Hill, New York, New York, 1970.

[48] A. Tondl. *Some Problems of Rotor Dynamics.* Chapman & Hall, London, England, 1965.

[49] J. K. Vandiver. "Coupled Axial, Bending, and Torsional Vibration of Rotating Drill Strings". July 1988. An internal report to the industrial sponsors.

[50] J. K. Vandiver, J. W. Nicholson, and R. J. Shyu. "Case Studies of the Bending Vibration and Whirling Motion of Drill Collars". In *Proceedings of 1989 IADC/SPE Conference*, New Orleans, Louisiana, March 1989.

[51] J. K. Vandiver and R. J. Shyu. "Analysis of the Bending Vibration of Bottom Hole Assemblies With Case Studies From the Quitman Field Test". April 1987. An internal report to the industrial sponsors.

[52] S. F. Wolf, M. Zacksenhouse, and A. Arian. "Field Measurement of Downhole Drill String Vibration". *SPE Conference Paper Number 14330*, September 1985.

[53] W. Zhang. "Dynamic Instability of Multi-Degree-of-Freedom Flexible Rotor Systems Due to Full Annular Rub". In *Proceedings of the Institution of Mechanical Engineers*, pages 305–310, Heriot-Watt University, Edinburgh, England, September 1988.

Appendix A

Finite Difference Formulations for Linear Bending Vibration

The homogeneous equation of motion of the bending vibration of the Bottom Hole Assembly involving only the spatial variable is :

$$\frac{d^4s}{dw^4} + a_1\frac{d^3s}{dw^4} + a_2(l_1 - w)\frac{d^2s}{dw^2} - a_2\frac{ds}{dw} + a_3 s = 0 \qquad \text{(A.1)}$$

where

$$a_1 = i\frac{QL}{EI} \qquad \text{(A.2a)}$$

$$a_2 = \frac{gh\cos\phi}{C_M L\omega_0^2} \qquad \text{(A.2b)}$$

$$a_3 = -i\frac{C_i\Omega}{A\rho C_M\omega_0^2} \qquad \text{(A.2c)}$$

The central finite difference scheme is introduced to transform the differential equation into a set of simultaneous equations, which can be solved by linear algebra. The central difference approximations to the differentials are :

$$(\frac{ds}{dw})_j = \frac{N}{2}(-s_{j-1} + s_{j+1}) \qquad \text{(A.3a)}$$

$$(\frac{d^2s}{dw^2})_j = N^2(s_{j-1} - 2s_j + s_{j+1}) \qquad \text{(A.3b)}$$

$$(\frac{d^3s}{dw^3})_j = \frac{N^3}{2}(-s_{j-2} + 2s_{j-1} - 2s_{j+1} + s_{j+2}) \qquad \text{(A.3c)}$$

$$(\frac{d^4s}{dw^4})_j = N^4(s_{j-2} - 4s_{j-1} + 6s_j - 4s_{j+1} + s_{j+2}) \qquad \text{(A.3d)}$$

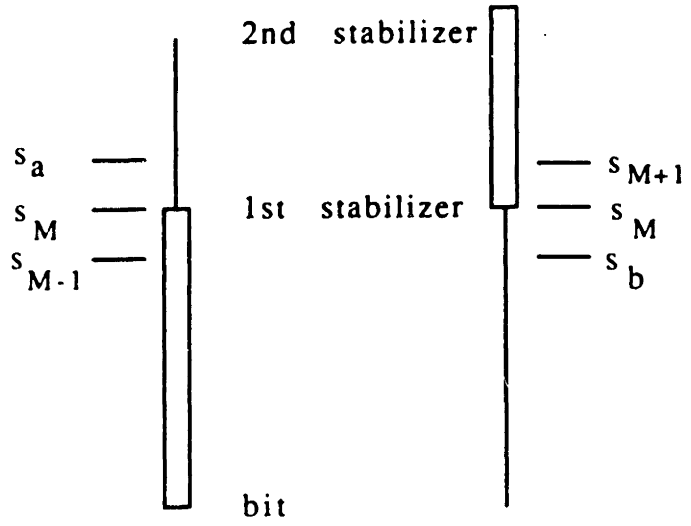

Figure A.1: The Fictitious Point for the Finite Difference Scheme

where j indicates j-*th* point on the collar. The condition at the bit and the two stabilizer can be resolved by method fictitious points. In central finite difference scheme for beam vibration, one needs one more point beyond the boundary, due to condition on the equilibrium of moments, to construct the finite difference matrix. This fictitious point can be represented by the points inside the boundary through the boundary conditions. Figure A.1 is a figure indicating the location of the fictitious points. The boundaries at the bit and the second stabilizer are assumed to be with torsional spring, so at bit

$$s_0 = 0 \tag{A.4a}$$

$$N_a^2(s_{-1} + s_1) = \frac{K_b L}{EI_a}\frac{N_a}{2}(-s_{-1} + s_1) \tag{A.4b}$$

where K_b is the torsional sprig constant for the bit, and at second stabilizer same conditions can be applied

$$s_N = 0 \tag{A.5a}$$

$$N_a^2(s_{N-1} + s_{N+1}) = \frac{K_s L}{EI_b}\frac{N_b}{2}(-s_{N-1} + s_{N+1}) \tag{A.5b}$$

where K_s is the torsional spring constant at the 2nd stabilizer, and N is the total number of finite difference element from bit to the second stabilizer. From these two equations, we have

$$s_{-1} = a_8 s_1 \tag{A.6a}$$

$$s_{N+1} = a_9 s_{N-1} \tag{A.6b}$$

if we denote $b_1 = \frac{K_b L}{EI_a}$ and $b_2 = \frac{K_s L}{EI_b}$, then

$$a_8 = \frac{b_1 - 2N_a}{b_1 + 2N_a} \tag{A.7a}$$

$$a_9 = \frac{b_2 + 2N_b}{b_2 + 2N_b} \tag{A.7b}$$

The interface conditions for the first stabilizer are the continuation of the slope, and the equilibrium of the moment. By same procedure, we can describe these interface conditions using fictitious points. Assuming that s_a is the fictitious for the section from bit to first stabilizer, and s_b is the fictitious for the section from first stabilizer to second stabilizer, and M the number of element from bit to the first stabilizer, then

$$\frac{s_b - s_{M-1}}{2\Delta_a} = \frac{s_{M+1} - s_a}{2\Delta_b} \tag{A.8a}$$

$$\frac{s_b + s_{M-1}}{\Delta_a^2} = K\frac{s_{M+1} + s_a}{\Delta_b^2} \tag{A.8b}$$

where $K = \frac{EI_a}{EI_b}$, $\Delta_a = \frac{L_a}{M}$,and $\Delta_b = \frac{L_b}{N-M}$. Solved for s_a and s_b, we have

$$s_a = \frac{\frac{2}{\Delta_a^2}}{\frac{1}{\Delta_a\Delta_b} + \frac{K}{\Delta_b^2}} s_{M-1} + \frac{\frac{1}{\Delta_a\Delta_b} - \frac{K}{\Delta_b^2}}{\frac{1}{\Delta_a\Delta_b} + \frac{K}{\Delta_b^2}} s_{M+1} \tag{A.9}$$

$$s_b = \frac{\frac{K}{\Delta_a\Delta_b} - \frac{1}{\Delta_a^2}}{\frac{K}{\Delta_a\Delta_b} + \frac{1}{\Delta_a^2}} s_{M-1} + \frac{\frac{2K}{\Delta_b^2}}{\frac{K}{\Delta_a\Delta_b} + \frac{1}{\Delta_a^2}} s_{M+1} \tag{A.10}$$

For convenience, let us denote the coefficients of s_{M-1} and s_{M+1} as f_1 and f_2 in equation A.9, and as f_3 and f_4 in equation A.10 respectively. By substituting the finite difference approximation to the governing equation, and using the above boundary conditions, a system of finite difference equations can be obtained for the bending vibration of the BHA,

$$\underline{F} \cdot \underline{s} = \underline{0} \tag{A.11}$$

where $\underline{F}$ is shown in the following table. It is a band-limited matrix with five diagonal columns, and the dimension of this matrix is N-2.

Table A.1: The Finite Difference Matrix for a Two Spans Drill Collar

$$\begin{bmatrix}
u_1 & d_1 & e_1 & & & & & & & & & & \\
q_1 & u_2 & d_2 & e_2 & & & & & & & & & \\
p_1 & q_2 & u_3 & d_3 & e_3 & & & & & & & & \\
 & p_2 & \cdot & \cdot & \cdot & e_4 & & & & & & & \\
 & & \cdot & \cdot & \cdot & \cdot & \cdot & & & & & & \\
 & & & p_{M-4} & q_{M-3} & u_{M-2} & d_{M-2} & 0 & & & & & \\
 & & & & p_{M-3} & q_{M-2} & u_{M-1} & d'_{M-1} & 0 & & & & \\
 & & & & & 0 & q_{M-1} & u'_M & d'_M & e'_M & & & \\
 & & & & & & 0 & q'_M & u'_{M+1} & d'_{M+1} & e'_{M+1} & & \\
 & & & & & & & p'_M & q'_{M+1} & u'_{M+2} & d'_{M+2} & e'_{M+2} & \\
 & & & & & & & & \cdot & \cdot & \cdot & \cdot & \cdot \\
 & & & & & & & & & p'_{N-6} & \cdot & \cdot & \cdot \\
 & & & & & & & & & & p'_{N-5} & q'_{N-4} & u'_{N-3} \\
 & & & & & & & & & & & p'_{N-4} & q'_{N-3} \\
 & & & & & & & & & & & & \\
\end{bmatrix}
\begin{matrix}
 & & & & & & & & & & & & e'_{N-4} \\
 & & & & & & & & & & & & d'_{N-3} \\
 & & & & & & & & & & & & u'_{N-2}
\end{matrix}$$

where $'$ denotes the properties pertaining to the material between first and second stabilizer, and $\underline{s}$ is $\{s_1, s_2, \cdots, s_{M-1}, s_{M+1}, \cdots, s_{N-2}, s_{N-1}\}^T$, which is a column vector of displacement of the collar, and has N-2 elements. $\underline{0}$ is a zero vector. If we use the

following notations

$$c_1 = M^4 - \frac{a_1}{2}M^3 \quad \text{(A.12a)}$$

$$c_1' = (N-M)^4 \frac{a_1'}{2}(N-M)^3 \quad \text{(A.12b)}$$

$$c_2 = -4M^4 + a_1 M^3 + a_2 l_1 M^2 + \frac{1}{2}a_2 M \quad \text{(A.12c)}$$

$$c_2' = -4(N-M)^4 + a_1'(N-M)^3 + a_2' l_1 (N-M)^2 + \frac{1}{2}a_2'(N-M) \quad \text{(A.12d)}$$

$$c_3 = 6M^4 - 2a_2 l_1 N^2 + a_3 \quad \text{(A.12e)}$$

$$c_3' = 6(N-M)^4 - 2a_2' l_1 (N-M)^2 + a_3' \quad \text{(A.12f)}$$

$$c_4 = -4M^4 - a_1 M^3 + a_1 l_1 M^2 - \frac{1}{2}a_2 M \quad \text{(A.12g)}$$

$$c_4' = -4(N-M)^4 - a_1'(N-M)^3 + a_2' l_1 (N-M)^2 - \frac{1}{2}a_2'(N-M) \quad \text{(A.12h)}$$

$$c_5 = M^4 + \frac{a_1}{2}M^3 \quad \text{(A.12i)}$$

$$c_5' = (N-M)^4 + \frac{a_1'}{2}(N-M)^3 \quad \text{(A.12j)}$$

then, the elements, p_n, q_n, u_n, d_n, e_n, in the matrix have the following form:

$$p_n = c_1 \quad , \quad 1 \le n \le M-3 \quad \text{(A.13a)}$$

$$p_n' = c_1' \quad , \quad M \le n \le N-4 \quad \text{(A.13b)}$$

$$q_n = c_2 - (n+1)a_2 M \quad , \quad 1 \le n \le M-2 \quad \text{(A.13c)}$$

$$q_{M-1} = c_1 f_3 \quad \text{(A.13d)}$$

$$q_n' = c_2' - (n+2)a_2(N-M) \quad , \quad M \le n \le N-3 \quad \text{(A.13e)}$$

$$u_1 = c_3 + 2a_2 M + c_1 a_3 \quad \text{(A.13f)}$$

$$u_n = c_3 + 2n a_2 M \quad , \quad 2 \le n \le M-2 \quad \text{(A.13g)}$$

$$u_{M-1} = c_3 + 2(M-1)a_2 M + c_5 f_1 \quad \text{(A.13h)}$$

$$u_M' = c_3' + 2(M+1)a_2(N-M) + c_1' f_4 \quad \text{(A.13i)}$$

$$u'_n = c'_3 + 2(n+1)a'_2(N-m) \quad , \quad M+1 \le n \le N-3 \qquad \text{(A.13j)}$$

$$u'_{N-2} = c'_3 + 2(N-1)a'_2(N-m) + c'_5 a_9 \qquad \text{(A.13k)}$$

$$d_n = c_4 - na_2M \quad , \quad 1 \le n \le M-2 \qquad \text{(A.13l)}$$

$$d'_M = c_5 f_1 \qquad \text{(A.13m)}$$

$$d'_n = c'_4 - na'_2(N-M) \quad , \quad M \le n \le N-4 \qquad \text{(A.13n)}$$

$$e_n = c_5 \quad , \quad 1 \le n \le M-3 \qquad \text{(A.13o)}$$

$$e'_n = c'_5 \quad , \quad M \le n \le N-4 \qquad \text{(A.13p)}$$

The eigenvalues and eigen vectors of this system can be obtained through standard eigensolvers, for example EINSPACK, IMSL or NAG.

Appendix B

Equations of Bending Vibration with Borehole Constraint

The equations of motion of bending vibration of the BHA are shown in equation 3.1 and 3.2. If the collar is forced to be in contact with the wall, then the following relationship holds

$$x = \Delta \sin\gamma \tag{B.1a}$$

$$y = \Delta \cos\gamma \tag{B.1b}$$

Recall that Δ is the clearance between the collar and the wall, γ is the angle from the collar to its original unbent configuration. Note that γ is a function of the vertical axis z, and time t. From equation B.1a, the spatial derivatives with respect to vertical axis, z, can be written as follows :

$$\frac{\partial x}{\partial z} = \Delta \sin\gamma(\frac{\partial \gamma}{\partial z}) \tag{B.2a}$$

$$\frac{\partial^2 x}{\partial z^2} = \Delta(\cos\gamma(\frac{\partial \gamma}{\partial z})^2 + \sin\gamma(\frac{\partial^2 \gamma}{\partial z^2})) \tag{B.2b}$$

$$\frac{\partial^3 x}{\partial z^3} = \Delta(3\cos\gamma(\frac{\partial \gamma}{\partial z})\frac{\partial^2 \gamma}{\partial z^2} - \sin\gamma(\frac{\partial \gamma}{\partial z})^3 + \sin\gamma(\frac{\partial^3 \gamma}{\partial z^3})) \tag{B.2c}$$

$$\begin{aligned}\frac{\partial^4 x}{\partial z^4} = \Delta(&-3\sin\gamma(\frac{\partial \gamma}{\partial z})^2\frac{\partial^2 \gamma}{\partial z^2} + 3\cos\gamma(\frac{\partial^2 \gamma}{\partial z^2})^2 + 3\cos\gamma(\frac{\partial \gamma}{\partial z})\frac{\partial^3 \gamma}{\partial z^3} \\ &- 3\sin\gamma(\frac{\partial \gamma}{\partial z})^2\frac{\partial^2 \gamma}{\partial z^2} + \cos\gamma(\frac{\partial \gamma}{\partial z})\frac{\partial^3 \gamma}{\partial z^3} - \cos\gamma(\frac{\partial \gamma}{\partial z})^4 + \sin\gamma(\frac{\partial^4 \gamma}{\partial z^4}))\end{aligned} \tag{B.2d}$$

If similar differentiation is carried out on equation B.1b, then

$$\frac{\partial x}{\partial z} = \Delta\cos\gamma(\frac{\partial\gamma}{\partial z}) \tag{B.3a}$$

$$\frac{\partial^2 x}{\partial z^2} = \Delta(-\sin\gamma(\frac{\partial\gamma}{\partial z})^2 + \cos\gamma(\frac{\partial^2\gamma}{\partial z^2})) \tag{B.3b}$$

$$\frac{\partial^3 x}{\partial z^3} = \Delta(-3\sin\gamma(\frac{\partial\gamma}{\partial z})\frac{\partial^2\gamma}{\partial z^2} - \cos\gamma(\frac{\partial\gamma}{\partial z})^3 + \cos\gamma(\frac{\partial^3\gamma}{\partial z^3})) \tag{B.3c}$$

$$\begin{aligned}\frac{\partial^4 x}{\partial z^4} &= \Delta(-3\cos\gamma(\frac{\partial\gamma}{\partial z})^2\frac{\partial^2\gamma}{\partial z^2} - 3\sin\gamma(\frac{\partial^2\gamma}{\partial z^2})^2 - 3\sin\gamma(\frac{\partial\gamma}{\partial z})\frac{\partial^3\gamma}{\partial z^3} \\ &- 3\cos\gamma(\frac{\partial\gamma}{\partial z})^2\frac{\partial^2\gamma}{\partial z^2} - \sin\gamma(\frac{\partial\gamma}{\partial z})\frac{\partial^3\gamma}{\partial z^3} + \sin\gamma(\frac{\partial\gamma}{\partial z})^4 + \cos\gamma(\frac{\partial^4\gamma}{\partial z^4}))\end{aligned} \tag{B.3d}$$

If the nonlinear terms involving the product of the differentials are neglected in equation B.2d and B.3d, and substituting these expressions into the equation 3.1 and 3.2, and adding these two equations together, we find

$$\begin{aligned}&A\rho C_M\Delta\frac{\partial^2\gamma}{\partial t^2}(\cos\gamma+\sin\gamma) + EI\Delta(\cos\gamma+\sin\gamma)\frac{\partial^4\gamma}{\partial z^4} \\ -\ &Q(\sin\gamma-\cos\gamma)\frac{\partial^3\gamma}{\partial z^3} + (C_E+C_I)\Delta(\cos\gamma+\sin\gamma)\frac{\partial\gamma}{\partial t} \\ +\ &A\rho gh\cos\phi[(l-z)\Delta(\cos\gamma+\sin\gamma)\frac{\partial^2 x}{\partial z^2} - \Delta(\cos\gamma+\sin\gamma)\frac{\partial x}{\partial z}] \\ +\ &A\rho gh\sin\phi\sin\gamma = 0\end{aligned} \tag{B.4}$$

If we further assume that γ is small, then equation B.4 can be written as follows :

$$\begin{aligned}&A\rho C_M\frac{\partial^2\gamma}{\partial t^2} + (C_E+C_I)\frac{\partial\gamma}{\partial t} + EI\frac{\partial^4\gamma}{\partial z^4} + Q\frac{\partial^3\gamma}{\partial z^3} \\ +\ &A\rho gh\cos\phi[(l-z)\frac{\partial^2\gamma}{\partial z^2} - \frac{\partial\gamma}{\partial z}] + A\rho gh\frac{\sin\phi}{\Delta}\gamma = 0\end{aligned} \tag{B.5}$$

This equation is almost same as equation 3.3, except for the last term, which involving the the clearance and the slant angle of the borehole. This term representing the effect of the gravity on the constraint dynamics. It is similar to the effect of a spring, and is proportional to the angle γ.

Appendix C

Green Function of a Rotating Beam with Linearly Varying Tension

The equation of motion of bending vibration with respect to a rotating reference frame, with rotational speed Ω, is equation 3.8, as repeated here with variable sectional properties

$$A(z)\rho(z)C_M(z)\ddot{r}' + (C_E(z) + C_I(z) + i2\Omega A(z)\rho(z)C_M(z))\dot{r}' + \frac{\partial^2}{\partial z^2}(E(z)I(z)\frac{\partial^2 r'}{\partial z^2}) + \frac{\partial}{\partial z}(T(z)\frac{\partial r'}{\partial z}) - (\Omega^2 - iC_E(z)\Omega)r' = f(z,t) \quad \text{(C.1)}$$

Boundary conditions for single span pinned-pinned beam are

$$r'(0,t) = 0, \quad \frac{\partial^2 r'(0,t)}{\partial z^2} = 0 \quad \text{(C.2a)}$$

$$r'(L,t) = 0, \quad \frac{\partial^2 r'(L,t)}{\partial z^2} = 0 \quad \text{(C.2b)}$$

If the following notations are used:

$$m(z) = A(z)\rho(z)C_M(z) \quad \text{(C.3a)}$$

$$d(z) = C_E(z) + C_I(z) + i2\Omega A(z)\rho(z)C_M(z) \quad \text{(C.3b)}$$

and the equation C.1 is normalized with respect to following variables: $\omega_0^2 = \frac{E_0 I_0}{m_0 L^4}$, $w = \frac{z}{L}$, $\tau = \omega_0 t$, and $r = \frac{r'}{L}$, where subscript "0" denotes the values at a reference

position on the beam, then this equation can be transformed into

$$M(w)\frac{\partial^2 r}{\partial \tau^2} + R(w)\frac{\partial r}{\partial \tau} + \frac{\partial^2}{\partial w^2}(P(w)\frac{\partial^2 r}{\partial w^2}) + \frac{\partial}{\partial w}(Q(w)\frac{\partial r}{\partial w}) - (\frac{\Omega^2}{\omega_0^2} - i\frac{C_E\Omega}{m_0\omega_0^2})r = F(w,\tau) \quad \text{(C.4)}$$

where

$$M(w) = \frac{m(wL)}{m_0} \quad \text{(C.5a)}$$

$$R(w) = d(wL)\sqrt{\frac{L^4}{E_0 I_0 m_0}} \quad \text{(C.5b)}$$

$$Q(w) = \frac{T(wL)L^2}{E_0 I_0} \quad \text{(C.5c)}$$

$$P(w) = \frac{E(wL)I(wL)}{E_0 I_0} \quad \text{(C.5d)}$$

$$F(w,\tau) = \frac{f(wL,\tau/\omega_0)L^3}{E_0 I_0} \quad \text{(C.5e)}$$

C.1 Green's Function

If we assume the input is of the form

$$F(w,\tau) = \delta(w-\eta)e^{-i\omega\tau} \quad \text{(C.6)}$$

which is a delta function in space but sinusoidal in time, then assume the solution for this equation is

$$r(w,\tau) = \psi e^{-i\omega\tau} \quad \text{(C.7)}$$

Then, the solution for the equation, which is the Green's function of the rotating tensioned beam, according to Kim [31] is

$$\psi(w,\eta) = \frac{T_2(w)T_2(\eta)}{B_1}\sin[\int_0^w H_2 d\xi]\sin[\int_\eta^1 H_2 d\xi] - \frac{T_1(w)T_1(\eta)}{B_2}\sinh[\int_0^w H_1 d\xi]\sinh[\int_\eta^1 H_1 d\xi] \quad 0 \le w \le \eta \quad \text{(C.8)}$$

and

$$\psi(w,\eta) = \frac{T_2(w)T_2(\eta)}{B_1}\sin[\int_0^\eta H_2 d\xi]\sin[\int_w^1 H_2 d\xi] - \frac{T_1(w)T_1(\eta)}{B_2}\sinh[\int_0^\eta H_1 d\xi]\sinh[\int_w^1 H_1 d\xi] \quad \eta \le w \le 1 \qquad \text{(C.9)}$$

where

$$T_1(w) = \frac{1}{\sqrt{P}}[\frac{1}{2}(\frac{Q}{P})^3 + 2(\frac{QU}{P^2}) + \frac{1}{2}((\frac{Q}{P})^2 + 4\frac{U}{P})^{\frac{3}{2}}]^{\frac{1}{4}} \qquad \text{(C.10a)}$$

$$T_2(w) = \frac{1}{\sqrt{P}}[-\frac{1}{2}(\frac{Q}{P})^3 - 2(\frac{QU}{P^2}) + \frac{1}{2}((\frac{Q}{P})^2 + 4\frac{U}{P})^{\frac{3}{2}}]^{\frac{1}{4}} \qquad \text{(C.10b)}$$

$$H_1(w) = \sqrt{\frac{1}{2}(\frac{Q}{P}) + \frac{1}{2}\sqrt{(\frac{Q}{P})^2 + 4\frac{U}{P}}} \qquad \text{(C.10c)}$$

$$H_2(w) = \sqrt{-\frac{1}{2}(\frac{Q}{P}) + \frac{1}{2}\sqrt{(\frac{Q}{P})^2 + 4\frac{U}{P}}} \qquad \text{(C.10d)}$$

$$B_1 = sin(\int_0^1 H_2 d\xi) \qquad \text{(C.10e)}$$

$$B_2 = sinh(\int_0^1 H_1 d\xi) \qquad \text{(C.10f)}$$

$$U = M(w)\omega^2 - iR(w)\omega - \frac{\Omega^2}{\omega_0^2} + i\frac{C_E\Omega}{m_0\omega_0^2} \qquad \text{(C.10g)}$$

This Green's function is the first order approximation to the exact solution obtained using perturbation techniques.